

MASTER

Active damping of lenstop vibrations

Verbeek, T.R.

Award date:
2000

[Link to publication](#)

Disclaimer

This document contains a student thesis (bachelor's or master's), as authored by a student at Eindhoven University of Technology. Student theses are made available in the TU/e repository upon obtaining the required degree. The grade received is not published on the document as presented in the repository. The required complexity or quality of research of student theses may vary by program, and the required minimum study period may vary in duration.

General rights

Copyright and moral rights for the publications made accessible in the public portal are retained by the authors and/or other copyright owners and it is a condition of accessing publications that users recognise and abide by the legal requirements associated with these rights.

- Users may download and print one copy of any publication from the public portal for the purpose of private study or research.
- You may not further distribute the material or use it for any profit-making activity or commercial gain

China!

TU/e



Active damping of lensstop vibrations

Author: T.R.Verbeek

Master of Science Thesis
Veldhoven, February 2000 until November 2000

Commissioner: Prof.Dr.Ir. P.P.J.van den Bosch
Supervisors: Dr.Ir. H.Butler
Dr.Ir. A.A.H.Damen
Dr.Ir. W.P.M.H.Heemels

Institutions:

Control Group
Mechatronic Systems Development
ASM Lithography
Veldhoven, The Netherlands

Measurement and control Section
Measurement and Control Systems
Faculty of Electrical Engineering
Eindhoven University of Technology
Eindhoven, The Netherlands

(16) IDE!
(25) : "wrong" experiments?
(26) lens stop seen on noise?
sharp.
(31) phase is sensitive!
24-46 \leftrightarrow 33-34%
unmovable
vaf 40
(40) Exper 40, 3 = best
(43) Tustin aliasing.
(46) Perfect w \rightarrow No Rt.

Summary

Lenstop vibrations are a limiting factor in the achieved accuracy of the projection within ASML wafer scanners. In this report a controller is designed to damp these vibrations with the existing airmount system as actuator and accelerometers located at the lenstop as sensors. Especially lenstop vibrations in the frequency area of 50-110 Hz contribute to the reticle stage position error. Consequently the design aim is to damp the vibrations in this area.

The used sensors have a high noise level compared with the occurring lenstop acceleration, but this level is low enough to use the sensors for measuring acceleration in the targeted frequency area. The use of the airmount system as actuator can not disturb the vibration isolation function of this system. This requirement is complied with by restricting the actuation signal to frequencies that are not used for the vibration isolation function.

The process between the actuating system and sensors is very complex. Frequency response function measurements show a highly entangled process, the presence of non-minimum phase zeros and unavoidable cross-talk. Limitations on performance follow directly from modeling errors that can not be avoided because of the process complexity. Performance restrictions are also imposed by the non-minimum phase zeros.

Three controller design methods are tried out. It quickly becomes clear that simple proportional design can not cope with the process complexity. With the LQG controller design method it is not possible to suppress certain resonance frequencies considerably while effectively restricting performance deterioration at other frequencies. The H_∞ design method with the proper augmented plant setup does provide this possibility. An augmented plant that leads to a mixed-sensitivity design is not suitable, because this design causes pole-zero cancellations which provide bad robustness properties. Using an augmented plant that leads to a four-block problem prevents these cancellations and an acceptable controller can be obtained.

With the H_∞ design method a controller is designed that provides substantial damping of lenstop vibrations. Implementation of the controller shows a considerable reduction of lenstop acceleration and reticle stage position error in a production situation.

This report shows that it is feasible to damp lenstop vibrations with the use of the airmount system. Stability robustness could not be guaranteed and is left to be researched when it is intended to apply a similar control system in a wafer scanner.

Contents

Summary	ii
1. Introduction	1
1.1 ASML Background	1
1.2 Research assignment: damping of lenstop vibrations	2
1.3 Outline.....	2
2. Disturbance: Lenstop vibrations	3
2.1 Resonances.....	3
2.2 Resulting RS position error.....	4
3. Design restrictions: Sensor and Actuator.....	9
3.1 Accelerometers.....	9
3.2 The airmount-system.....	10
4. Measuring and modeling the process.....	15
4.1 Measuring the frequency response functions	15
4.1.1 <i>The process under inspection</i>	15
4.1.2 <i>Measurement results</i>	16
4.1.3 <i>Actuation directions choice</i>	16
4.2 Modeling	17
4.2.1 <i>SISO or MIMO</i>	17
4.2.2 <i>Black-box modeling and reduction</i>	17
4.3 Performance restrictions.....	20
4.3.1 <i>Process characteristics</i>	20
4.3.2 <i>Process uncertainty</i>	22
5. Controller design	25
5.1 Controller evaluation.....	25
5.1.1 <i>Simulations</i>	25
5.1.2 <i>Controller requirements</i>	26
5.1.3 <i>Controller performance evaluation and comparison</i>	26
5.2 Simple proportional design	27
5.3 LQG design	28
5.4 H_∞ design.....	30
5.4.1 <i>Augmented plant setup 1</i>	31
5.4.2 <i>Augmented plant setup 2</i>	35
5.4.3 <i>Augmented plant setup 3</i>	38
5.4.4 <i>H_2 design</i>	39
5.5 Designed controllers comparison	40
6. Controller implementation	41
6.1 Controller reduction	41
6.2 Controller digitization	42

6.3	Implementation results	43
6.3.1	Results during airmount noise.....	43
6.3.2	Results during the run of a job.....	44
7.	Conclusions and recommendations	45
7.1	Conclusions	45
7.2	Recommendations	46
Literature.....		47
Appendix A: Disturbance PSD-s.....		48
Appendix B: Measured SISO FRF-s		50
Appendix C: Model compared with measurements		56
Appendix D: Proportional design		58
Appendix E: LQG Design.....		64
Appendix F: H_∞ design, augmented plant setup 1		68
Appendix G: H_∞ design, augmented plant setup 2		71
Appendix H: H_∞ design, augmented plant setup 3		73
Appendix I: Controller implementation results.....		78

1. Introduction

This Master of Science thesis covers the research that has been carried out by the author at ASML Lithography (ASML), to graduate as an electrical engineer at the Eindhoven University of Technology. In this chapter first a short description of the company ASML is given. After that the research assignment will be explained. In the last section the structure of this report is outlined.

1.1 ASML Background

ASML develops and manufactures photolithographic systems for the semiconductor industry. Photolithography is the technology which makes it possible to put complex patterns on so-called wafers and is essential for the fabrication of integrated circuits.

A photolithographic system for semiconductor production contains a variety of complex components, including an illumination source, a reduction lens, precise alignment and staging subsystems, and reticle (mask) and wafer-transfer robotics. All of these components are integrated into a sophisticated and complex system known as a wafer stepper or a Step&Scan system.

The name wafer stepper is derived from the fact that it makes an exposure of a circuit pattern on the wafer, then 'steps' to the next area of the wafer and repeats the process until the circuit pattern is 'printed' across the wafer's surface in an array of dies, which will become individual, finished chips.

The Step&Scan system is a more recent developed product of ASML. The die surface needed for chips increased because of the development of more advanced integrated circuits. It is hard and expensive to construct a lens with a large accurate projection area. At the Step&Scan systems the reticle stage and wafer stage make a scanning movement (in opposite direction). As a consequence only a small slice of the lens has to be very accurate. Another advantage is that throughput, a very important property for photolithographic systems, of the Step&Scan system is greater than that of the wafer stepper. Figure 1 shows a picture of a Step&Scan system. With these systems linewidths of $0.15 \mu\text{m}$ (1/500 of the thickness of a human hair) can be reached. The rest of the report is applicable to the Step&Scan systems and they will simply be called wafer scanners or scanners.

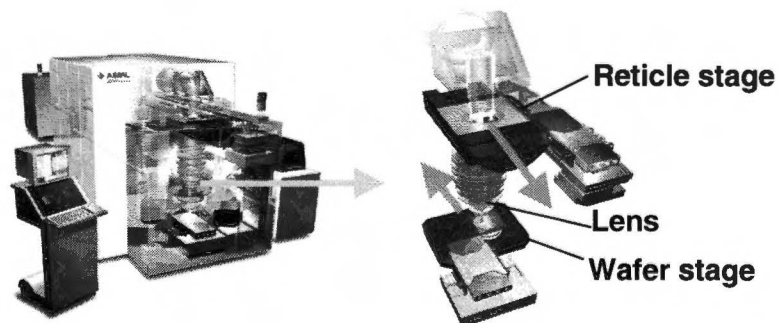


Figure 1: ASML Step and Scan system

ASML was founded in 1984 and nowadays is second in the world market of producers of wafer steppers and scanners. ASML has around 3500 employees and offices in Europe, Asia and the United States. Its headquarters are in Veldhoven, the Netherlands.

1.2 Research assignment: damping of lenstop vibrations

Accuracy is essential for the photolithographic process. At the moment lens vibrations are limiting factor in the achieved accuracy of the projection within the scanner. To limit the influence of the lens vibrations these vibrations are measured at the top of the lens with accelerometers and the acquired signal is used in a feedforward loop for the reticle stage that has to follow the lens. The position of the lens and reticle stage in the scanner can be seen in figure 1. Because this solution is not totally satisfying other additional solutions are researched. One possible additional solution is to actively damp the lens vibrations to decrease their influence.

The research assignment was to design the optimal controller to damp the vibrations at the top of the lens. Preconditions and thus design restrictions were that the used actuator is the so-called airmount-system and that the used sensors are the mentioned accelerometers. The controller has to be optimized for one scanner type, the PAS5500/800. A drawback was that during the research a scanner of this type did not exist up to halfway the research period and the available measurement time was very scarce. Therefore it was necessary to make some deductions from another machine type, the PAS5500/500, and assume similarity with the /800.

Figure 2 shows the scheme of the control system that has to be designed. It is obvious that, because the lenstop vibrations have to be damped, the reference value of the lenstop acceleration is zero.

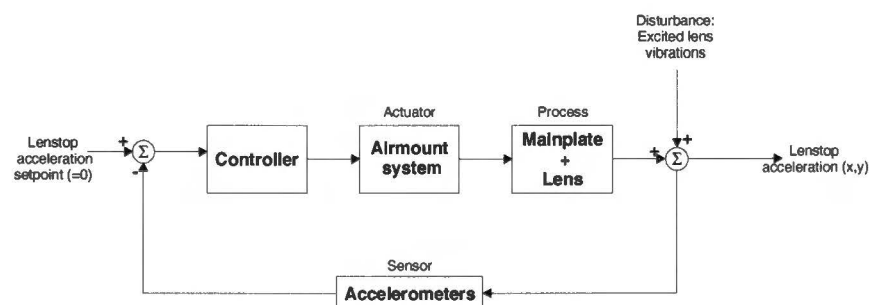


Figure 2: Control loop to be designed

1.3 Outline

The outline of this report coincides much with the layout depicted in figure 2. In chapter 2 the disturbance that needs to be damped will be described. After that the design restrictions, these are the sensor and actuator, will be discussed in chapter 3. Chapter 4 treats the process, i.e. the response of the mainplate with lens to actuation. The process will be measured, modeled and performance restrictions that result from the process will be outlined. Chapter 5 is the main chapter of this report, as it discusses the controller design, including simulation results. In chapter 6 the controller implementation results are shown. Finally, chapter 7 contains conclusions and recommendations.

2. Disturbance: Lenstop vibrations

This chapter discusses the disturbance, i.e. the lenstop vibrations, that has to be damped. First is explained what causes these vibrations and in which frequency area they occur. After that is discussed which lenstop vibrations are the most important to be damped.

2.1 Resonances

Figure 3 shows an illustration of the layout of the scanner. The location of the lens, airmounts and sensors are depicted. The sensor and airmount system are discussed in the next chapter.

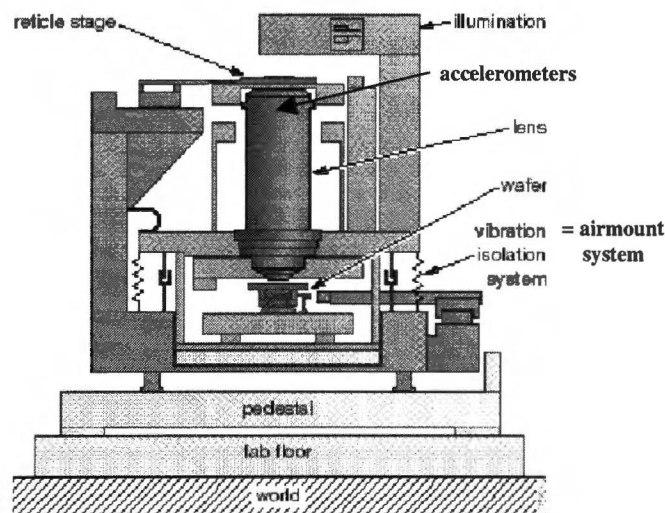


Figure 3: PAS5500 body

Lens vibrations are the result of resonances in the scanner. These resonances can be caused by acoustics, a fan for temperature control etc., but are especially excited by movements in the scanner, e.g. movement of the wafer stage and reticle stage (RS). To be able to design an appropriate controller, it is necessary to know the shape of these resonances. Interesting to know are the resonance modes concerning movement, frequency and the resulting amplitude at the lenstop.

Measurements have been done to determine the lenstop vibrations, on a /500 and a /800 system, with the use of the sensors that were depicted in figure 3. Table 1 shows the measurement situations, the system type, the root mean square (RMS) values of the measured lenstop acceleration and the figures where a power spectrum density (PSD) plot of the measured acceleration can be found. These figures can be found in appendix A. The RMS values and PSD plots result from the mean values that were taken from 15 tracefiles in each situation.

ref same vathing.

which?

With the ‘Rx and Ry white noise situation’ is meant that existing PAS 5500 software was used to inject noise on the airmounts Lorenz motors (see next chapter) in a rotation direction around the X (Rx) and Y (Ry) axis. The coordinate system will be depicted in the next chapter. Note that in these artificially excited experiments, the white noise disturbance is effected by the airmount system, while in actual operation (run of a job) the lens is excited especially by the moving stages both at the bottom and at the top. The lenstop acceleration (LA) is measured with two accelerometers, one measures the acceleration in X and one in Y direction.

Table 1: Measurement results of lenstop acceleration

Situation	Scanner type	LA RMS value (mm/s ²)		Figure Appendix B
		X	Y	
rest ¹⁾	/500	2.39	2.76	A.1
Rx and Ry white noise	/500	4.75	7.23	A.2
Run of a job ²⁾	/500	5.09	6.83	A.3
Rx and Ry white noise	/800	6.20	5.87	A.4

- 1) Although this is a rest situation, lenstop vibrations are still present due to acoustics and temperature control.
- 2) This is the most important situation. This will give an impression of lenstop vibrations in a production situation. Implementing a damper for lenstop vibrations has eventually to lead to a better performance in the production situation.

The RMS values will be used to calculate a performance improvement percentage that will be obtained with designed controllers. The PSD plots from appendix A are very useful for recognition of the resonance frequencies and derivation which resonances are the most important to be damped. Table 2 and 3 show the resonance frequencies (with the direction in which they occur between brackets) of respectively the /500 and /800 system that stand out clearly in the PSD plots of appendix A. Probable causes have been denoted also.

Table 2: Resonance frequencies of lenstop vibrations of /500

Frequency [Hz]	Probable Cause
52.5 (Y) , 56.2 (X and Y), 59.2 (X)	Z-frame ¹⁾ leafsprings twisting modes
73.2 (Y)	Z-frame leafsprings bending mode
95.2 (X)	Rigid body movement lens
98.9 (X and Y), 100.1 (X and Y)	Other lens modes
107.4 (Y)	Eigenmode of sensorplate

- 1) Frame on which the reticle stage is mounted.

Table 3: Resonance frequencies of lenstop vibrations of /800

Frequency [Hz]	Probable Cause
69.0 (Y)	Z-frame leafsprings bending mode
76.9 (X and Y)	Other Z-frame mode
84.2 (X and Y), 89 (Y)	Rigid body movements lens
102 (Y)	Eigenmode of sensorplate

2.2 Resulting RS position error

The question remains which are the most important resonance frequencies to damp. One has to keep in mind that lenstop displacement is the disturbance factor when producing, and not lenstop acceleration. Acceleration at frequency f has to be multiplied with a factor $(1/2\pi f)^2$ to obtain the displacement at that frequency. It can easily be noticed that low frequency lenstop

acceleration will have an excessive lenstop displacement compared with higher frequency accelerations. This would mean that the high frequency lenstop accelerations could be ignored. However, the reticle stage position error is the real limiting precision factor when producing. This position error is measured and controlled relative to the lens position. The controller is very well able to reject low frequency disturbance (in this case lenstop displacement) up to around 20 Hz, which would mean that low frequency lenstop accelerations could be ignored. The previous shows that some measurements and/or calculations are needed to determine which resonance frequencies have the most influence on the RS position error, and thus are the most interesting to damp.

The control loop concerning this problem can be seen in figure 4. The controller in the figure consists of a PID-controller, a second-order low-pass filter and a first order low pass filter. The controller also consists of a few notch-filters but they can be ignored for convenience, because the notches are placed at frequencies well above the area of interest. This leads to the following transfer function for the controller:

$$C(s) = K_p \cdot \left(1 + \frac{s}{2\pi f_d} + \frac{2\pi f_i}{s}\right) \cdot \left(\frac{s}{2\pi f_2}\right)^2 + 2b \frac{s}{2\pi f_2} + 1)^{-1} \cdot \left(\frac{s}{2\pi f_1} + 1\right)^{-1}$$

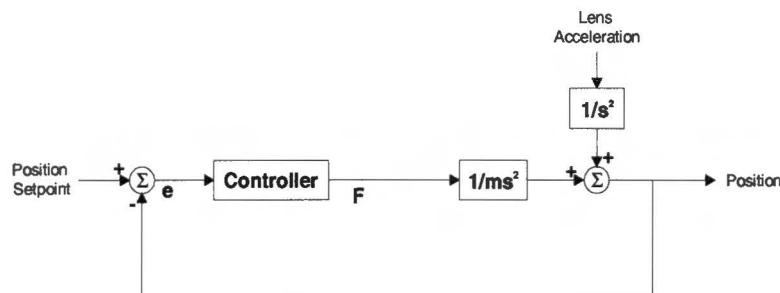


Figure 4: RS position control loop, simplified

The present solution for reducing the lenstop acceleration influence with use of the accelerometers, the lenstop acceleration feedforward is not depicted and left out in this derivation. Both X- and Y-directions are controlled with separate controllers and have their own parameters. The parameters of proto1/500 (the /500 machine on which measurements took place) differ slightly from the parameters on production machines. In this case the parameters used on proto1/500 are taken. These parameters can be seen in table 4. In figure 4 the parameter m represents the mass of the reticle stage which is 10 kg.

Table 4: Proto1/500 RS controller parameters

Parameters	X-direction	Y-direction
K_p	2e6	4.5e6
f_i	30	50
f_d	45	70
f_1	1250	1250
b	0.5	0.5
f_2	500	1250

The sensitivity of the RS position error to lenstop acceleration was calculated using figure 5 and the given transfer function of the controller. It was found out that a delay was present that could not be ignored, and therefore the delay can be seen in the sensitivity loop. This delay consists of 0.5 sample time because of the zero-order-hold of the digitally implemented controller and an

I/O delay of 0.3 sample time. The sample time is 0.4 ms because the controller operates at 2500 Hz. The magnitude of the calculated sensitivities can be seen in figure 6.

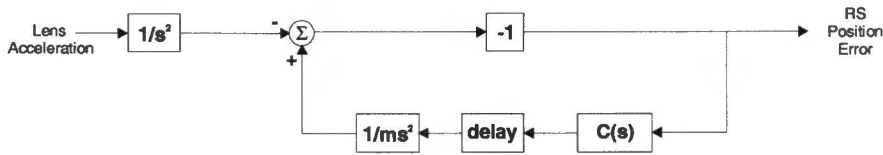


Figure 5: Sensitivity loop with delay

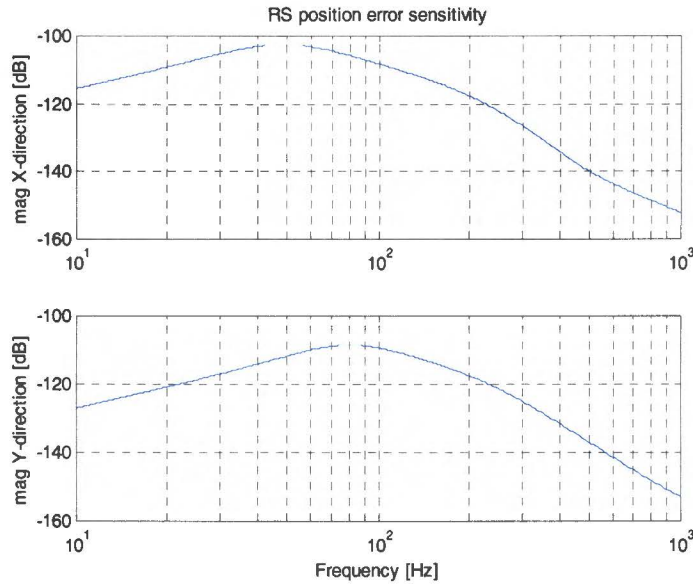


Figure 6: RS position error sensitivity to lenstop acceleration

The calculated sensitivities were used to calculate the RS position error that results from measured lenstop acceleration, according to the following formula:

$$PE_c(f) = |S(j2\pi f)|^2 \cdot LA(f)$$

$\frac{m^2}{Hz} = S^2 \cdot \frac{m^2}{s^2 \cdot Hz}$
 $S = \frac{m}{s^2} = [s^{-2}]$

PE_c = calculated position error in [m²/Hz]
 LA = lens acceleration in [(m/s²)²/Hz]

In the second and third situation indicated in table 1, the RS position error was also measured. Figure 7 shows the measured and calculated RS position error PSD in these situations. It can be seen that the measured RS position error matches the calculated RS position error rather well. Therefore it can be concluded that indeed the lenstop acceleration that is measured, causes the RS position error and thus can be used in a controller for performance improvement. This was expected, but what is more important, is that we now can deduct from the RS position error PSD-s which resonance frequencies are the most important to be damped.

It can be concluded that although low frequency lenstop accelerations will lead to much more lenstop displacement, they can be ignored, because they do not lead to a considerable RS position error. This follows from the sensitivity functions (figure 6) and is confirmed by RS position error calculations and measurements (figure 7). These last measurements and measurements of the lenstop acceleration show that the most important resonance frequencies to focus on are around 55 and 95Hz in X-direction and 55, 73, 100 and 107Hz in Y-direction. We

broaden this by saying that the frequency area in which the performance has to be improved is the 50-110 Hz area. Although this was deduced from a /500 machine, it is assumed that this frequency area holds for a /800 machine, despite slight differences in the RS controller parameters and a few resonance frequencies. Although in table 3 no resonance frequencies could be seen for the /800 in the 50-60 Hz area, they are present. These resonances are excited especially during a job, of which no measurement data was available for the /800.

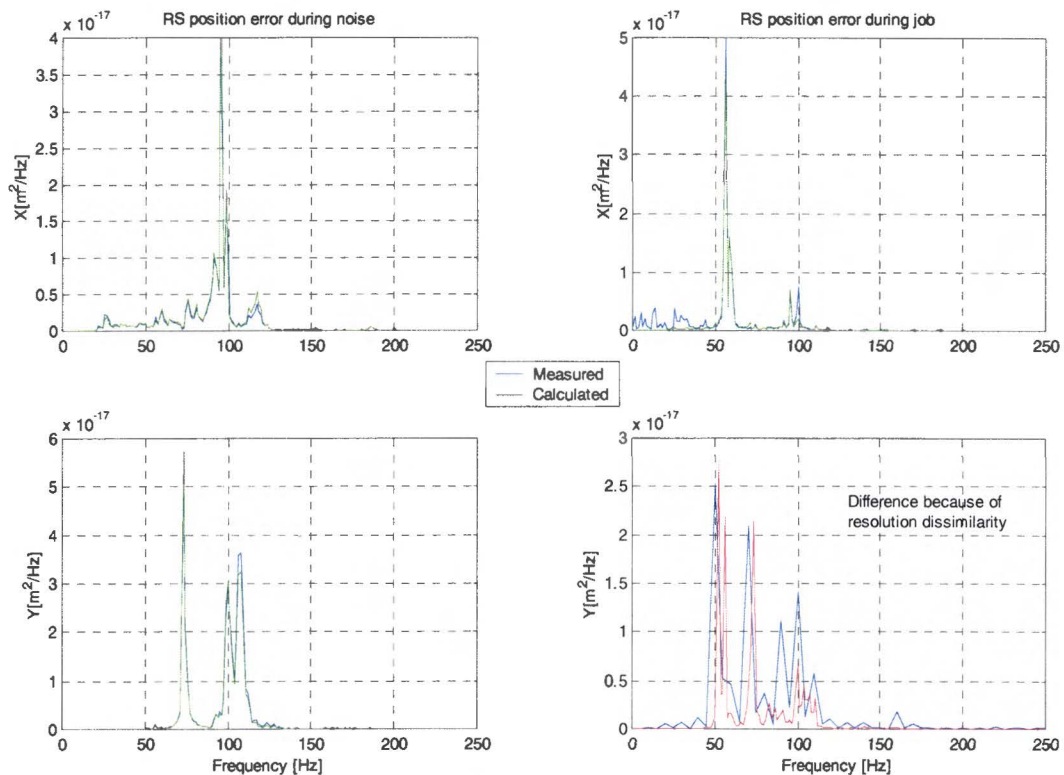


Figure 7: Measured and calculated RS position error PSD-s

To give an impression of the degree of complexity of the problem the following comparison can be made. The amplitude of the RS position error is up to $0.1 \mu\text{m}$. The height of the lens is around 1 meter. The airmount system that is used as an actuator to damp the lenstop vibrations is located at the bottom of the lens. So, damping the lenstop vibrations with this system can be compared with damping $10 \mu\text{m}$ vibration amplitudes of a 100 meter high building from below.

quite good.

3. Design restrictions: Sensor and Actuator

As mentioned in the introduction, there were some preconditions for the control loop that had to be designed. The used sensors had to be the accelerometers mounted on the lenstop. The so-called airmount system had to be used as actuator. In this chapter first the specifications of the accelerometers will be treated. After that an explanation about the airmount-system will be given. Recall figure 3 of the previous chapter for the location of the lens, the airmounts and the accelerometers.

3.1 Accelerometers

The accelerometers are mounted on the top of the lens of the scanner. One accelerometer measures the acceleration of the lenstop in X-direction and one accelerometer measures the acceleration in Y-direction. In the next section these directions will be specified. At the PAS 5500 systems the accelerometers used are of the type FA 201-15 from J&M instruments. Such an accelerometer comprises a micromachined silicon structure whose Wheatstone bridge format piezoresistors change their value proportionally to the acceleration applied. The bandwidth of this sensor is around 1200 Hz, which is abundantly sufficient when it is used in a control loop that has to be active up to 110 Hz. The phase shift of the sensor at 110 Hz is around 7 degrees.

The sensor noise of the used type of accelerometers has been measured within ASML, the results of these measurements can be seen in figure 8. The same figure also shows the measured PSD-s of the lenstop acceleration, with Rx and Ry noise on the /800. It can be seen that the noise level is rather high compared with the measured acceleration level. In a rest situation this

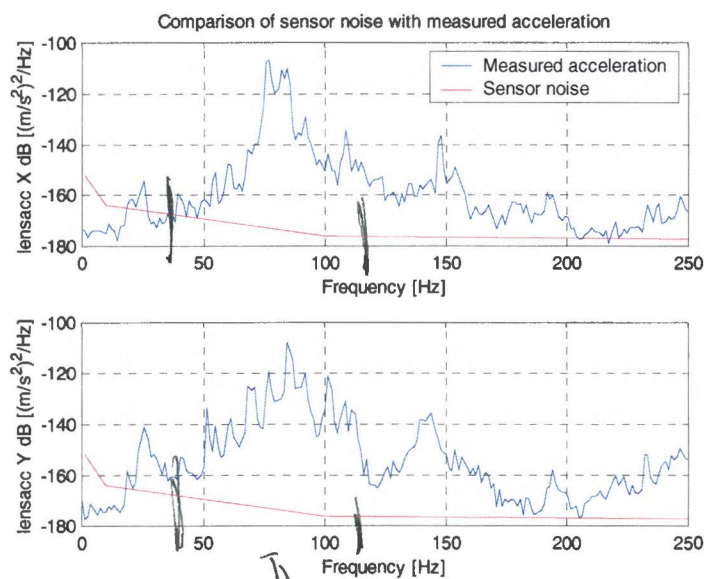


Figure 8: Comparison sensor noise with measured acceleration

will be worse. Furthermore it is known that the noise level fluctuates heavily per sensor. The RMS value of the noise is around 1.1 mm/s², which is high when compared with the measurements from table 1.

An interface between the sensor and the sensor board, called Feed Forward Acceleration Sensor (FFAS), has been developed by ASML. This interface has the function to amplify and filter the sensor output signal, for instance to filter out the dc offset. It is sufficient to note that the bandwidth of the interface exceeds the bandwidth of the accelerometer, and therefore does not cause a restriction.

3.2 The airmount-system

The airmount (AM)-system is an active vibration isolation system with which the ASML scanners are equipped. It was developed by ASML in close co-operation with a German company, I.D.E. GmbH. The airmount system is built in the scanner between the baseframe and the mainplate. The baseframe is the frame under the scanner on which all parts that are fixed to the real world are mounted. The mainplate is the part of the machine that is suspended and that contains all the critical assemblies of the scanner that must be kept at low acceleration levels, specified below 1 mm/s².

This gives the vibration isolation system two functions:

1. Isolate the vibrations on the mainplate.
2. Keep the mainplate with all its subsystems in a fixed position relative to the base frame.

Figure 9 shows a simplified front and top view of the scanner and also contains a coordinate system, which will be referred to in the rest of this report. It can be seen that the airmount-system exist of three airmounts, positioned at the corners of the triangular mainplate.

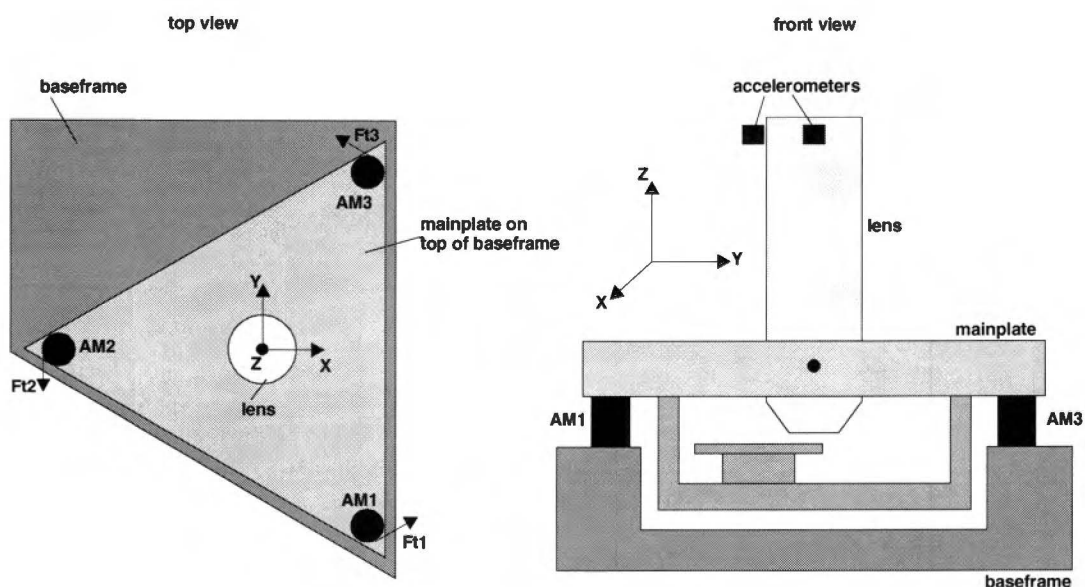


Figure 9: Simplified top and front view of scanner

A thorough explanation of the AM-system will not be given, because it is not the topic of this research. What is important to know, is that each airmount among other devices is equipped with two Lorentz-motors. One motor actuates a force in z-direction and one motor actuates a force in tangential direction. These motors are the actuators that have been used to excite the

lens artificially by white noise (see chapter 2) and will be used to damp the lens vibrations, by injection of an additional control signal in the corresponding power amplifiers. It is obvious that this additional injection can not disturb the vibration isolation system. Because the highest bandwidth of the loops in the airmount system is around 2 Hz, this requirement can be complied with by making sure that the additional injection signal only exist in a higher frequency area, e.g. above 5 Hz. In this way a separate actuation system can be obtained. This method is depicted in figure 10.

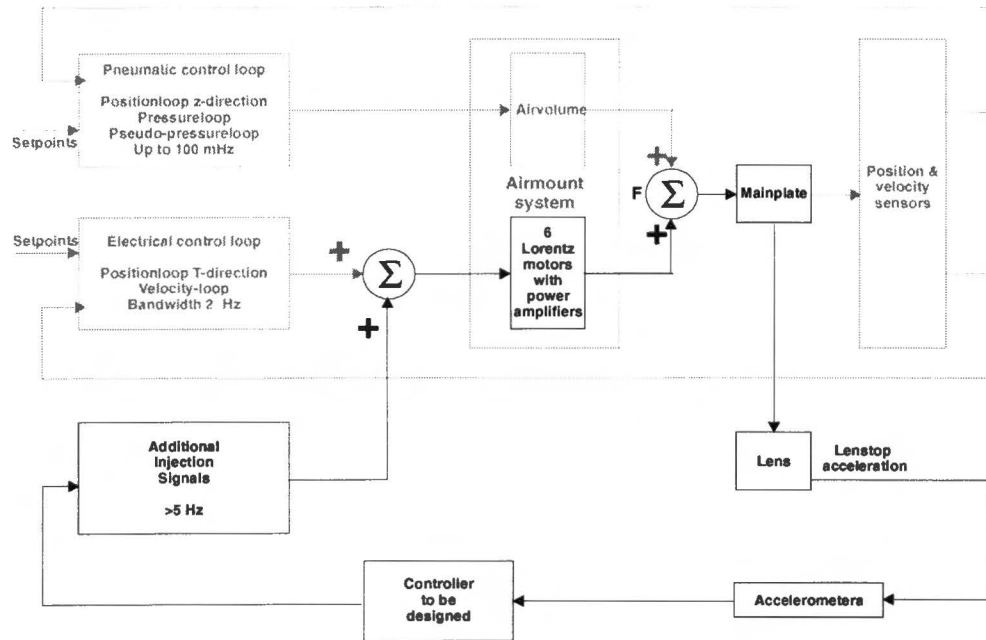


Figure 10: Additional signal injection in airmount system

When using the airmount system in this way, it is possible to excite the mainplate in numerous ways. The six Lorentz motors can be actuated in different proportions to obtain different actuation directions. It is desired to obtain six degrees of freedom (DOF) accurate actuating directions: translations in X, Y and Z direction and rotations around the X, Y and Z-axis (pointed out as X, Y, Z, Rx, Ry and Rz respectively). The reason for this intention is that when there is no cross-talk in the system, each accurate actuating direction will only cause lenstop acceleration in at most one measured direction, X or Y. This would mean that the design of a controller would be less difficult. Q

The above is emphasized because it is not very easy to obtain these accurate actuating directions with the six Lorentz-motors. Figure 11 shows the important geometry of the actuating system. The coordinate system is the same as in figure 9. The origin, which lies in the geometric center of the triangle, is the place where the lens is located along the z-axis.

When the center of mass of the mainplate with the lens is located in the origin, it can easily be calculated in which proportion the airmounts have to be actuated to obtain accurate actuating directions. But, the center of mass is not located in the origin. It is known that its location in the 2-dimensional plane is fixed at approximately [0,100 mm]. This means that when actuating the Lorentz-motors in the proportion calculated when one does not comply with this shift of the mass-center, that clear actuating directions will not be obtained. There will be some cross-talk and for instance actuation in Rx direction will also cause a (smaller) Z-translation and Ry-rotation. It should be noted that ASML airmount software does not take this shift of the mass center into account.

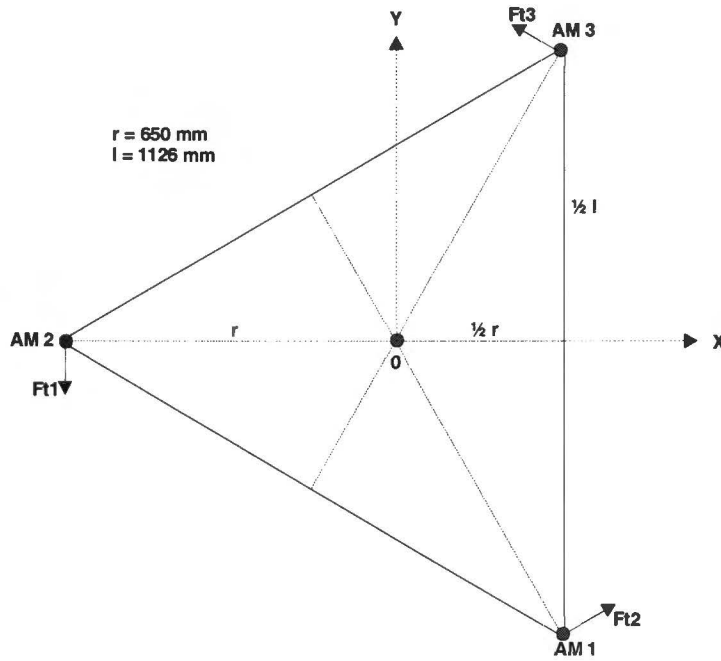


Figure 11: Geometry of the actuation system

It was not possible to calculate the correct actuating proportions, because inertias of the machine were not known. That is why the proportions were obtained experimentally. This was done by individually adjusting the gain of the input voltages of the power amplifiers of the Lorentz-motors and measuring the displacement of the airmounts, with the position sensors that are mounted on the airmounts. These sensors measure the displacement in tangential and vertical direction. This displacement could then be transformed in the actuation directions with the following transformation matrix:

$$\begin{bmatrix} X \\ Y \\ Z \\ R_x \\ R_y \\ R_z \end{bmatrix} = \begin{bmatrix} \frac{1}{3}\sqrt{3} & 0 & -\frac{1}{3}\sqrt{3} & 0 & 0 & 0 \\ \frac{1}{3} & -\frac{2}{3} & \frac{1}{3} & 0 & 0 & 0 \\ 0 & 0 & 0 & \frac{1}{3} & \frac{1}{3} & \frac{1}{3} \\ 0 & 0 & 0 & -\frac{1}{l} & 0 & \frac{1}{l} \\ 0 & 0 & 0 & -\frac{\sqrt{3}}{3l} & \frac{2\sqrt{3}}{3l} & -\frac{\sqrt{3}}{3l} \\ \frac{\sqrt{3}}{3l} & \frac{\sqrt{3}}{3l} & \frac{\sqrt{3}}{3l} & 0 & 0 & 0 \end{bmatrix} \begin{bmatrix} T1 \\ T2 \\ T3 \\ Z1 \\ Z2 \\ Z3 \end{bmatrix}$$

In this transformation formula the most right column vector represents the measured displacement (T stands for the tangential displacement and Z for the vertical displacements in [m], the number is the airmount number). The left column vector represents the displacement in the 6 DOF in [m] respectively [rad].

The gains of the input voltage for each power amplifier for the Lorentz-motors were tuned until accurate actuation directions were obtained. Table 5 shows the relative actuation gains used when one does not account for the shift of the mass center and it shows the tuned relative actuation gains.

Table 5: Relative actuation gains

	X		Y		Rz	
	no shift	tuned	no shift	tuned	no shift	tuned
Ft1	1	1.41	1	0.70	1	1.00
Ft2	0	-0.06	-2	-1.60	1	1.00
Ft3	-1	-1.53	1	0.70	1	1.00
	Z		Rx		Ry	
	no shift	tuned	no shift	tuned	no shift	tuned
Fz1	1	0.73	-1	-1.16	-1	-0.83
Fz2	1	1.13	0	0	2	1.83
Fz3	1	1.15	1	1.84	-1	-0.33

In this way an actuating system was obtained that could actuate the mainplate with lens fairly accurate in the mentioned 6 DOF. The design freedom concerning actuation which is left is the choice which actuation directions of these 6 DOF will be used in the control loop that has to be designed. This will be dealt with in the next chapter.

4. Measuring and modeling the process

The subject of this chapter is the process, i.e. the response of the mainplate with lens at the lenstop accelerometers to actuation with the airmount system. First the method of measuring this response is treated and the results are presented. A choice for actuation directions will be made. After that the modeling of the process is discussed. Finally, it will be shown that the process and the model of this process lead to restrictions on the performance that can be obtained with the control loop.

4.1 Measuring the frequency response functions

4.1.1 The process under inspection

In the previous chapter, the actuation system was discussed. This system can now be used to obtain process knowledge. First a choice has to be made which transfer function will be determined, because there are various signals available to take as input and output signal. Possible input signals are the input voltage of the amplifiers, the input current of the Lorentz-motors or the applied force or torque on the mainplate. Because the difference between these signals is a known static, frequency independent, gain, it is easy to convert the measured transfer functions to transfer functions with another input signal.

It was chosen to determine the transfer function between the input voltage of the power amplifiers of the AM Lorenz motors in [V] and the lenstop acceleration in [m/s^2]. This because the output signal of the controller which has to be developed will be an input voltage of the power amplifiers. And the lenstop acceleration is the variable to be controlled. So, the desired transfer function is the H process, depicted in figure 12. The expected average slope of the transfer function in [dB] is 0 dB per decade, because:

$$V \rightarrow I \rightarrow N(Nm) \rightarrow m/s^2$$

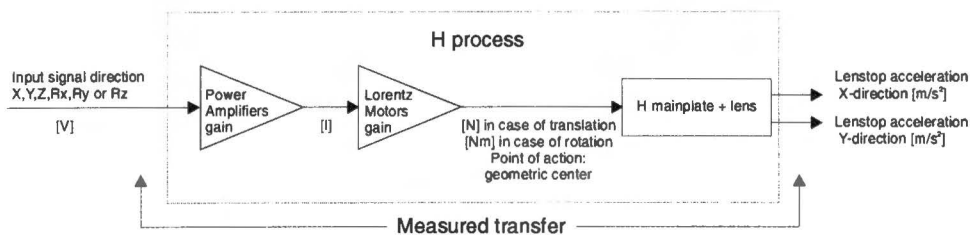


Figure 12: FRF measurements

The measured frequency response functions (FRF-s) will be used for the design of the control loop. To have an insight in the physical interpretation, table 6 shows a recalculation to obtain the transfer function in [N] or [Nm] to [m/s^2]. To calculate these gains, knowledge about the power amplifiers, motor-constants, actuation directions and distances of the airmounts to rotation axes have to be known. The last two were depicted in figure 11. The power amplifiers

are of the type DCPA50/2 (direct current power amplifier 50 V, 2 A, gain 0.25 A/V). The motor constants are 43 N/A for the horizontal motors and 87 N/A for the vertical motors. This leads to the gains shown in table 6.

Table 6: gain conversion values

Actuation direction	Applied force/torque per actuation volt
X	27.4 N
Y	24.7 N
Z	65.4 N
Rx	36.7 Nm
Ry	34.1 Nm
Rz	21.0 Nm

4.1.2 Measurement results

Conform figure 12, SISO FRF measurements have been performed with the swept sine method with both a SigLab system and with a spectrum analyzer (HP35670A), which lead to the same results. The measurements were performed on the testrig/800. (Twelve (6 DOF → lenstop acceleration X,Y) SISO FRF-s have been obtained. They are displayed in appendix B. It was checked that the FRF-s maintain a linear behavior by actuation at different input voltages. Coherence during all measurements was always close to one.

In general can be said about the measured FRF-s that they are very entangling. Close inspection shows a lot of anti-resonances – resonances which represent the uncoupling of masses. The resonance at 84 Hz represents the uncoupling of the lens itself. A tremendous negative phase shift can be seen in all measured FRF-s that depend on cross-talk (e.g. Ry-actuation to Y acceleration). This phase shift is also present at the FRF-s that do not depend on cross-talk (e.g. X actuation to X acceleration) for frequencies higher than around 100 Hz. It is important to mention this, because this phase shift will be one of the burdens when designing a controller.

4.1.3 Actuation directions choice

A choice has to be made which actuation directions will be used to damp the lenstop vibrations. The main criterion is to use those actuation directions with which damping in X and Y direction is very well possible but the process model can be kept as simple as possible:

- There is more than one actuation direction required; there are two acceleration directions that need to be damped. With an actuator acting in only one direction it is not possible to control both directions independently.
- The Z and Rz directions are the least likely to be used. They depend on cross-coupling for both the X and Y acceleration direction. This can also be seen in the frf-s: the amplitude plots are even more entangled for both acceleration directions which will lead to a higher order model. Furthermore the phase shift is very high, also at low frequencies, in both directions.
- Good options are an X,Y combination and an Rx, Ry combination. The X,Y combination is preferred because the transfer functions are a bit more clear: The (anti)resonances are better distinct and the large negative phase shift starts occurring at higher frequencies (for the actuation-acceleration combination that does not depend on cross-coupling). These directions should give the simplest model. Large cross-coupling is present in both actuation combinations, so this is no argument to choose a certain combination.
- It is not necessary to use more than two actuation directions.
- X,Y actuation is less powerful than Rx, Ry actuation (see table 6), but powerful enough for this application.

4.2 Modeling

4.2.1 SISO or MIMO

In the previous section it was made clear that the X and Y actuation directions of the airmount system will be used in the control loop. An important choice is whether a MIMO control loop or multiple SISO control loops will be designed. This choice determines if the process is modeled with multiple SISO transfer functions or if a MIMO model is to be obtained, which leads to some additional modeling techniques.

At first sight it seems clear that a MIMO controller is needed, because the magnitude of the transfer functions that depend on cross-coupling ($X \rightarrow Y$ and $Y \rightarrow X$) is almost equal to the magnitude of the $X \rightarrow X$ and $Y \rightarrow Y$ transfer functions at the resonance frequencies. This is explicable by the fact that a resonance mode occurs in an arbitrary fixed direction. That direction is independent of the actuation. The choice to design a MIMO controller can be founded with the so called relative gain array.

The concept of relative gain array (RGA) can be used to measure the degree of cross coupling or interaction in a system. For an arbitrary square matrix A, it is defined as:

$$\text{RGA}(A) = A \cdot (A^{-1})^T$$

Here \cdot denotes (like in Matlab) element-wise multiplication. RGA of a diagonal, thus uncoupled, matrix is the unit matrix. The deviation of RGA from the unit matrix can be taken as a measure of cross coupling between x and y in the relation $y = Ax$. For this case RGA can be considered as a function of frequency:

$$\begin{bmatrix} |\text{lensacc}X(f)| \\ |\text{lensacc}Y(f)| \end{bmatrix} = A(f) \cdot \begin{bmatrix} |\text{actuation}X(f)| \\ |\text{actuation}Y(f)| \end{bmatrix} \quad A = \begin{bmatrix} |H_{x \rightarrow x}(f)| & |H_{y \rightarrow x}(f)| \\ |H_{x \rightarrow y}(f)| & |H_{y \rightarrow y}(f)| \end{bmatrix}$$

$$\text{RGA}(A(f)) = A(f) \cdot (A(f)^{-1})^T$$

In figure 13 the elements of the RGA matrix for the measured system are plotted. This figure shows that in the frequency area of interest (identified in chapter 2), the RGA deviates very much from the unit matrix, and therefore the cross coupling is very large in that frequency area. It can also be seen that the cross coupling is highly frequency dependent, and therefore can not be circumvented by using uncoupling matrices. So the cross coupling can not be neglected and a MIMO controller is needed. RGA calculations were also done for the Rx, Ry actuation combination (not depicted) to assure that in this case a MIMO controller also was necessary. This was the case, so there was no reason to switch to this actuation combination. More information about RGA can be found in [10].

4.2.2 Black-box modeling and reduction

Since there is no information available about the process except for the measured FRF-s from the two inputs to the two outputs, the modeling is completely black-box. The steps carried out to obtain the model are described below:

Step 1: Fit the SISO FRF-s.

The SISO FRF-s have been fitted with the use of the Matlab function `invfreqs`. The fitting procedure was a combination of methodically approach and 'trial and error'. Weights have been assigned in such a way that the fit in the frequency area of interest matched well. Fine tuning has been done by trial and error changing the number of poles and zeros and adjusting the

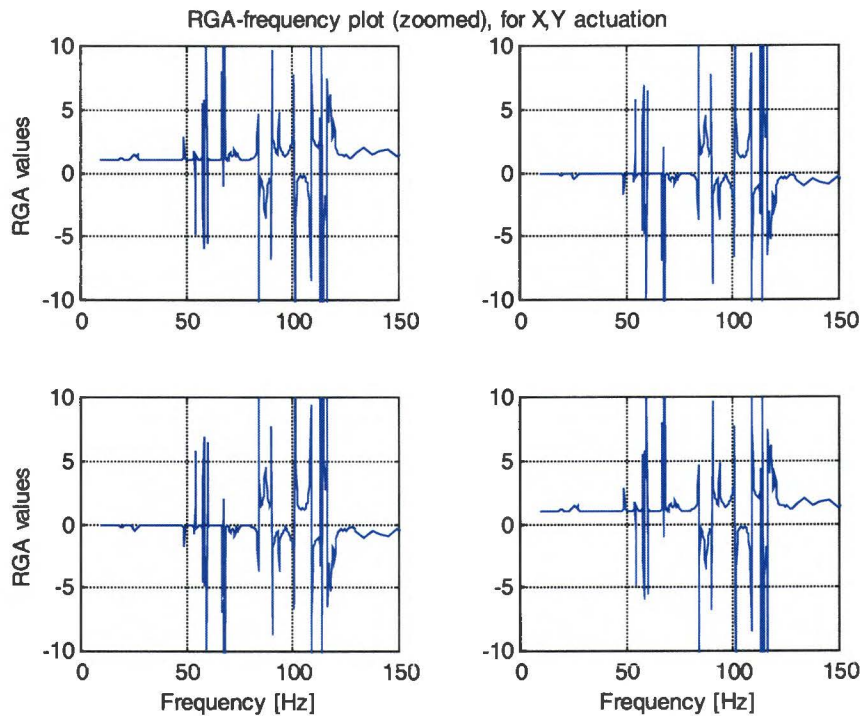


Figure 13: Process RGA plot

weights. The result was four transfer functions of the order 26,26,24 and 28 for respectively the $X \rightarrow X$, $X \rightarrow Y$, $Y \rightarrow X$ and $Y \rightarrow Y$ transfer functions.

Step 2: Transfer the SISO models to a MIMO model.

The SISO transfer functions were put in a transfer function matrix. With the use of Matlab this transfer function matrix system was transformed to a MIMO state space model. This model was consequently of the order $26+26+24+28 = 102$.

Step 3: Model reduction.

The obtained model was of the order 102, which is rather large when one wants to continue with calculations. Order reduction should be possible because:

- SISO fitting places the poles and zeros for each transfer function at a different frequency, also when they represent the same modes. This is one of the disadvantages of black-box SISO modeling, compared with grey-box or MIMO modeling. The process under research is far too complex to use a grey-box modeling approach.
- Some of the states of the model are more important than others. It is very likely that some states can be left out without increasing the incorrectness of the model too much.

In [10] 5 different methods for model reduction are described. The first two are truncation and residualization after the model has been put in the so-called Jordan form, with the eigenvalues ordered according to mode frequencies. Truncation is to be preferred when accuracy is required at high frequencies, whereas residualization is better for low frequency modeling.

The other three model reduction methods are balanced truncation, balanced residualization and optimal Hankel norm approximation. They all need a balanced realization of the system. A balanced realization is an asymptotically stable minimal realization in which the controllability and observability Gramians are equal and diagonal (and therefore can be addressed as Gramian). The controllability Gramian describes how much the different state variables are influenced by

the input. The observability Gramian describes how the different state variables contribute to the energy of the output.

The values in the Gramian are ordered so-called Hankel Singular Values (HSV). These values are a measure for the relevant significance of the different components of the state vector. After balancing the system, each state is just as controllable as it is observable, and a measure of a state's joint observability and controllability is given by its associated HSV. This is fundamental to the three model reduction methods, mentioned in the previous paragraph, which work by removing states having little effect on the system's input-output behavior.

A balanced representation of the system has been calculated by using the function `sysbal` from the μ -toolbox of Matlab. For more info about the Jordan form, truncation, residualization, balanced realization and HSV see [6] and [10].

All five reduction methods have been tried out. The two reduction methods which use the Jordan form gave a much worse result than the three methods using a balanced realization. This because in the first case states are removed ordered to frequency. Because the frequency areas that were not considered very important already were neglected during SISO fitting, much reduction could not be obtained.

The remaining methods measured up to each other for this system. The aim was to let the model come close to the measured FRF-s in at least the frequency area 50 – 110 Hz, because this was identified as the area of interest. Balanced residualization was finally evaluated as the method giving the best result when reducing the model. This can be explained, because in [10] it is pointed out that residualization works best in the low frequency domain. The three balanced methods did not have as much trouble matching the frequency domain up to well above 110 Hz (already simplified because of the SISO fitting) as with the frequency domain in the 50 Hz area. In that area the balanced residualization had the best performance, and thus was chosen as the best method.

The Hankel singular values of the balanced realization of the system are plotted in figure 14 with the values belonging to the states numbered above 20 also zoomed in. These plots are important in that fact that when reducing the model order, one can look in such a plot for large 'gaps'. When there are large gaps one can choose a 'cut-off' Hankel singular value, to make a

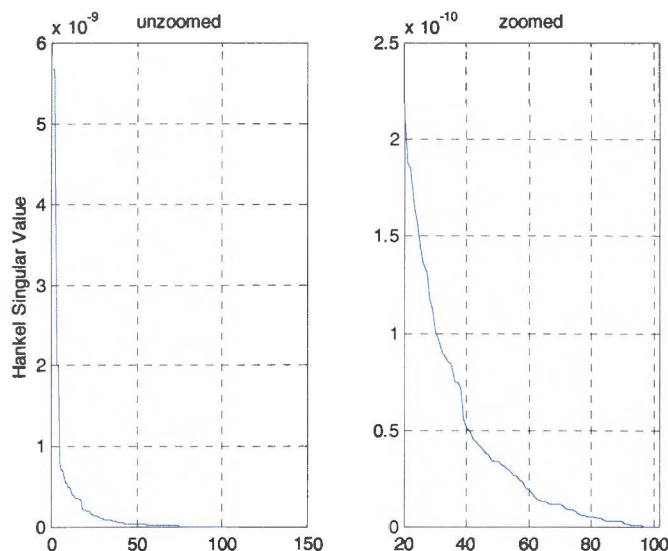


Figure 14: Hankel Singular Values of the unreduced model

founded choice of order reduction. It can be seen that in this system the gaps are not present (except at very low order, which would reduce the model too much), and therefore a more trial and error method concerning choosing order had to be used. The resulting order was 40.

It can be mentioned that the problem of the same resonance frequencies being placed at slightly different frequencies during SISO fitting, is not addressed and solved directly by the used model order reduction method. However, it became clear that still almost all 'double' resonance frequencies disappeared in the reduced model, when evaluating pole and zero frequencies.

?
Error?

Appendix C shows plots of the four measured FRF-s compared with the transfer functions resulting from the 40th order MIMO model, figure 15 below shows the magnitude plot of the MIMO system.

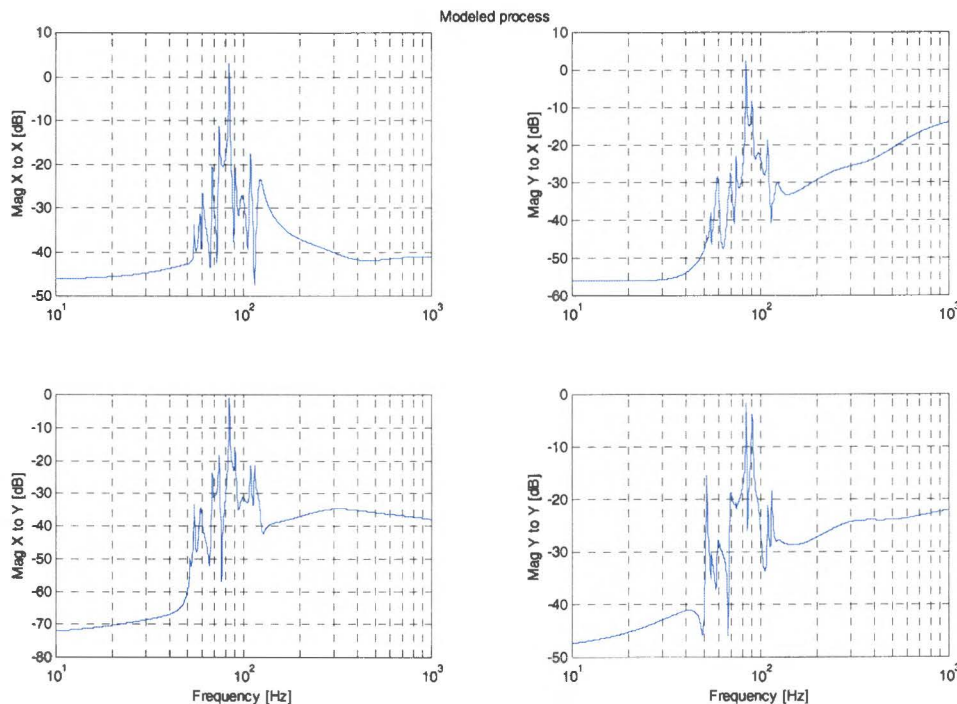


Figure 15: Modeled and reduced process magnitude plot

4.3 Performance restrictions

The process used in the control loop leads to some performance restrictions. With performance the degree of disturbance rejection is meant in this control problem, which can be measured by the sensitivity S . There are two main causes for these performance restrictions: process characteristics and process uncertainty.

4.3.1 Process characteristics

In e.g. [3] an enumeration is given of process characteristics that imply limitations on performance. Besides the Bode Sensitivity Integral, which always holds for existing processes, one mentioned characteristic is in order here: non-minimum phase zeros.

what?
not

The Bode Sensitivity Integral states that if the pole zero excess of the combination of the plant and controller is at least 2 and there are no RHP poles, the following holds:

$$\int_0^{\infty} \ln |S(j\omega)| d\omega = 0$$

Although the process model does not have a pole zero excess, this excess will certainly be present in the real process as well as in the controller process, because of limitations on physical realizable processes. The integral means that the area of $|S(j\omega)|$ under 0dB equals the area above it and thus that an inevitable trade-off exists between performance improvement in a certain frequency area and performance deterioration in another frequency area.

Non-minimum phase zeros are zeros located in the right half plane and are therefore also addressed as RHP zeros. Their presence in a system causes a net change in phase when evaluated for frequency inputs between zero and infinity. The phase decreases at the zero break point instead of exhibiting the usual phase increase that occurs for an LHP zero. In section 4.1.2 it was already remarked that a tremendous negative phase shift was present in the measured SISO transfer functions. This shows that there are a lot of non-minimum phase zeros present in the SISO transfer functions. These zeros are well known to appear in a flexible structure problem with non-collocated sensors and actuators [7], with which this control problem can be compared.

As the process was considered to be a MIMO system, the non-minimum phase zeros turn up as RHP transmission zeros in the MIMO model. In figure 16 the pole-zero plot of the modeled MIMO system is shown. The zeros in this plot are the transmission zeros of the system. Close inspection of this plot showed three (one pair can not be observed well in the figure) RHP transmission zero pairs. They have a natural frequency of respectively 479 , 674 and 715 rad/s, or 76 , 107 and 114 Hz. These zeros lie almost exactly in the frequency area identified in chapter 2 as the area of interest. In [7] it was also shown that model refinement by addition of higher order modes can cause the appearance of additional zeros in the right half plane. Because almost no attention was paid to the correctness of the model at higher frequencies than 110 Hz but the negative phase shift continues, it can be assumed that these additional zeros are present in the real process.

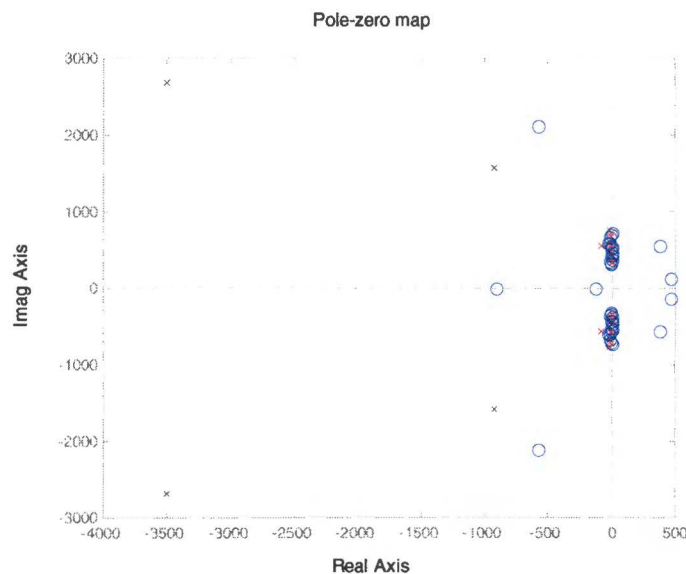


Figure 16: Pole-zero map of the MIMO modeled system

It is well known that RHP zeros of the process set very high limitations on the obtainable performance of the controlled loop. In [5] limitations imposed by RHP zeros of the open-loop

system are expressed directly in terms of the sensitivity function of the closed-loop system. The mentioned Bode Sensitivity Integral effect, the trade-off between performance in one frequency area against another, is boosted. It is said that a significant level of sensitivity reduction at frequencies near a right half plane zero, which is exactly what we need in this control problem, is necessarily accompanied by a large sensitivity increase at other neighbouring frequencies.

Thus, as a consequence of the characteristics of the process in the control loop, there will be a very strong trade-off between disturbance rejection at certain frequencies and disturbance amplification at other nearby frequencies.

4.3.2 Process uncertainty

Limitations on performance are also implied by process uncertainty. This because the control loop has to possess stability robustness as well as performance robustness. These two requirements can be translated in requiring a small complementary sensitivity T [3]. When there is a lot of uncertainty about the process, requirements on T will be very stringent. These requirements on T are reflected directly on S because of the rule $S(j\omega) + T(j\omega) = 1$. Thus, a high process uncertainty imposes strong limitations on performance.

In the case of the damping lenstop vibrations problem, process uncertainty is caused by measuring errors, modeling errors and process variation over time. The measuring errors will be ignored as it is expected that they can be neglected compared to the modeling errors. It is very difficult to quantify the process variation over time. Qualitatively it can be said that it was shown in [1] that control of flexible structures with non-collocated sensors and actuators is extremely sensitive to process changes, and therefore special care has to be given to robustness.

The model error can be quantified easily. Figure 17 shows the maximum singular value of the additive model error divided by the minimum singular value of the process in percent, in formula:

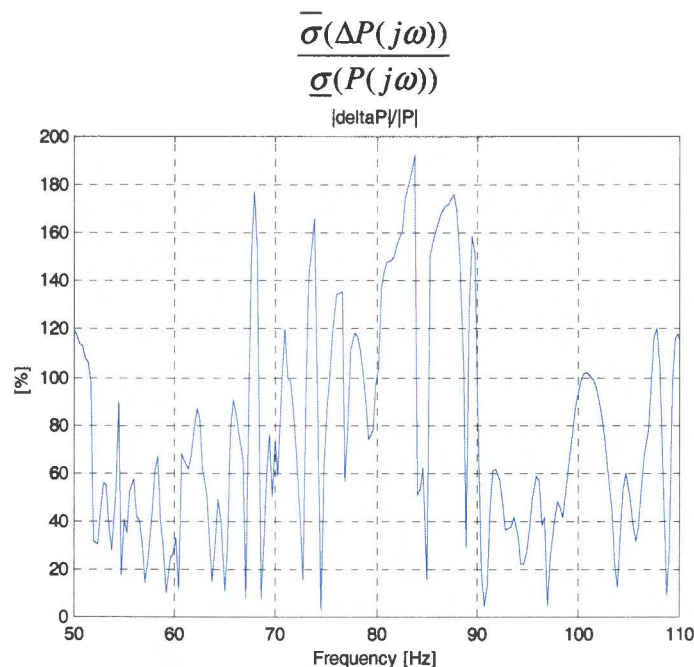


Figure 17: Maximum relative additive model error

In [3] it is stated that a 100% modeling error will certainly prevent disturbance rejection. It can be seen that for some frequencies in the frequency area of interest in the worst case the

modeling error is greater than 100 %, so the performance is more likely to become worse than better at those frequencies. This does not mean that control design is useless with this model, because the model error at the peaks of the process, which are the resonance frequencies that also are dominant in the disturbance, is much less than 100%. Still, it can be concluded that the model error limits the disturbance rejection considerably.

The modeling error contributes to the process uncertainty which becomes very high and there will necessarily be a strong trade-off between robustness and performance. This could be a reason for model improvement, however, because of the entanglement of the process, this is extremely difficult and will also provide a much higher order of the model.

5. Controller design

In this chapter the design of the controller that has to damp the lenstop vibrations is outlined. First is explained how it is evaluated if the designed controllers meet the requirements and how well they perform. After that three main control design methods will be tried out: simple proportional feedback, LQG control and H_∞ control, with different augmented plant setups. Not all design techniques will be treated equally extensively as it will quickly become clear that some techniques are not well suited for this problem. Finally all designed controllers will be compared and a choice will be made which designed controller will be implemented in the /800. This implementation is discussed in the next chapter.

5.1 Controller evaluation

The design methods that are used lead to controllers of which the performance has to be evaluated. First it has to be checked if the designed controller meets the requirements. When this is the case, the controller can be evaluated further to be able to compare its performance with the other designed controllers.

5.1.1 Simulations

Before outlining the requirements, first it is explained how the designed controllers could be simulated in Simulink of which results were used to judge if some requirements were met. The setup of the simulation can be seen in the lay-out of the Simulink model in figure 18. It can be seen that disturbance is inserted (lensacc, from workspace). This disturbance was extracted from tracefiles, in which measured undamped lenstop acceleration data was saved. Therefore the inserted disturbance represented real lenstop vibrations that had to be damped. There were 15 tracefiles available with data obtained from testrig/800, the same machine on which the transfer functions were measured.

The tracefiles were obtained during white noise injection on the airmount system in Rx and Ry direction with the existing PAS 5500 software. A very important remark is that tracefiles obtained during the run of a job were not available, and therefore no direct conclusions can be made about the improvement of performance during a job. The damped lenstop acceleration data is represented by c_lensacc in the Simulink model. Furthermore it can be seen that the actuation signal (actuation, to workspace) is also extracted.

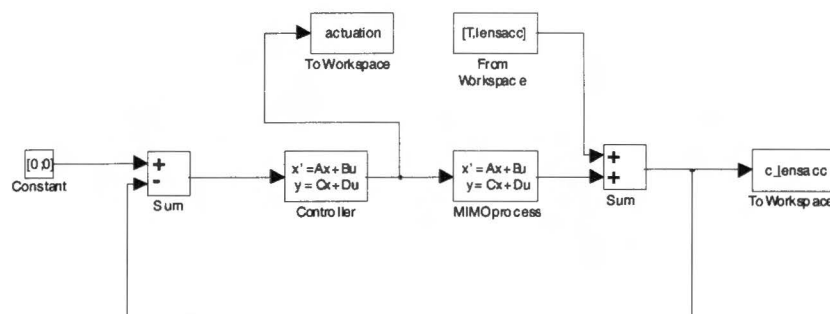


Figure 18: Simulink model setup

5.1.2 Controller requirements

Requirements that have to be met by the controller are:

- The control loop has to be stable, which is rather obvious.
- The controller should not be active in the frequency area below 5 Hz as was explained in paragraph 3.2.
- The resulting actuation signals can not exceed 1 V. This is an arbitrary but safe upper limit.
- The aim concerning performance was to damp the lenstop vibrations in the 50-110 Hz area as much as possible. It is not allowed to achieve this at the expense of high degradation of performance, thus strongly amplifying vibrations, outside this area. Designing a controller with such a performance goal will be called conservative design in the rest of this report.
- No explicit requirements are made on the avoidance of sensor noise. Figure 8 in chapter 3 showed that sensor noise certainly is present. However, in the targeted area, it is considerably smaller than the acceleration signal, except at the borders of this area. Taking the sensor noise into account would restrict the complementary sensitivity, which is already restricted indirectly by other requirements and performance aims.
- The controller has to provide an arbitrary amount of robust stability and performance robustness. At least the implementation of the controller can not lead to instability or high performance deterioration.

Strange!

There are several evaluation methods to check if a designed controller meets the requirements:

- Stability can be checked fastest by running a simulation.
- The simulation also provides actuation signal data. The amplitude of this signal can be checked to see if this does not exceed the upper limit. Furthermore a cumulative PSD plot of the actuation signal can be made to see if the actuation signal does not contain components below 5 Hz.
- The easiest way to see if the controller signal does not deteriorate the behavior outside the 50 – 110 Hz area too much is to look at cumulative PSD plots of closed loop lenstop acceleration data resulting from simulations.
- Nyquist plots can also be used to judge the stability of the control system. Because the system under research is a MIMO system, a kind of Nyquist plot can be obtained by plotting the eigenvalues of the looptransfer against frequency, the so-called characteristic loci [8]. Precise phase and gain margins can not be obtained from this plot, however it can be seen if a system is close to instability. A great advantage is that these Nyquist plots can also be constructed with the measured transfer functions. Although the plots are less clear because of less resolution, it can be evaluated if the closed-loop will also be stable with the real system. Consequently with the Nyquist plot something can be said about the robustness of the system.

5.1.3 Controller performance evaluation and comparison

When a designed controller meets the requirements its performance can be evaluated further and compared with other designed controllers by a few methods:

- An easy measure for comparison is the RMS performance improvement. This is calculated by dividing the RMS value of the undamped lenstop acceleration by the RMS value of the damped lenstop acceleration expressed in terms of percentage. The mentioned values are the mean of the values resulting from simulations with the mentioned 15 tracefiles.
- The PSD-s and / or cumulative PSD-s of closed loop lenstop acceleration data can be compared with the plots resulting from open-loop data to judge the behavior in the frequency domain.
- (Complementary) Sensitivity plots will also be used to judge the closed loop behavior in the frequency domain.

- The process sensitivity (P*S) can be used to see how the peaks in the transfer functions are suppressed. In this way, it can be seen at first glance, where the behavior of the system was improved by inserting the controller. The resonances in the system are mainly the same as the peaks in the disturbance, especially in the disturbance obtained by the artificially excited experiments, because this excitation was done with Lorenz motors of the AM system. Thus, when the peaks in the process sensitivity are decreased, the main frequency components of the disturbance will be suppressed.

5.2 Simple proportional design

In chapter 4 where the process was discussed, there were many indications that a sophisticated controller, rising from modern control methods, is needed for the damping of lenstop vibrations problem. Still, it is wise to also try out a classical design method for performance comparison and to see if the extra effort and the high order controller which will certainly arise from modern control methods, is really necessary. Therefore a simple proportional design was tested for the damping of lenstop vibrations problem. Because this method is SISO, which is a disadvantage, one controller was designed for the X direction and one for the Y direction. No uncoupling matrices were used, in paragraph 4.2.1 it was already shown that this would be no use. All figures used for evaluation of the designed controllers can be found in appendix D.

Figure D.1 and D.2 show the two SISO Nyquist plots of the open loop when the controller is only a gain. To obtain a SISO gain margin of 6 dB, this gain was 1.83 for X actuation to X acceleration and 4.26 for Y actuation to Y acceleration. Simulation with the MIMO system showed that the controller stayed stable. Simulation results are not shown, it is sufficient to mention that the improvement in RMS-values obtained with these controllers was less than 3 percent in both directions, without much disparity in performance between certain frequency areas.

It was decided to improve these controllers with low-pass filters at the proper frequencies, to obtain a more favorable phase at resonance frequencies (especially 84 Hz). After tuning the final controllers were:

$$C_{xx}(s) = K_{xx} \cdot \frac{2 \cdot \pi \cdot f_{xx}}{s^2 + 4 \cdot \pi \cdot d_{xx} \cdot f_{xx} \cdot s + (2 \cdot \pi \cdot f_{xx})^2} \cdot \frac{2 \cdot \pi \cdot f_l}{s + 2 \cdot \pi \cdot f_l}$$

$$C_{yy}(s) = K_{yy} \cdot \frac{2 \cdot \pi \cdot f_{yy}}{s^2 + 4 \cdot \pi \cdot d_{yy} \cdot f_{yy} \cdot s + (2 \cdot \pi \cdot f_{yy})^2} \cdot \frac{2 \cdot \pi \cdot f_l}{s + 2 \cdot \pi \cdot f_l}$$

$$\begin{aligned} K_{xx} &= -15.1 & d_{xx} &= 0.30 \\ K_{yy} &= -17.4 & d_{yy} &= 0.60 \\ f_{xx} &= 30 & f_l &= 75 \\ f_{yy} &= 40 & & \end{aligned}$$

The controllers are plotted in figure D.3 and figure D.4 and the obtained SISO Nyquist diagrams in figure D.5 and D.6. The MIMO Nyquist plot can be found in figure D.7. It shows that using the SISO controllers in the MIMO system does not lead to instability, and that a reasonable margin from instability is kept. Still, evaluation on the measured system in figure D.8. shows that the closed loop almost becomes unstable, the design does not hold much robustness.

The obtained system was simulated. First simulations took place with controlling in one direction. It was noticed that the performance in the other direction also improved. This can be explained by the fact that a controller tries to damp a certain movement in one direction. However, this same movement also causes lenstop acceleration in the other direction. Consequently, when this movement is damped, the lenstop acceleration in the other direction becomes less, and therefore the performance somewhat better.

Secondly, both controllers were inserted in the system and again simulations took place. The actuation signal amplitude stayed below 0.05 V, and there was no action below 5 Hz. As expected, the performance improved compared with using a single SISO controller. Furthermore it was noticed, that there was a great difference in performance dependent on the tracefile that was used to insert disturbance. The mean improvement concerning RMS-values was 10% in X-direction and 6.3 % in Y-direction. But the performance improvement fluctuated between 0% and 25% in both directions. The fluctuation can be explained with the sensitivity plots in figure D.11. In the sensitivity plots it can be seen that there are a few deep narrow drops in the sensitivity. Therefore the performance is good at only a few frequencies. In the tracefiles the resonance frequencies that dominate the disturbance fluctuate. So, when a resonance that does not have a low sensitivity attached to it, dominates the disturbance, the performance will be less, than when e.g. the lens resonance frequency (84 Hz) dominates the disturbance. This effect is increased because of an unfavorable phase of some resonance frequencies.

The process sensitivities can be seen in figure D.9. These show that because of the low order of the controller (compared to that of the system) only a few resonances can be suppressed, the process sensitivity does not become 'flat'. Figure D.10 show the cumulative PSD-s resulting from a simulation. It can be seen that the performance outside the 50 – 110 Hz area is not deteriorated, but that the performance improvement inside this area is small.

It can be concluded that as expected simple proportional design is not well suited to design a controller for damping lenstop vibration. The performance of the system improves only slightly. More tuning and higher order control design will probably lead to some improvement of the performance, but this improvement will be marginal. The controller needed will be of a very high order and the problem is too complex to expect a fair result with classical design methods.

5.3 LQG design

The second method which is tried out for controller design is the modern control theory method LQG-design. The reader is supposed to be known with this method. If needed, information about LQG design can be found in [2]. However, some important aspects of the LQG design methods, concerning the use of the method for the problem of damping of lenstop vibrations will be pointed out here:

- The LQG-design method is, opposite to the proportional design of the last section, well capable to handle MIMO systems. This is a great advantage.
- The LQG-design method is state-space orientated. This is a disadvantage, because knowledge about the system, the disturbance and the performance requirements is available in the frequency domain. It is difficult to link states to the frequency domain information.
- The LQG-design method does not guarantee robustness (see e.g. [3]), which is a disadvantage because one of the requirements is to generate a robust design.

For the calculation of an LQG controller, there are four weighting matrices that need to be determined:

Q: weights of the importance of the states
 R: weights of the actuation
 Rv: weights of the disturbance on the states
 Rw: weights of the measurement noise

The matrices Q and Rv are the most difficult to determine. For example, the disturbance of the system is the measured open-loop lenstop acceleration. In the frequency domain it is perfectly known where the disturbance is large. But because the system was black-box-modeled, it is difficult to determine which state will be affected the most by this disturbance. It is possible to do this, but it would be rather laborious.

Many weight matrix combinations have been tried out. In almost all situations the proportion of Q to R and of Rv to Rw was taken very high, to suppress actuation costs and neglect sensor noise. R and Rw were taken as the identity matrix all the time (except for a multiplication factor), because there was no difference between the actuation costs in X and Y direction and the sensor noise in X and Y direction. Options for Q were e.g. (squared) Hankel singular values (see below), $C^T C$, unity matrix). R could be taken as e.g. the unity matrix or $(I^*)BB^T$.

The best result was obtained by taking Q as the squared Hankel Singular Values (HSV, see paragraph 4.2.2) and R as the unity matrix. Using the HSV-s is a practical way to assign weights to the states of the matrix Q. The lenstop acceleration is particularly a result of the same resonances that are present in the system. The states belonging to those resonances have high HSV-s. As a consequence it is possible to use these HSV-s in the weighting matrix Q. In this way, we should suppress important resonances in the system.

The controller that met the requirements and had the best performance was calculated with the following weighting matrices (the size has been put in brackets, and is a consequence of the order of the modeled system, 40, and the number of in- and outputs, 2):

Q [40x40]: squared HSV-s on the diagonal axis, multiplied with a factor $1e27$.
 R [2x2]: Identity matrix.
 Rv [40x40]: Identity matrix, multiplied with a factor $1e4$.
 Rw [2x2]: Identity matrix, multiplied with a factor $1e-4$.

The squared HSV-s lay between $2.6e-21$ and $3.2e-17$, so indeed we did not restrict the actuation signal.

The figures following from this controller can be found in appendix E. The controller (figure E.1), the sensitivity (figure E.2), the complementary sensitivity (figure E.3), the process sensitivity (figure E.4), the Nyquist plot of the modeled MIMO system (figure E.5), the Nyquist plot of the measured system (figure E.6) and a cumulative PSD-plot of lenstop acceleration resulting from a simulation (figure E.7). The simulation showed that the actuation signal did not exceed 0.02 V and was not active below 5 Hz.

The following conclusions about the designed LQG controller can be made:

- The performance concerning RMS-values of the lenstop acceleration is a mean improvement 8.8 % and 11.8 % for x and y directions respectively. Fluctuation was high in this case also, between -3.8 % and 34 %.

- The trade-off between overall performance and the performance in the 50-110 Hz area could be steered up to certain extent. Some designed controllers performed slightly better in that area, while the overall performance degraded quickly.
- The sensitivity plots show the inevitable trade-off between performance improvement at some frequencies and performance deterioration at other frequency areas.
- The process sensitivity also shows that the performance at certain resonance frequencies is improved, but others are worsened. Here the mentioned disadvantage of LQG design was a burden. When a certain frequency does not have a state with a high HSV attached to it, the performance at that frequency will be bad, also when there is a lot of disturbance present at that frequency. Without the linking of the states to frequencies, it is not possible to penalize such deterioration of the performance. This effect is not well visible with this designed controller, because of the conservative design, but it was the limiting factor during designing. Besides worse performance outside 50-110 Hz there were also some frequencies inside this area that deteriorated the performance quickly.
- The MIMO Nyquist plot shows that the modeled closed loop system is nominally stable, which is an automatic outcome of LQG design. It seems that there also is an acceptable stability margin present, presumably as a result of the conservative design. The Nyquist plot of the measured system with this controller also shows a stable system. Less conservative designs lead to Nyquist plots that were close to being unstable, and seemed unstable when they were evaluated with the measured system.

It can be concluded that LQG design is not well suited for this problem of damping of lenstop accelerations. Only one controller has been evaluated here, but this one was regarded as the one with the performance that best met the requirements. Still, the performance of this 40th order controller was not appreciably better than the designed proportional controllers. It is expected that the performance can be improved by the mentioned linking of the states to frequencies, but it makes more sense to switch to another design method, the H_∞ control design method.

5.4 H_∞ design

The third design method that has been tried out to develop a controller for damping of lenstop vibrations is the H_∞ control design method. Again it is not the purpose of this report to give an explanation about this method. Information about H_∞ can be found in [3]. However, some important aspects of the H_∞ design method, concerning the use of the method for the problem of damping lenstop acceleration are pointed out here:

- The H_∞ design method is well capable to handle MIMO systems.
- The H_∞ design method is frequency orientated. As has been pointed out in the previous section, this is a great advantage, because all the needed information is available in the frequency domain.
- The H_∞ design method can guarantee robustness.

The critical part of H_∞ design is to determine the augmented plant. First it has to be chosen which weighting filters have to be taken into account. Second, these filters have to be determined. After choosing initial filters some tuning is needed to obtain the preferable performance.

For the choice which weighting filters will be used two aspects will be taken into account:

- Performance
- Model uncertainty

Sensor noise is neglected again and no direct penalty will be put on actuation. Furthermore there is no reference signal present, there is only disturbance that has to be damped.

There are three augmented plant setups, resulting from three different control structures, i.e. three different weighting filter combinations, that will be discussed. The standard control system set-up can be seen in figure 19. In this figure P denotes the physical standard plant, G is the generalized standard plant including the weighting filters V and W to specify performance, and M is the augmented plant, the weighted closed-loop system. Each different augmented plant setup results in a different minimizing problem and it will be shown that this will have a major impact on controller performance.

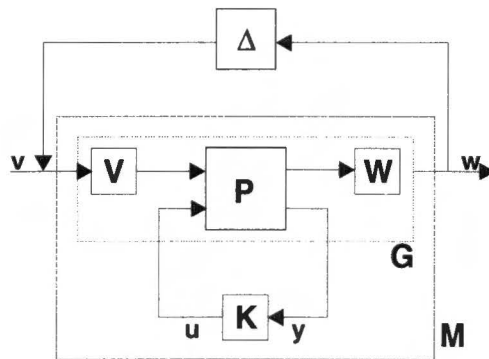


Figure 19: Standard control system setup

The weighting filters normally exist out of two parts: a scaling filter and a weighting filter for loopshaping. Different scaling for the inputs and outputs can be omitted. This is a consequence of the mutual similarity of the actuators and sensors. Furthermore, the mutual similarity of the sensors and actuators together with equal performance demands for the X and Y direction of the controlled system, result in the use of diagonal weighting filters. So, with every mentioned filter, a [2,2] transfer function matrix is meant, with the filter on the (1,1) and (2,2) position (the other elements of the matrix are zero), unless stated otherwise. Another remark is that phase data of filters will not be plotted, because the H_∞ method is phase irrelative. *True?*

5.4.1 Augmented plant setup 1

In [3] it is explained that it is wise to keep the composed matrix, resulting from the augmented plant, as small as possible. Therefore it is advised to use a filter W_u on the actuation signal to account for model uncertainty. This is very well possible here, because we do not use the filter for restricting actuation. In combination with a disturbance input filter V_d we now can model the model uncertainty ΔP . The control structure with the weighting filters can be seen in figure 20.

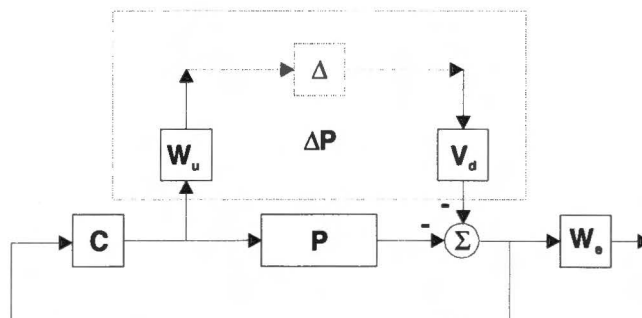


Figure 20: H_∞ control structure setup 1

The filter W_e is the filter that penalizes the output signal and thus specifies performance requirements.

With the setup of the augmented plant from figure 20 the H_∞ design control method results in the so-called mixed sensitivity problem, the design of a controller that minimizes:

$$\|M\|_\infty = \left\| \begin{pmatrix} W_e S V_d \\ W_u R V_d \end{pmatrix} \right\|_\infty$$

It holds that:

$$W_{et} \cdot S \cdot V_{dt} = \begin{bmatrix} W_e & 0 \\ 0 & W_e \end{bmatrix} \cdot \begin{bmatrix} S_{11} & S_{12} \\ S_{21} & S_{22} \end{bmatrix} \cdot \begin{bmatrix} V_d & 0 \\ 0 & V_d \end{bmatrix} \Rightarrow$$

$$\bar{\sigma}(W_{et} \cdot S \cdot V_{dt}) < \gamma \Leftrightarrow |W_e| \cdot \bar{\sigma}(S) \cdot |V_d| < \gamma \Leftrightarrow \bar{\sigma}(S) < \frac{\gamma}{|W_e V_d|}$$

equivalently:

$$\left. \begin{aligned} \bar{\sigma}(W_{ut} \cdot R \cdot V_{dt}) < \gamma \Leftrightarrow |W_u| \cdot \bar{\sigma}(R) \cdot |V_d| < \gamma \Leftrightarrow |W_u| \cdot \bar{\sigma}(P^{-1}T) \cdot |V_d| < \gamma \\ \bar{\sigma}(P^{-1}T) \geq \underline{\sigma}(P^{-1}) \cdot \bar{\sigma}(T) \end{aligned} \right\} \Rightarrow$$

$$|W_u| \cdot \underline{\sigma}(P^{-1}) \cdot \bar{\sigma}(T) \cdot |V_d| < \gamma \Leftrightarrow \bar{\sigma}(T) < \frac{\gamma}{|W_u V_d| \cdot \underline{\sigma}(P^{-1})} \Leftrightarrow \bar{\sigma}(T) < \frac{\gamma \cdot \bar{\sigma}(P)}{|W_u V_d|}$$

During the design we aim for $\|M\|_\infty < \gamma \approx 1$, consequently in the mixed sensitivity problem this leads to the restrictions:

$$\forall \omega : \bar{\sigma}(S) < \frac{1}{|W_e V_d|}$$

$$\forall \omega : \bar{\sigma}(T) < \frac{\bar{\sigma}(P)}{|W_u V_d|}$$

These restrictions can easily be plotted and bottlenecks can easily be recognized, which helps with the choice of weighting filters.

Model uncertainty

Model uncertainty can best be modeled as additive model uncertainty when using the control structure of figure 20. In [3] is proven that in this case as a result of the small gain theorem robust stability is guaranteed if:

$$\|M\|_\infty < \gamma \approx 1 \text{ and } \forall \omega : \bar{\sigma}(\Delta P) < |W_u V_p|$$

ΔP represents the additive model error. In this case the filter V_d represents V_p .

It is a great problem to guarantee robustness for the problem of damping lenstop acceleration. Already in section 4.3.2 was stated that there would be a harsh trade-off between robustness and performance. Figure 21 shows the maximum singular values of the additive model error. This was obtained by subtracting the modeled frequency response functions from the measured frequency response functions. Figure 21 also shows a possible combination $|W_u V_d|$ where applies:

$$\forall \omega : \bar{\sigma}(\Delta P) < |W_u V_p|$$

To guarantee robust stability, the goal was $\|M\|_\infty < \gamma \approx 1$, which was shown to imply:

$$\forall \omega : \bar{\sigma}(T) < \frac{\bar{\sigma}(P)}{|W_u V_d|}$$

Figure 22 shows the border for the maximum singular value of T when $|W_u V_d|$ is chosen as drawn in figure 21. It can be seen that the border in the bode magnitude plot for this value T is very low, so T has to have a very small value at all frequencies to guarantee robust stability. Because of the rule $S+T=I$, S will be around I, which means that a controller designed in this way will lead to near zero performance improvement. The design and simulation of a controller with the mentioned weighting filters W_u and V_d confirmed this.

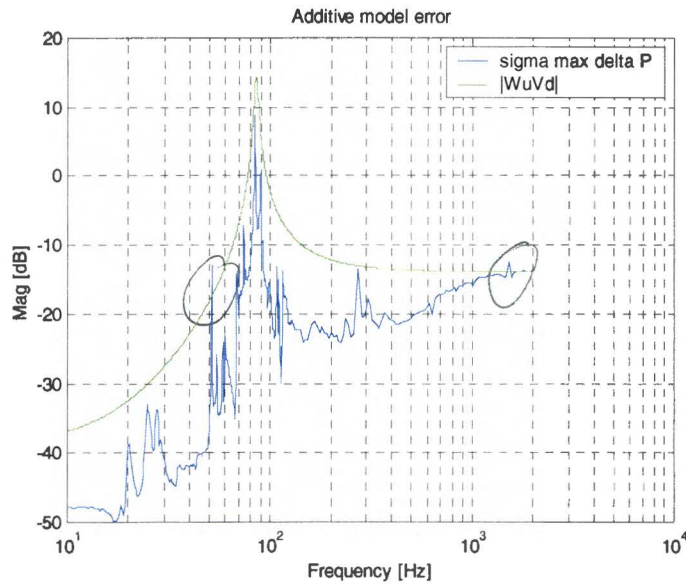


Figure 21: Additive model error

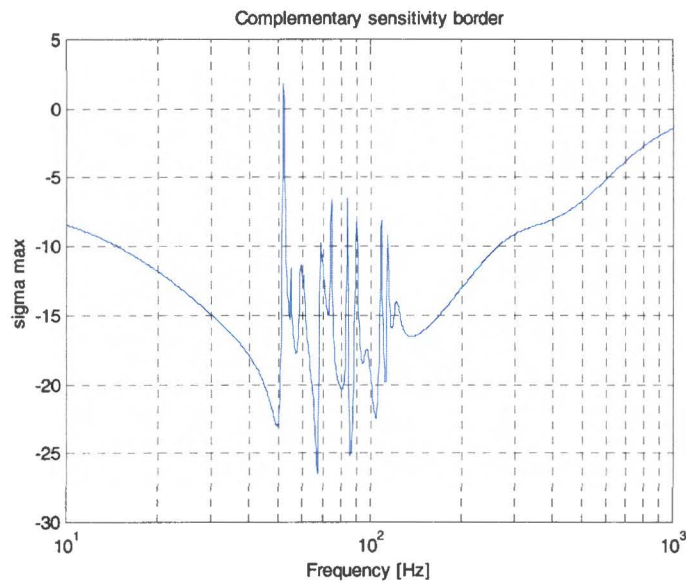


Figure 22: T border when guaranteeing robustness

As a consequence of the mentioned problem, we have to leave out the guarantee for robust performance. This does not have to be disastrous, because the restriction that the H_∞ method lays on the controller design to guarantee robustness often is far more stringent than needed. Therefore the only restriction left will be the performance of the designed controller. We will use the filter W_u to restrict R , but far above the robustness requirement.

Plots of used filters and results with the augmented plant setup 1 can be found in appendix F.

Loopshaping: $V_d = 1$

The first tuned H_∞ controller was developed with the disturbance taken as white noise, $V_d = 1$. The filters W_e and W_u are plotted in figure F.1 and the transfer functions are:

$$W_e = 2.9 \cdot 10^{-4} \cdot \left(\frac{(s + 2 \cdot \pi \cdot f_{e1})^2 \cdot (s + 2 \cdot \pi \cdot f_{e2})^2}{(s + 2 \cdot \pi \cdot f_{e3})^2 \cdot (s + 2 \cdot \pi \cdot f_{e4})^2} \right)$$

$$W_u = 0.23 \cdot \left(\frac{(s + 2 \cdot \pi \cdot f_{u1})^2}{(s + 2 \cdot \pi \cdot f_{u3})^2} \right)$$

$$f_{e1} = 1\text{Hz}, f_{e2} = 1 \cdot 10^4 \text{Hz}, f_{e3} = 50\text{Hz}, f_{e4} = 110\text{Hz}$$

$$f_{u1} = 30\text{Hz}, f_{u2} = 300\text{Hz}$$

W_u was chosen to follow the shape of the model uncertainty in the frequency domain, except for the peak. W_e was chosen to emphasize the performance requirement in the area 50-110 Hz. The restrictions imposed on S and T by these filters can be seen in figure F.2. Figure F.3 shows the controller that emerged from this design. The achieved γ -value was 1.11. It can be seen that the controller actions are quite low. The sensitivity plot, figure F.4 shows that the controller indeed emphasizes to improve the performance in the area 50-110 Hz. However, because the disturbance input filter V_d was taken as white noise, there is no extra emphasis in suppressing certain resonance frequencies. So, the controller wants to improve the performance over a wide area and because of the explained strong trade-off between performance improvement and deterioration, the obtained performance improvement is very minimal. Furthermore the required sensitivity decrease at the non-minimum phase zero locations can not be complied with.

This controller was the best controller obtained with the filter $V_d = 1$. It will not be analyzed further, because of its very minimal performance (9% respectively 8% RMS improvement for X and Y), which also can be seen in the cumulative PSD plot resulting from a simulation in figure F.5. It is clear that the neglect of available information, i.e. the disturbance shape, restricts the controller too much and this information has to be taken into account.

Anyway, also with this filter shape choice, a trade-off between the performance inside and outside the 50-110 Hz area was possible, again a conservative approach was taken. Furthermore, the performance improvement fluctuates little over the tracefiles, because of the lack of sharp peaks and narrow drops in the sensitivity.

Loopshaping: V_d shaped according to disturbance PSD-s

The best way to precisely model the disturbance with a filter, is to fit a filter exactly over the PSD of the measured disturbance data. First phase data has to be generated, because only magnitude data are available in a PSD function. Phase data can be generated with e.g. the function `genphase` of the Matlab μ -toolbox. Next, a fit can be made with e.g. the function

invfreqs of the Matlab signal processing toolbox (also used for fitting of the transfer functions of the process).

An important remark at this point is that H^∞ design (before possible order reduction) leads to a controller that is of the order of the process (40 in this case) plus the order of all the filters. Consequently, a higher order fit on the disturbance PSD-s, will lead to a higher order controller. This is a reason to confine the fit to a few orders. Furthermore this filter will not be diagonal, because the disturbance PSD in x-direction differs from the disturbance PSD in y direction. Fits can be seen in figure F.6, V_{dx} was 6th order and V_{dy} was 12th order.

There was no success in designing a usable controller in this way. γ -values exceeded 100, almost all the time, also with the most conservative controller design, i.e. very low performance weights. The reason for this appears to be numerical. When the 6th order V_{dx} and the 12th order V_{dy} filter are used, the function hinfsyn is not capable of calculating controllers with a γ -value below 1000, regardless of the W_e and W_u filters, even when the restrictions on performance are very low. Decreasing of W_e and W_u does not reduce the obtained γ -value. When the order of the V_d filters is reduced, the γ -value that can be obtained does decrease. However, keeping V_d of the order that is needed to approximate the disturbance-PSD-s very roughly, did never lead to a γ -value near 1 and a well performing controller. Therefore the disturbance information has to be taken into account in another way.

5.4.2 Augmented plant setup 2

There is a way to prevent the use of high order filters and still take some information about the disturbance into account. This can be done by composing the augmented plant as depicted in figure 23. It can be seen that the V_d filter is left out and that an actuation input filter V_u has come in its place. The augmented plant now can be compared with the plant that is depicted in figure 24.

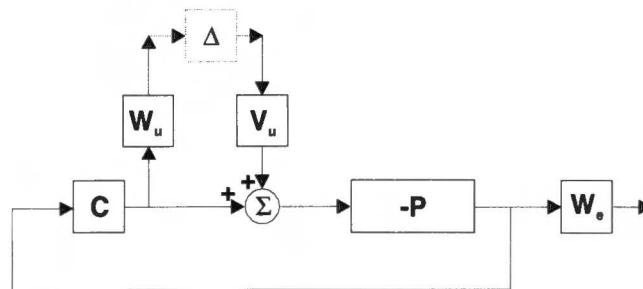


Figure 23: H^∞ control structure setup 2

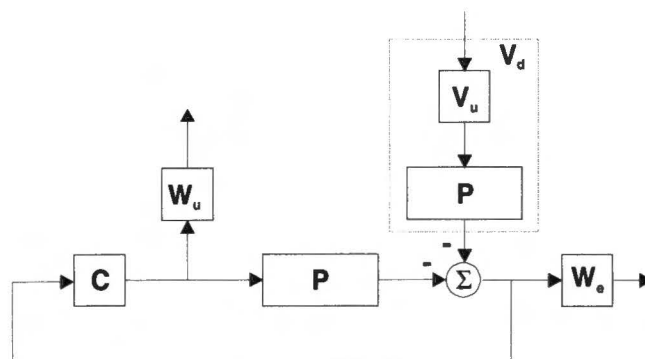


Figure 24: Redrawn H^∞ control structure

When the filter V_u is taken as a constant value, the disturbance is shaped with the great difference that we do not need a high order filter for this. The disadvantage of the new configuration is that although the disturbance has much resemblance with the process, it is not the same. Therefore we do not model the disturbance exactly and this approach will especially optimize the decrease of the process sensitivity $P \cdot S$.

The H_∞ optimization problem again becomes a kind of mixed sensitivity problem and will minimize:

$$\|M\|_\infty = \left\| \begin{pmatrix} W_e P \cdot S V_u \\ W_u T V_u \end{pmatrix} \right\|_\infty$$

The V_u filter will be taken simply I. Design restrictions will only be applied with the other two filters, W_u and W_e . Restrictions on T and S can be deducted equivalently to the deduction of the restrictions at the previous augmented plant setup and when we again aim at $\|M\|_\infty < \gamma \approx 1$, they become:

$$\forall \omega : \bar{\sigma}(S) < \frac{1}{|W_e V_u| \underline{\sigma}(P)}$$

$$\forall \omega : \bar{\sigma}(T) < \frac{1}{|W_u V_u|}$$

Model uncertainty

W_u will be again be used to model the model uncertainty. But because of the different structure of the augmented plant, it needs to be reviewed how this has to be done. The modeling of the uncertainty can better be done with input multiplicative model uncertainty, depicted in figure 25.

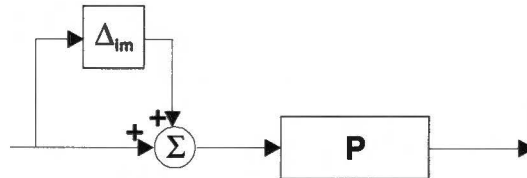


Figure 25: Input multiplicative uncertainty

As a result of the small gain theorem robust stability is assured when:

$$\forall \omega : \bar{\sigma}(T) \cdot \bar{\sigma}(\Delta_{im}) < 1 \Leftrightarrow \forall \omega : \bar{\sigma}(W_u T V_u \cdot \frac{1}{W_u V_u}) \cdot \bar{\sigma}(\Delta_{im}) < 1$$

And because:

$$\|M\|_\infty < \gamma \approx 1 \Rightarrow \|W_u T V_u\|_\infty < 1 \Leftrightarrow \forall \omega : \bar{\sigma}(W_u T V_u) < 1 \Rightarrow$$

$$\bar{\sigma}(W_u T V_u \cdot \frac{1}{W_u V_u}) \leq \bar{\sigma}(W_u T V_u) \cdot \frac{1}{|W_u V_u|} < \frac{1}{|W_u V_u|}$$

A sufficient condition for robust stability is:

$$\frac{1}{|W_u V_u|} \bar{\sigma}(\Delta_{im}) < 1 \Leftrightarrow \bar{\sigma}(\Delta_{im}) < |W_u V_u|$$

The weighting filters can be chosen so that $|W_u V_u|$ meets this condition. So, we can use W_u to model model uncertainty and guarantee robust stability, however again it will not be possible to reach this guarantee when also requiring performance.

Plots of used filters and results with the augmented plant setup 2 can be found in appendix G.

Loopshaping

This configuration of the augmented plant turned out to be very convenient to work with. The performance of the controllers designed in this way was often acceptable. A total trade-off was possible between the performance inside and outside the 50-110 Hz frequency area.

Figure 26 shows what is meant with this total trade-off. In this figure the cumulative PSD-s resulting from a simulation that was calculated to obtain a controller that performed very well in the area 50-110 Hz. It can be seen that this happens at the cost of frequencies outside this area.

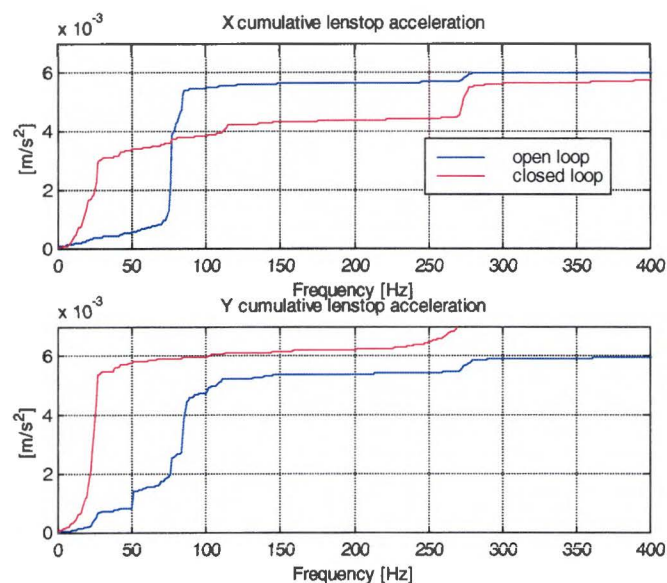


Figure 26: Total performance trade-off example

After tuning the controller that best met the performance requirements was obtained with the filters denoted below plotted in figure G.1.

$$W_e = 8.38 \cdot 10^{-8} \cdot \left(\frac{(s + 2 \cdot \pi \cdot f_{e1})^4}{(s + 2 \cdot \pi \cdot f_{e2})^2 \cdot (s + 2 \cdot \pi \cdot f_{e3})^2} \right)$$

$$W_u = 1000 \cdot \left(\frac{(s + 2 \cdot \pi \cdot f_{u1})^2 \cdot (s + 2 \cdot \pi \cdot f_{u2})^2}{(s + 2 \cdot \pi \cdot f_{u3})^2 \cdot (s + 2 \cdot \pi \cdot f_{u4})^2} \right)$$

$$f_{e1} = 1 \cdot 10^4 \text{ Hz}, f_{e2} = 20 \text{ Hz}, f_{e3} = 110 \text{ Hz}$$

$$f_{u1} = 50 \text{ Hz}, f_{u2} = 110 \text{ Hz}, f_{u3} = 1 \text{ Hz}, f_{u4} = 10000 \text{ Hz}$$

The mean performance improvement concerning RMS-values with this controller was 46 % in X direction and 24 % in Y-direction, which is rather well compared with previous designed controllers. Again it was not possible to guarantee the robust stability, the input multiplicative model uncertainty was calculated and plotted in figure G.2, with the modeled model uncertainty plotted in the same figure.

Loop shaping

Shaping and tuning of the filters until the optimal performance was reached, lead to the following filters:

$$Vd = 4.54 \cdot 10^{-2}$$

$$Vu = 1$$

$$We = 2.69 \cdot 10^{-3} \cdot \left(\frac{(s + 2 \cdot \pi \cdot f_{e1})^2 (s + 2 \cdot \pi \cdot f_{e2})^2}{(s + 2 \cdot \pi \cdot f_{e3})^2 \cdot (s + 2 \cdot \pi \cdot f_{e4})^2} \right)$$

$$Wu = 2250 \cdot \left(\frac{(s + 2 \cdot \pi \cdot f_{u1})^2 \cdot (s + 2 \cdot \pi \cdot f_{u2})^2}{(s + 2 \cdot \pi \cdot f_{u3})^2 \cdot (s + 2 \cdot \pi \cdot f_{u4})^2} \right)$$

$$f_{e1} = 1\text{Hz}, f_{e2} = 1 \cdot 10^4 \text{Hz}, f_{e3} = 50\text{Hz}, f_{e4} = 110\text{Hz}$$

$$f_{u1} = 60\text{Hz}, f_{u2} = 70\text{Hz}, f_{u3} = 1\text{Hz}, f_{u4} = 10000\text{Hz}$$

A plot of the filters W_e and W_u can be seen in figure H.1. Figure H.2 shows the weighting on S and T for the X to X and the Y to Y direction by respectively $|W_e P_i V_u|$ and $|W_u P_i^{-1} V_d|$ where for P_i the values of P_{11} respectively P_{22} were taken. In this way it is possible to see where extra performance improvement is requested for the X to X and Y to Y direction. Figure H.3 shows the restrictions that are made on S and T. It can be noticed that although we still require extra performance improvement at resonance frequencies, it is not allowed to comply with this request by too much performance deterioration at other frequencies.

The designed controller can be seen in figure H.4, the sensitivity in figure H.5, the complementary sensitivity in figure H.6 and the process sensitivity in figure H.7. The obtained γ -value was 0.98. The complementary sensitivity plot shows that the neglecting of the sensor noise did not lead to an unacceptable complementary sensitivity and therefore was allowed. The actuation signal does not exceed 0.2 V and does not have components below 5 Hz. The process sensitivity plot shows that indeed the controller emphasizes to suppress the resonance peaks.

Figure H.8 shows the MIMO Nyquist plot of the modeled open-loop, figure H.9 shows the Nyquist plot of the measured open-loop. It can be seen that the system indeed is stable. With this augmented plant setup, it was far more easy to trade off between robustness and performance.

Figure H.10 shows the cumulative PSD that results of a simulation with this controller. The mean performance improvement concerning RMS-values obtained with this controller were 32% in x-direction and 33% in y-direction.

5.4.4 H_2 design

A short note can be made on H_2 design. H_2 design is a design method that works in the same way as H_∞ design. The difference is that H_2 design tries to minimize $\|M\|_2$ instead of $\|M\|_\infty$. This means that H_2 design tries to minimize the energy induced by the augmented plant. Therefore, H_2 design can be seen as the equivalent of LQG design in the frequency domain. Consequently, with H_2 design the main disadvantage of LQG design for the damping of lenstop acceleration problem can be avoided.

The difference of LQG / H_2 with the H_∞ design method, is that it is much less easy to control $\overline{\sigma}(S(j\omega))$ and $\overline{\sigma}(T(j\omega))$ because all the principal gains are manipulated simultaneously over

the frequency domain. This is a significant difference and a disadvantage because we want to damp resonances which are sharp peaks in the frequency domain. Sharp peaks do not induce much energy, and therefore there is not much extra effort in suppressing these peaks.

H_2 design has been tried out with the augmented plant setups and weighting filters from the previous sections. Small adjustments were made because the H_2 design requires a strictly proper plant (otherwise the induced energy will be infinite). None of the controllers that emerged from the design will be treated, because the disadvantage mentioned in the previous paragraph was well observable and no controller with comparable performance to the H_∞ designed controllers could be obtained.

5.5 Designed controllers comparison

Table 7 shows an overview of all discussed controllers. In the table their performance is outlined, as well as their main disadvantage if any. It is rather obvious that the designed H_∞ controller with the augmented plant setup 3 is to be preferred above all others. This controller has the best performance while still obtaining some robustness. All other controllers damp the lenstop vibrations only marginal, except for the controller that arose from the H_∞ method with setup2. This controller was found out to be not robust and became unstable when evaluated in the real system.

Table 7: Controller comparison for nominal plant

Controller	Proportional	LQG	H_∞ setup1 Vd = 1	H_∞ setup1 Vd = fitted	H_∞ setup2	H_∞ setup3
RMS improvement X	10%	8.8%	9%	n / a	46% \rightarrow	32%
RMS improvement Y	6.3%	11.8%	8%	n / a	$\frac{24\%}{70}$	$\frac{33\%}{65}$
Main disadvantage	To low order for complex system and SISO	Hard to link frequency information to states	S is suppressed over wide area:	Numerical problems	Not robust because of pole/zero cancellations	-

The improvement obtained with the H_∞ controller with setup 3 is the maximum to obtain with the process in the control loop. Causes for this were denoted in paragraph 4.3.

6. Controller implementation

This chapter discusses the implementation of the best performing controller from the previous chapter. First the controller reduction is outlined briefly, after that the transformation to the z domain is treated. Finally implementation results are given.

6.1 Controller reduction

As mentioned before, the H_∞ control design method designs controllers that are of the order of the process together with the order of the filters. As a consequence the designed controller is of the order 56. It is possible to reduce this order with methods that were also used for reducing the order of the process model in section 4.2.2. An acceptable reduction to a 32 order controller could be obtained. Figure 28 shows the controller together with the reduced controller. Evaluation in a Nyquist plot of this controller with the measured system (not shown) revealed that the closed-loop did not come closer to instability by the reduction. The performance of the reduced controller improved slightly in X direction and degraded in Y direction, within acceptable margins.

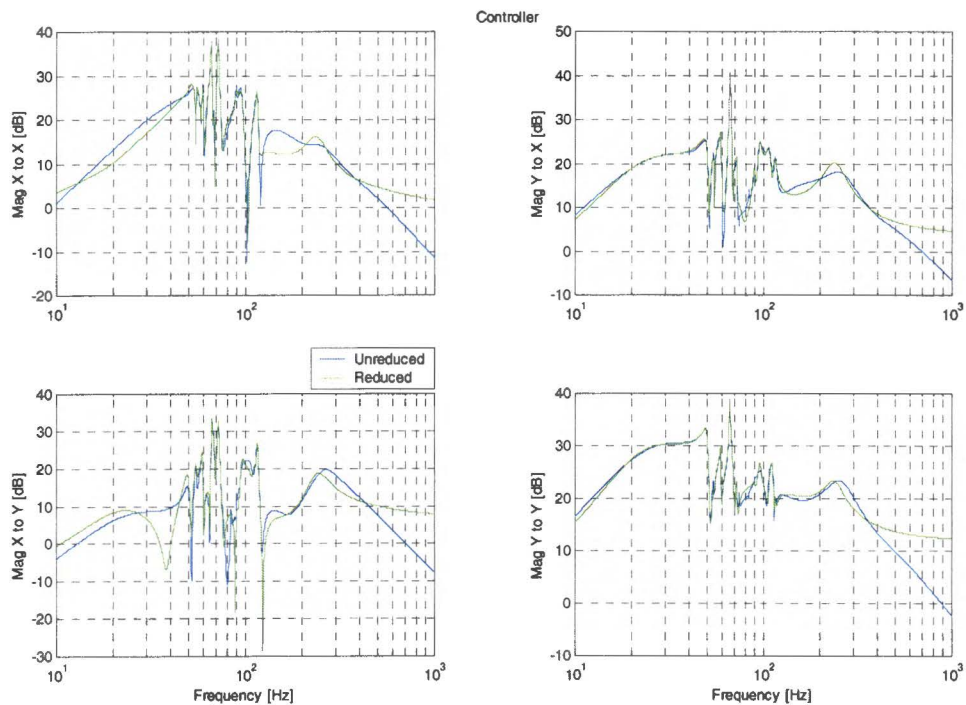


Figure 28: Controller reduction

6.2 Controller digitization

Implementation of the reduced controller had to be done with D-space, which requires that the continuous-time controller is converted to the discrete time domain. It was found out that the approximated maximum sample frequency with which the used D-Space system could work, with this high order controller, was 5 kHz. Figure 29 shows the pole-zero map of the reduced controller. The fastest pole is located at approximately 3476 rad/s = 553 Hz, so the digitization with 5 kHz should be possible.

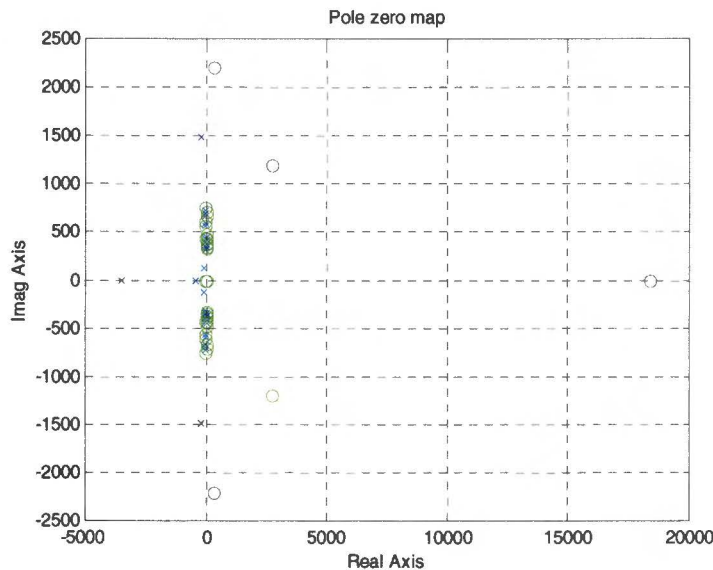


Figure 29: Pole-zero map of the reduced controller

It was found out that conversion to the discrete time domain at 5 kHz with the zero-order-hold (ZOH) approximation was less accurate than Tustin's method (both methods are described briefly in the next paragraph). With a previous designed controller, this inaccuracy of the ZOH method even led to an unstable closed-loop system.

Figure I.1 shows the magnitude plot of the continuous time controller and the digital controller, digitized with ZOH, figure I.2 shows the same plot when the controller is digitized with the Tustin approximation. It can be seen that Tustin's method approximates the controller better than the ZOH method, especially at high frequencies. With the mentioned previous designed controller, that did not perform satisfactorily, the difference was more clear. In that case the MIMO Nyquist plots showed that indeed the incorrectness of ZOH at high frequencies lead to an unstable controller.

Digitization by the ZOH method is done with Matlab as follows:

$$H(z) = \frac{z-1}{z} \cdot Z \left\{ \frac{1}{s} \cdot H(s) \right\}$$

Where Z denotes the z-transformation as described in e.g. [4].

Digitization by the Tustin method uses the approximation:

$$z = e^{sT_s} \approx \frac{1 + s \cdot \frac{T_s}{2}}{1 - s \cdot \frac{T_s}{2}}$$

T_s is the sample time. For Tustin's method it can be calculated how high the error in placing poles and zeros in the z-domain is as function of the frequency* T_s and the damping. This error is equal for zeros and poles. Tustin maps the complete imaginary axis of s-space onto the unit circle in the z-domain ($s=j\omega \rightarrow z=1$), while the ZOH-transform only maps the part till half the sampling frequency ($s=j\omega_s/2 \rightarrow z=1$). Consequently the Tustin transform performs better for higher frequencies and suffers less from aliasing. *?*

As a consequence, the controller digitized with Tustin's method was used for implementation in D-Space. Simulations showed that the digitization did not degraded performance at all, and also the MIMO Nyquist plot did not show any differences.

6.3 Implementation results

The digital controller was loaded in the D-Space system and connected in the loop as can best be grasped by figure 10 on page 11. The lenstop acceleration signals were fed into the D-Space A/D converters, while the actuation signal was taken from the D-Space D/A converters and fed into the airmount system. Open-loop and closed loop measurements of the lenstop acceleration signals have been performed again with noise on the airmounts in Rx and Ry direction. This time the resulting RS position errors were also measured. Furthermore it was possible to run a job on the testrig/800 and again trace the lenstop acceleration signals and RS position errors, open and closed loop. In all situations 15 tracefiles were obtained, and the discussed results are the mean over these tracefiles. Figures resulting from the measurements can be found in appendix I.

6.3.1 Results during airmount noise

The PSD plot of figure I.3 shows that the implemented controller indeed reduces the lenstop acceleration at certain frequencies. It can be seen that the lens resonance frequency, 84 Hz, dominates the PSD, and that the controller is very well able to reject this resonance at the lenstop. Although less visible, the figure also shows that resonances around this frequency are suppressed also.

The cumulative PSD plots (figure I.4) of the lenstop acceleration show a promising picture. Because the lenstop frequency is so dominating during noise on the airmounts and the controller suppresses this frequency well, the performance improvement is very well visible. Expressed in acceleration RMS values, also used during simulations to calculate improvement, the improvement was 35 % in X-direction and 60% in Y direction. For the X direction this matches almost exactly with the simulations. The improvement in Y direction is considerably higher than was simulated (33% improvement). Probable causes are the model and resulting simulation errors but also errors of statistical character. Measurement time was short and therefore not more than 15 tracefiles could be made in all situations, which is not enough to filter out statistical errors.

Time? X good? Y niet.

The RS position error that results from the lenstop accelerations were traced also. PSD and cumulative PSD plots can be seen in figure I.5 and figure I.6 respectively. The results shown in these plots are disappointing. The controller does not provide any observable performance improvement. Closer study learns that there are a few frequencies (e.g. lens frequency) that are damped, but performance is also deteriorated at other frequencies.

In section 2.2 the influence of the lenstop acceleration on the reticle stage position error was discussed. The RS position error could be derived from the measured lenstop acceleration and was confirmed with measurements. It could be seen that also during noise on the airmounts the influence of lenstop acceleration on RS position error was considerable. This derivation was deliberately done while omitting the present solution to suppress disturbance by lenstop acceleration, an extra feedforward from the accelerometers. This feedforward was also turned off during the position error measurements at that time, which was forgotten during controller implementation.

It is known that the feedforward operates well around a frequency of 90 Hz, which is close to the lens frequency. Therefore the influence of lenstop acceleration in this frequency area on the RS position error becomes much less, and suppressing the acceleration at especially the 84 Hz frequency does not lead to a smaller RS position error.

6.3.2 Results during the run of a job

It has been emphasized often that the excitation of resonances with airmount noise is different than the excitation during a job. The H_∞ controller was designed with an input filter on the actuation signal and simulated with lenstop acceleration data obtained during noise on the airmounts. In section 5.4.2 it was explained that this was convenient when working with noise, but that this did not give any guarantee of performance during a job, because of the possible different shape of the disturbance, the measured lenstop acceleration. In section 2.1 was shown that on proto1/500 the disturbance indeed was shaped different during a job and noise. However, the frequency peaks are a result of the same resonances, consequently they will be accounted for, only in a different proportion.

With the implemented controller open and closed loop measurements have been performed during a job. Figure I.7 and I.8 show the resulting PSD and cumulative PSD plots of the lenstop acceleration. The PSD plots have a low resolution because only data during a scan movement could be used. However, it can be seen that especially the resonance around the 70 Hz are excited. The lens is also excited. This is a pleasant finding, because the designed controller is well capable to damp these resonances. The cumulative PSD plots show that indeed a considerable improvement is obtained. In terms of RMS percentage the improvement in lenstop acceleration is no less than 100 % in X direction and 60% in Y direction.

In figure I.9 and figure I.10 the PSD and cumulative PSD of the resulting reticle stage position error can be seen. The problem of the previous section, the fact that the RS position error does not decrease, does not apply here. It is the 70 Hz frequency that dominates the acceleration and the level of acceleration is much higher than during excitation with noise. The feedforward does not operate well at 70 Hz and consequently the contribution of lenstop acceleration to RS position error is much higher during operation. The resonance peaks do stand out in the PSD plots and they are suppressed quite well. The cumulative PSD plot shows performance improvements in both directions. The RS position error during a job is reduced considerably, from 16 nm to 10 nm in X-direction. In Y direction the reduction is less, from 7.5 nm to 6 nm. The relative improvement goes up when one would only look at the area that was focussed on during control design, 50-110 Hz.

7. Conclusions and recommendations

This chapter concludes this thesis by presenting some conclusions about the design of the controller for lenstop vibration damping. Furthermore recommendations on the possible application of the controller and obtained knowledge is given.

7.1 Conclusions

It is possible to actively damp lenstop vibrations of an ASML wafer scanner with the use of the existing airmount system. This was proven on one scanner, testrig/800. Despite skepticism of this possibility that raised after measuring the transfer functions in order, a combination of several computational design techniques in different phases of the design process, lead to a controller that was able to damp the lenstop vibrations up to substantial extent.

The process from actuators to sensors in the control loop is so complicated that it is very hard to improve the obtained controller performance above marginal quantities with the same actuators and sensors. This applies for the scanner used in this research but is likely to apply to all scanners, because there is no indication that the process is less complicated at other scanners. Limiting factors that stood out during control design were model uncertainty and non-minimum phase zeros. The model uncertainty can be lowered by improving the model, however this will be very difficult and will lead to a higher order controller. There is no way of avoiding the non-minimum phase zeros with the present process.

Of the controller design methods that were tried out the H_∞ controller design method is the most appropriate method to use for the problem of damping lenstop vibrations. The process has multiple inputs and multiple outputs and is too complex to obtain considerable lenstop damping with a controller designed by a classical design method. The LQG control design method is very inconvenient to work with for this design task. The main burden is the discrepancy between the fact that all information is present in the frequency domain and the fact that LQG controller design requires information in the state-space domain. The H_∞ design method is powerful enough to calculate a high order multiple input multiple output controller that is necessary for actively damping of lenstop vibrations with the airmount system. Needed design information, e.g. performance requirements, can be provided in the frequency domain.

The best augmented plant used for the H_∞ controller design for lenstop vibration damping is the plant that has filters for performance and robustness requirements and two disturbance input filters, one located at the input and one at output of the process. The input filter on the input of the process is the most convenient way to stress additional effort at resonance frequencies. The input filter on the output of the process leads to the so-called four-block problem which prevents pole-zero cancellation that results from the mixed sensitivity problem. Consequently the mixed sensitivity problem lead to unrobust controllers, that became unstable in the closed-loop, while with the controllers resulting from the four block problem inherently some robustness was obtained. Still, the robustness could not be guaranteed because of the large model error.

7.2 Recommendations

This report can be seen as a feasibility study for active damping the lenstop vibrations with use of the airmount system as actuator and lenstop accelerometers as sensors. The previous section provided a positive answer to the question if this is possible. This does not imply that the designed controller should be implemented in all scanners right away. The pros and cons of implementation have to be weighed up against each other, which is beyond the competence of the author because of limited knowledge of the scanner and implementation consequences.

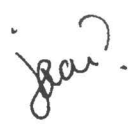
However, a few important remarks can be made:

- As was mentioned in the previous section and outlined in the report, robustness of the controller could not be guaranteed. This is a great disadvantage. Before a possible application it has to be researched if and when implementation on other scanners leads to an unstable closed loop. When small variances of resonance frequencies lead to instability, this can possibly be coped with by improving the design with the μ -analysis method.
- The controller was designed to damp vibrations at the top of the lens. It is unknown what the consequences are at other locations of the scanner. It is possible that the whole resonance vibration has been damped. But, it is also possible that the problem has been shifted and the resonance causes disturbance at another location. Thus, it has to be researched if this is the case.
- For each scanner type a different controller has to be designed because of different dynamic behavior. Because the testrig/800 is equipped with a dummy lens, the controller has to be redesigned for other /800 scanners. They will be equipped with a real lens and therefore posses other dynamic behavior also.
- The designed controller was implemented with a sample frequency of 5000 Hz. Motion controllers used in scanners work with a sample frequency of 2500 Hz. A quick check learned that it is probably very well possible to reduce the implementation sample frequency to this value. Consequently, when enough calculation capacity is present in the motion controllers, the controller to damp lenstop vibrations could be implemented in these systems.
- The possibility of damping the lenstop vibrations with the airmount system should be researched for the new Twinscan systems. Exactly the same design process based on H_{∞} design outlined in this report can be followed for this research. Because the Twinscan systems possess improved mechanical properties it may well be possible that the design is easier and the obtainable performance improvement is higher.
- There is something else that deserves some thoughts: This report showed that the airmount system is capable of damping of vibrations that are excited in the scanner. The sensors that were used were located far away from this actuation system. It is well known that non-collocated control of flexible structures faces severe robustness problems [1]. These problems were one of the limiting factors during this design. The location of the airmount system can not be changed. But when other sensors located closer to the airmount system could be used in the control loop, it may well become possible to obtain a much less complex transfer function. Consequently an easier design that leads to a better performing and more robust controller, may arise in this case. With better performing, performance improvement at the location of the new sensors is meant and not at the lenstop. At the lenstop the obtainable performance improvement will we less, because not all disturbance will be observed. But resonances are even more critical at other positions, closer to the airmount system. Locating the sensors near these positions makes it possible to damp the influence of the resonances at these position with the airmount system.

Perked Next?
Design → No
improvements

Q

Literature

- [1] Cannon R.H. and D.E.Rosenthal
Experiments in control of flexible structures with noncollocated sensors and actuators
J. of Guidance, Control and dynamics, Vol.7 (1984), p.546-553.
- [2] Damen A.A.H.
Modern control theory
Eindhoven, Eindhoven University of Technology, 1999, Dictaatnr. 5662
- [3] Damen A.A.H. and S.Weiland
Robust control
Eindhoven University of Technology, 1999
- [4] Franklin G.F., J.D.Powell and A.Emami-Naeini
Feedback control of dynamic systems
Reading: Addison-Wesley Publishing Company:1994
- [5] Freudenberg J.S. and D.P.Looze
Right half plane poles and zeros and design tradeoffs in feedback systems
IEEE Transactions on Automatic Control, Vol.30(1985),p.555-565.
- [6] Glad T. and L. Ljung
Control theory; multivariable and nonlinear methods
London: Taylor & Francis: 2000
- [7] Lindler D.K., K.M. Reichard and L.M. Tarkenton
Zeros of modals of flexible structures
IEEE Transactions on Automatic Control, Vol.38(1993),p.1384-1388.
- [8] Maciejowski J.M.
Multivariable feedback design
Workingham: Addison-Wesley Publishing Company:1989
- [9] Sefton J. and K.Glover
Pole/zero cancellations in the general H_∞ problem with reference to a two block design
Systems & Control letters, Vol.14(1990),p.295-306.
- [10] Skogestad S. and I.Postlethwaite
Multivariable feedback control
Chichester: John Wiley & Sons 
- [11] Smit S.G.
Pole-zero cancellations in the multivariable mixed sensitivity problem
N.V.Philips Gloeilampenfabrieken:1990, p.103-111.

Appendix A: Disturbance PSD-s

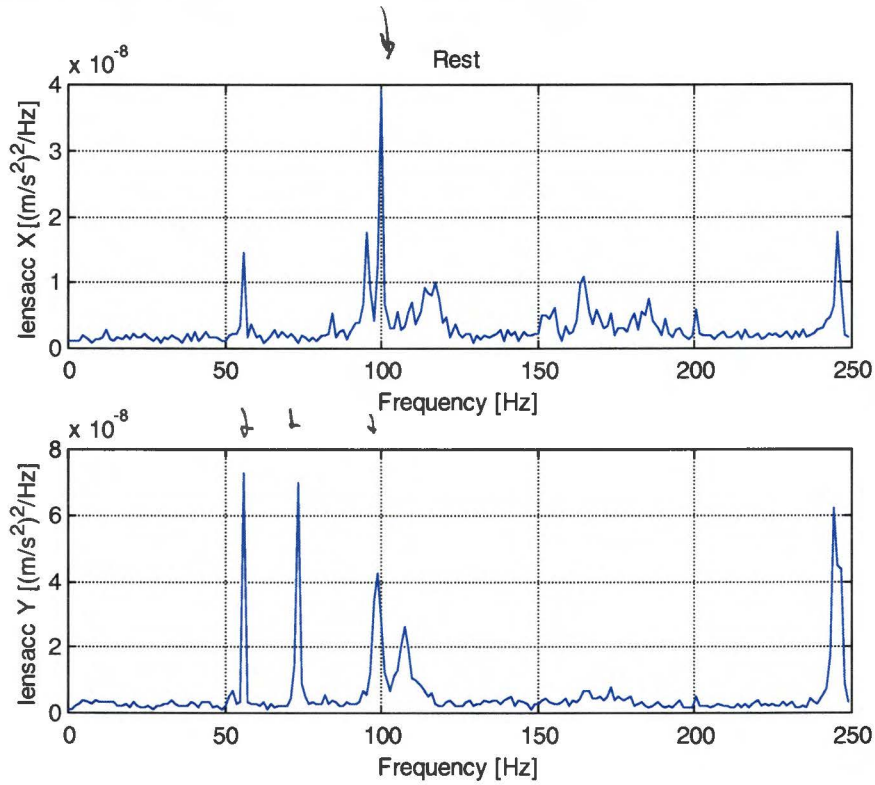


Figure A.1: Lenstop acceleration PSD during rest on /500

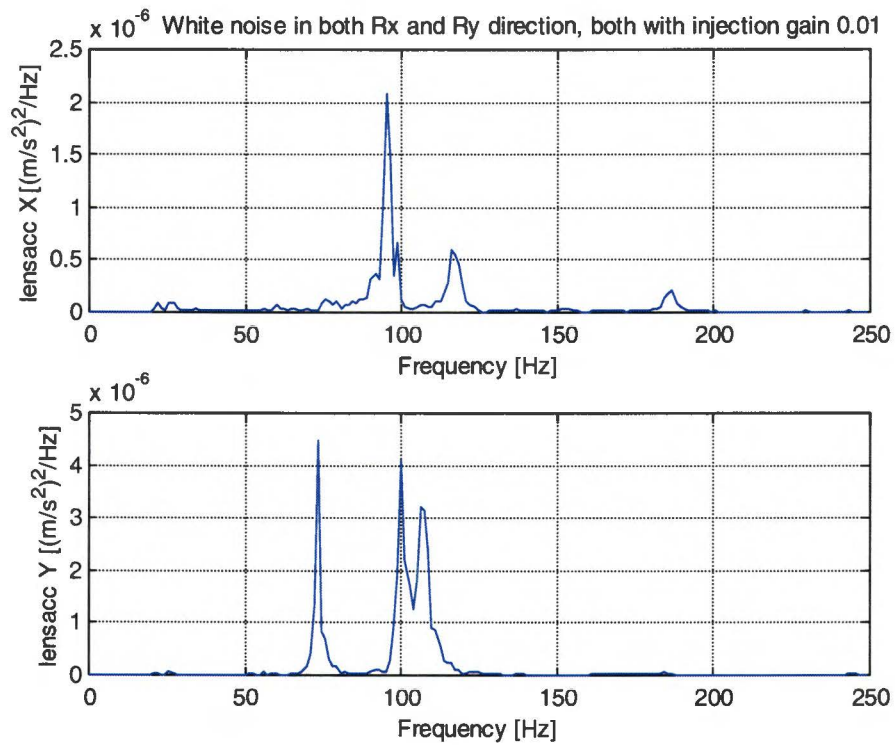


Figure A.2: Lenstop acceleration PSD during noise on AM-s on /500

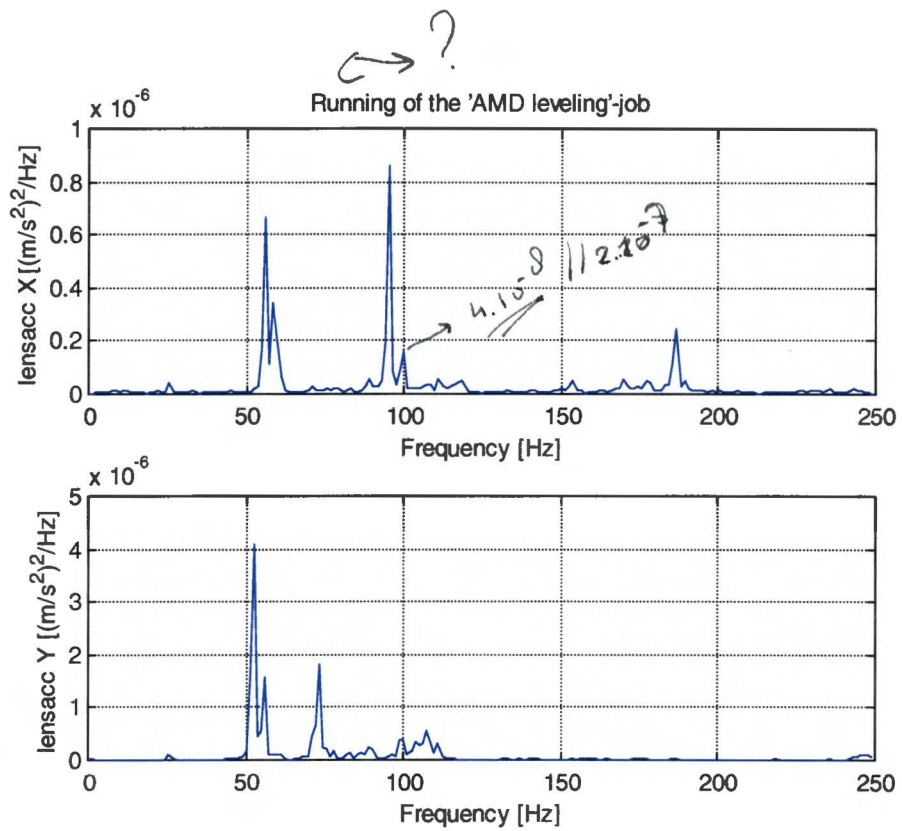


Figure A.3: Lenstop acceleration PSD during a job on /500

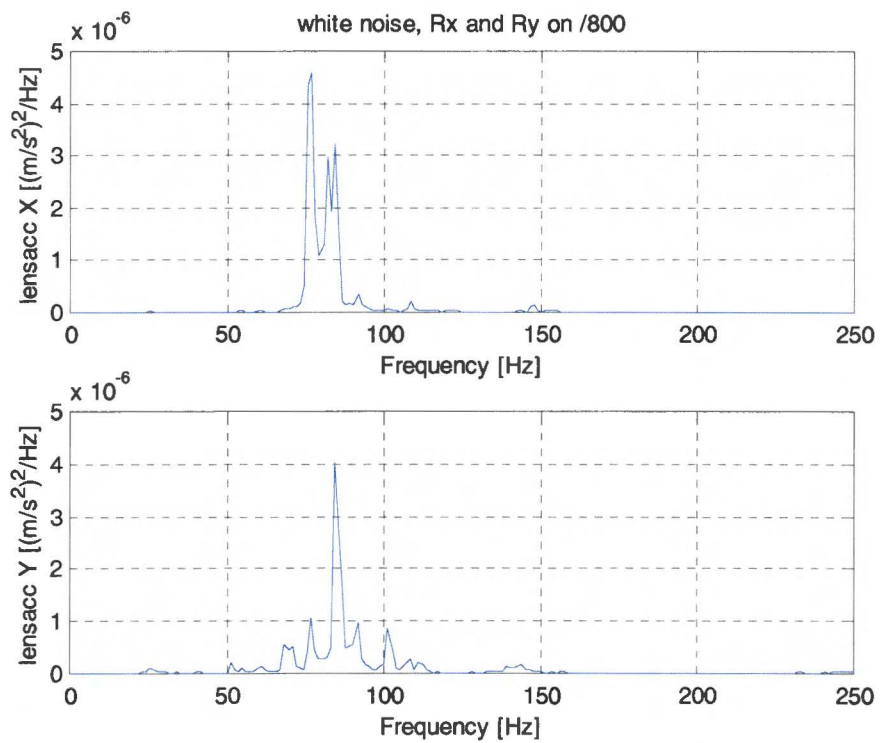


Figure A.4: Lenstop acceleration PSD during noise on AM-s on /800

Appendix B: Measured SISO FRF-s

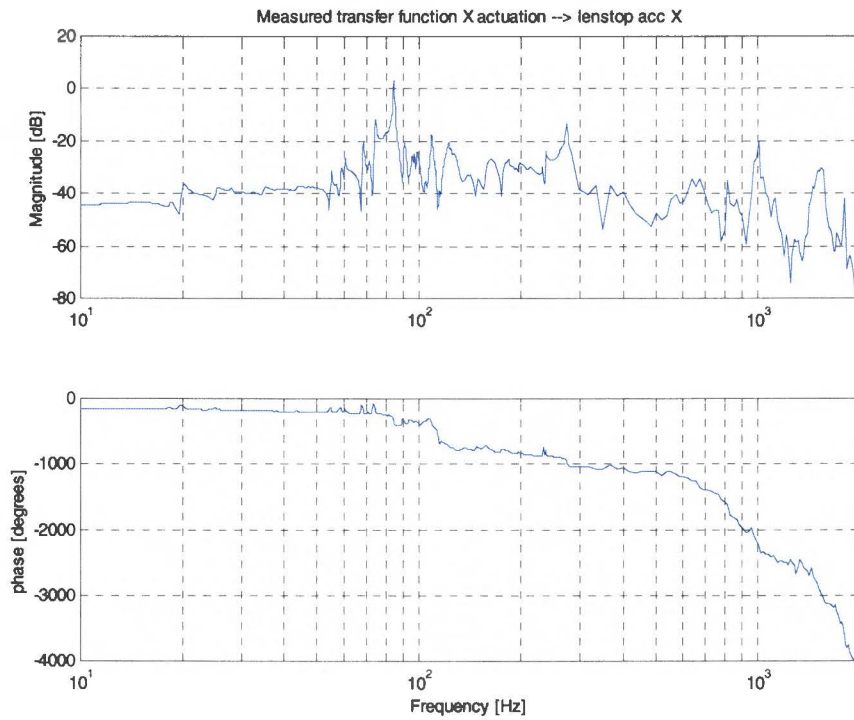


Figure B.1: Measured FRF X actuation [V] \rightarrow LA X [m/s^2]

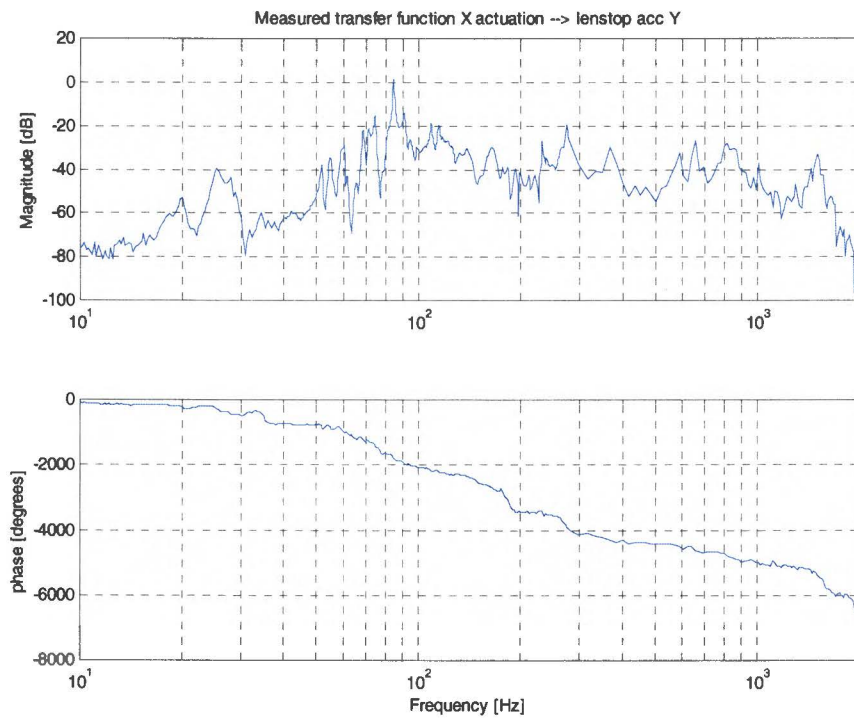


Figure B.2: Measured FRF X actuation [V] \rightarrow LA Y [m/s^2]

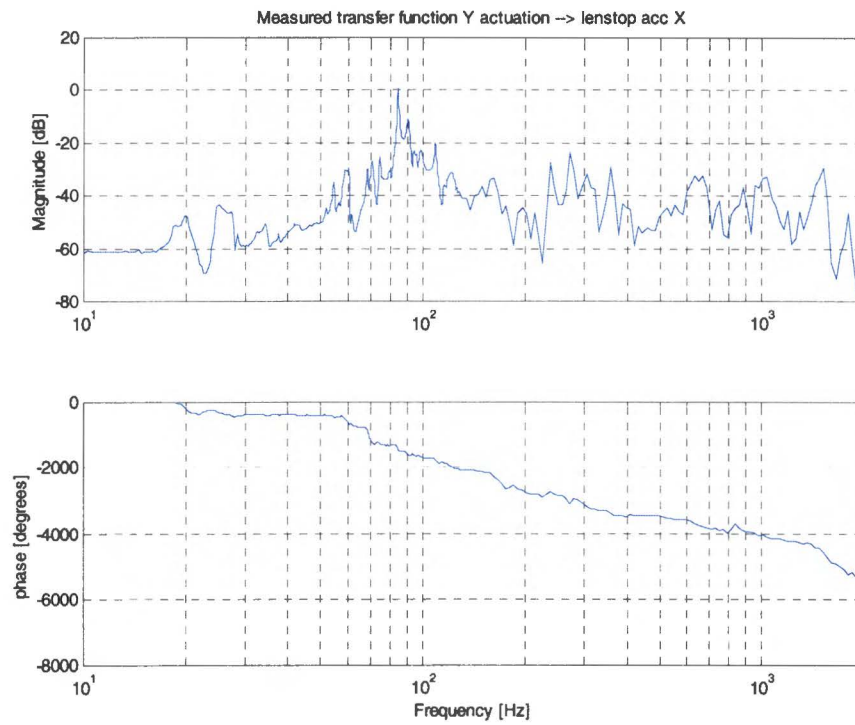


Figure B.3: Measured FRF Y actuation [V] → LA X [m/s^2]

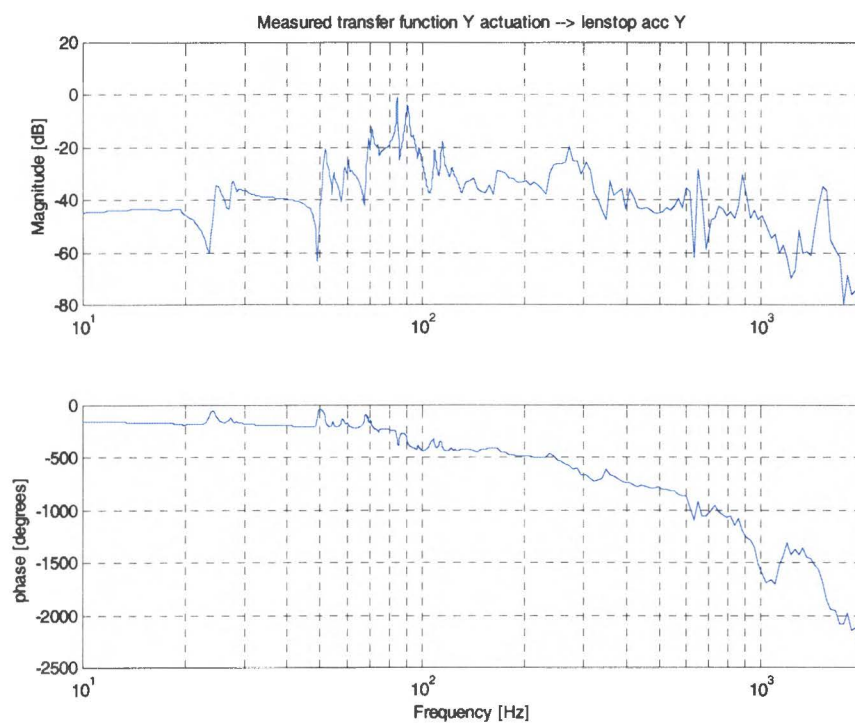


Figure B.4: Measured FRF Y actuation [V] → LA Y [m/s^2]

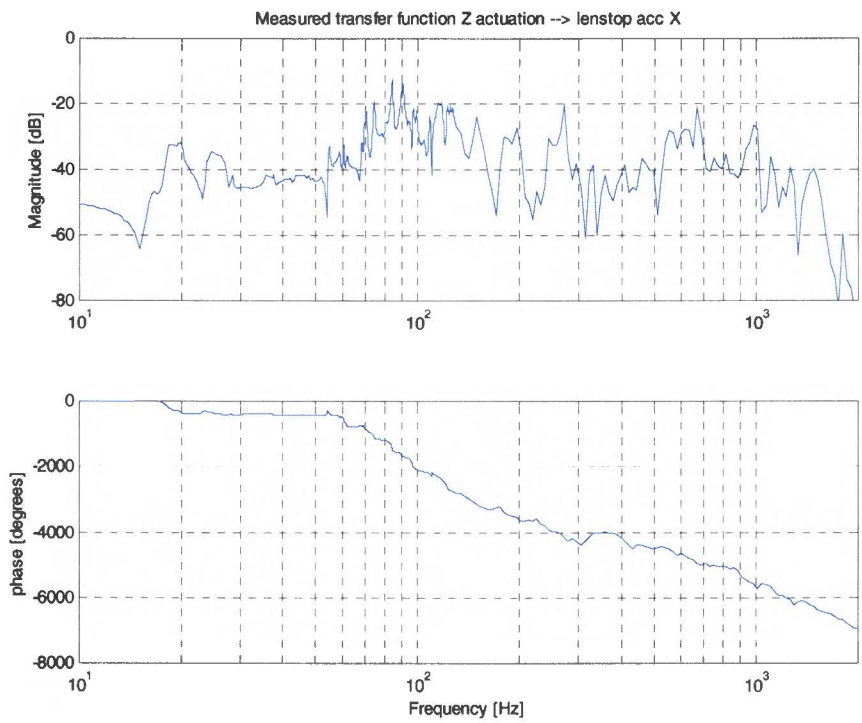


Figure B.5: Measured FRF Z actuation [V] → LA X [m/s²]

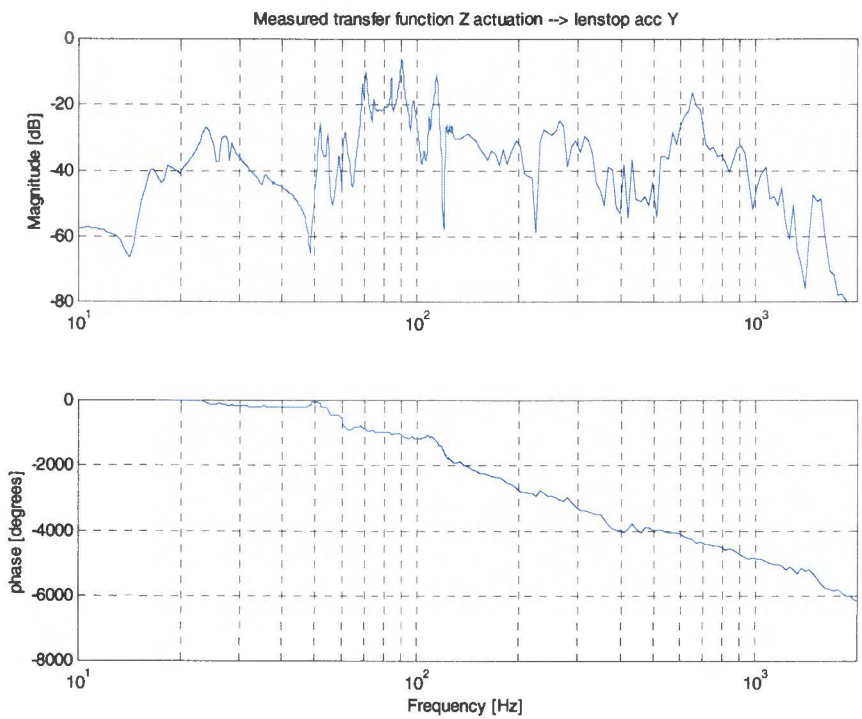


Figure B.6: Measured FRF Z actuation [V] → LA Y [m/s²]

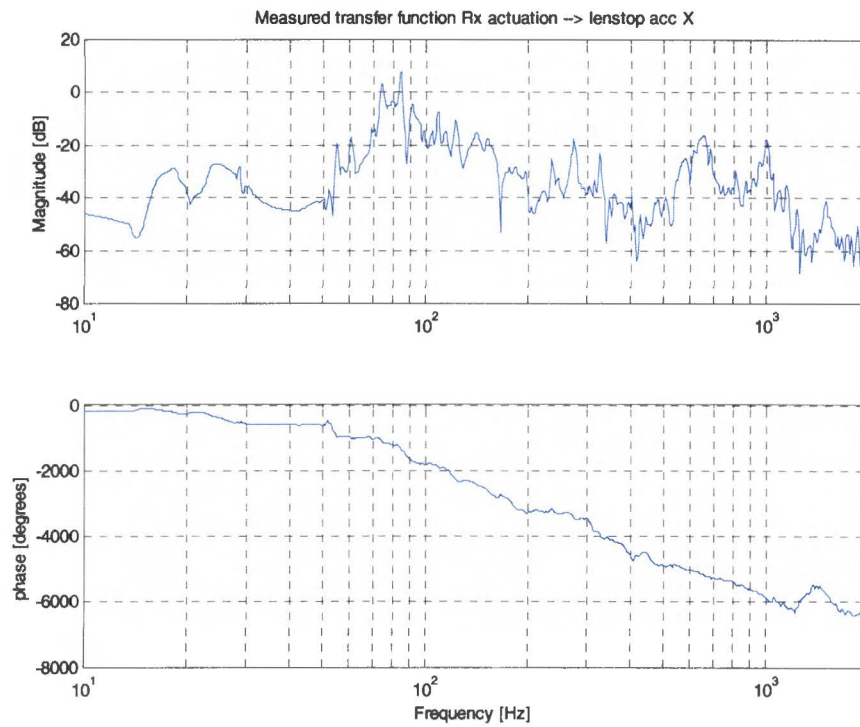


Figure B.7: Measured FRF Rx actuation [V] \rightarrow LA X [m/s^2]

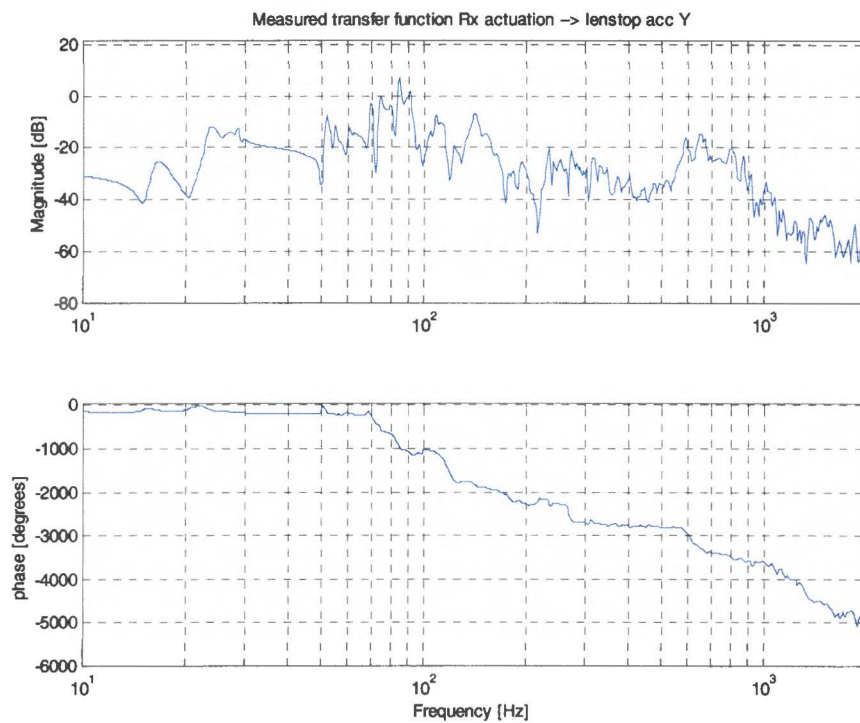


Figure B.8: Measured FRF Rx actuation [V] \rightarrow LA Y [m/s^2]

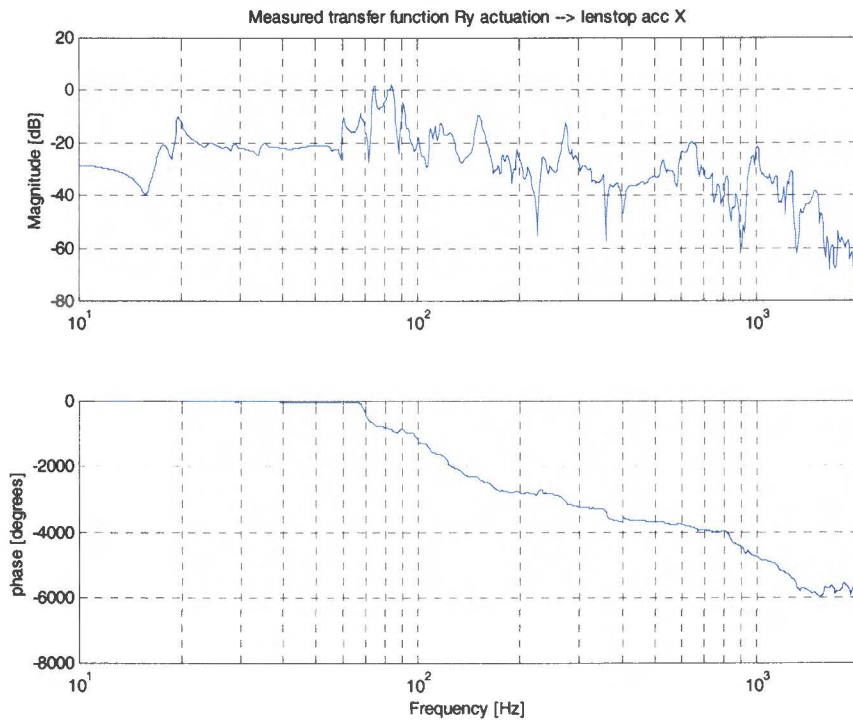


Figure B.9: Measured FRF Ry actuation [V] \rightarrow LA X [m/s^2]

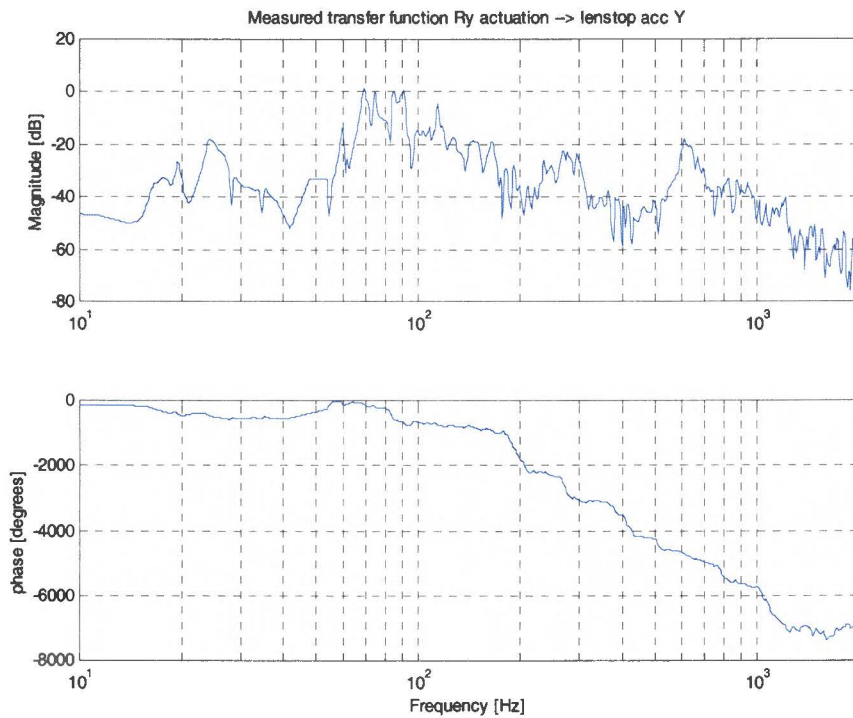


Figure B.10: Measured FRF Ry actuation [V] \rightarrow LA Y [m/s^2]

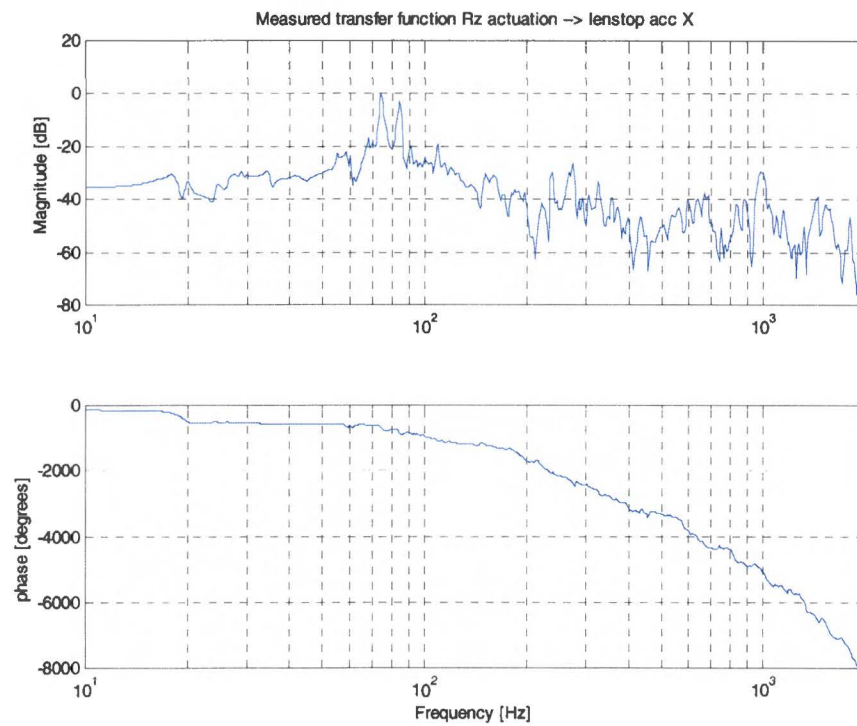


Figure B.11: Measured FRF Rz actuation [V] → LA X [m/s^2]

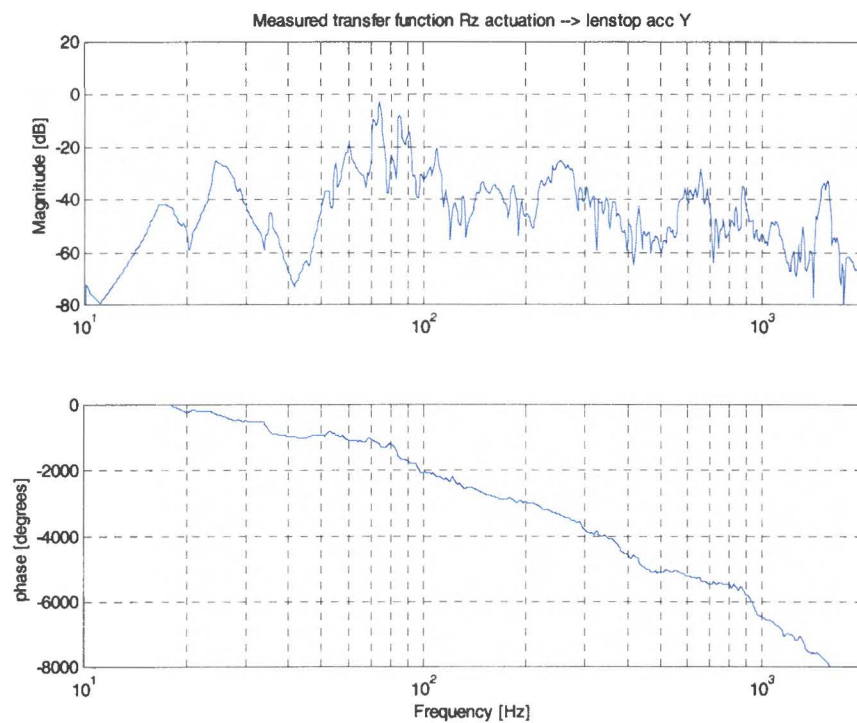


Figure B.12: Measured FRF Rz actuation [V] → LA Y [m/s^2]

Appendix C: Model compared with measurements

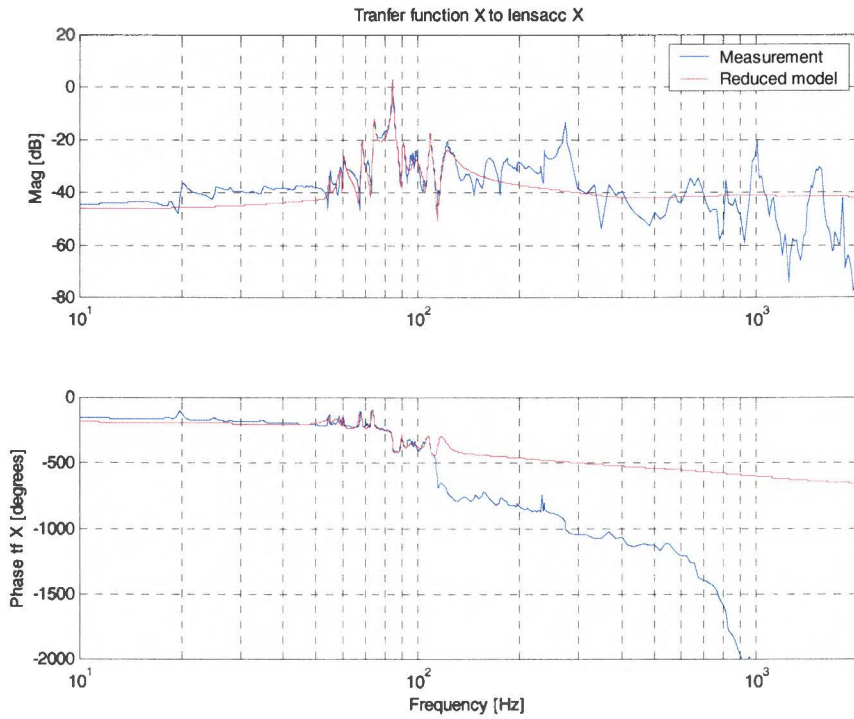


Figure C.1: Measured and modeled FRF X actuation \rightarrow IA X

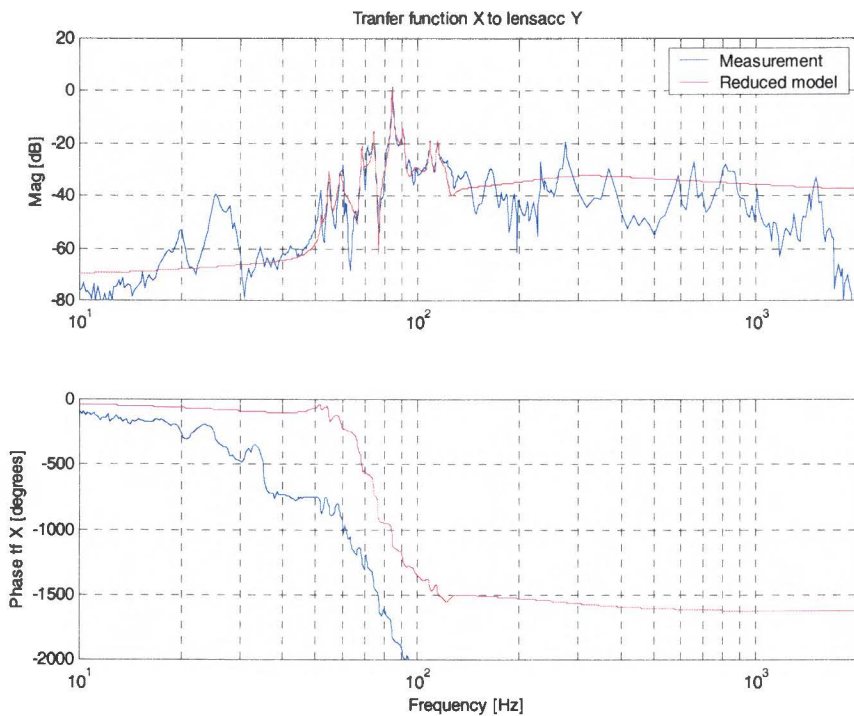


Figure C.2: Measured and modeled FRF X actuation \rightarrow IA Y

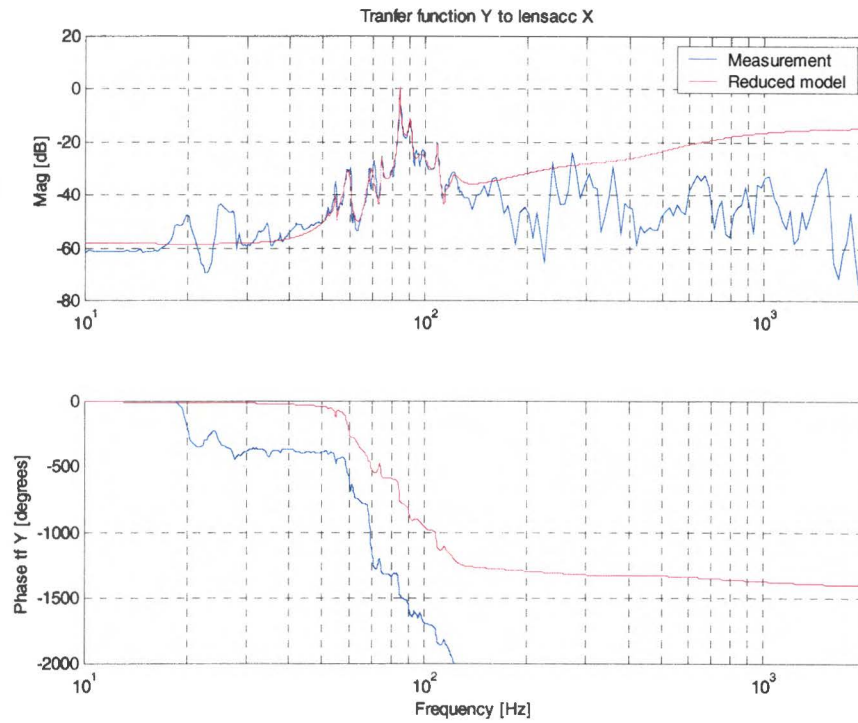


Figure C.3: Measured and modeled FRF Y actuation \rightarrow IA X

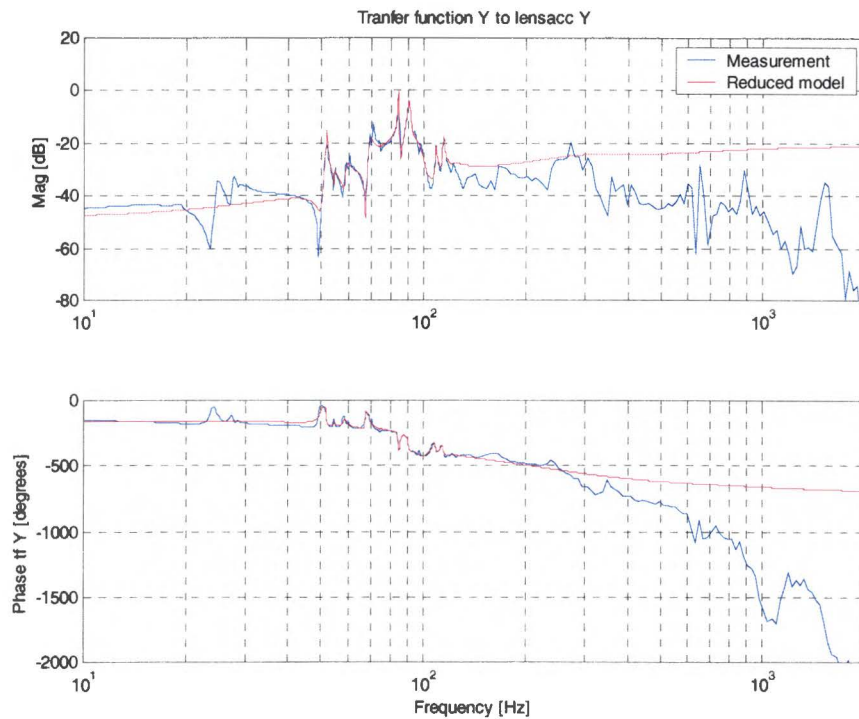


Figure C.4: Measured and modeled FRF Y actuation \rightarrow IA Y

Appendix D: Proportional design

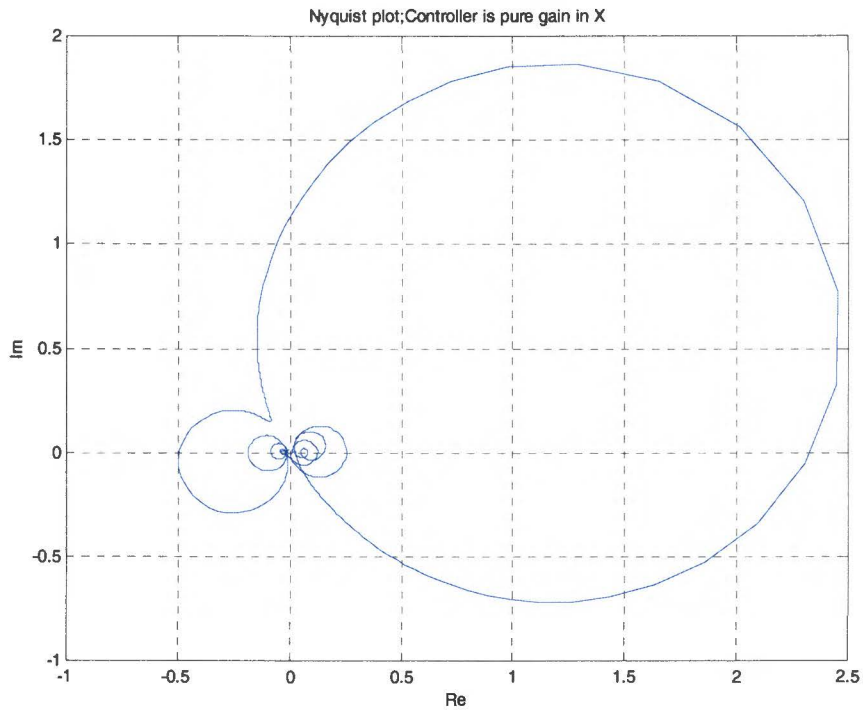


Figure D.1: SISO Nyquist plot for X controller with only gain

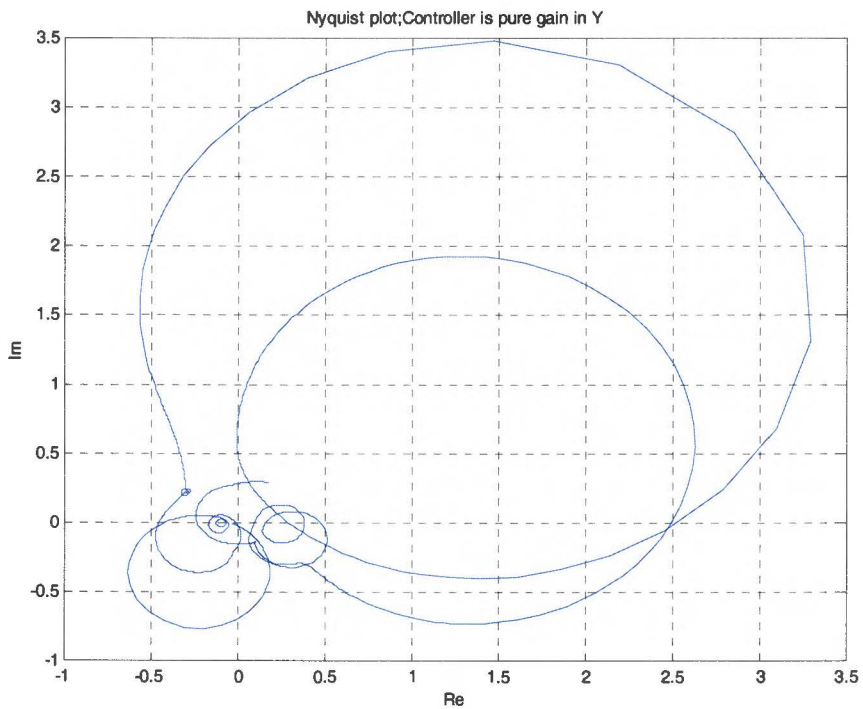


Figure D.2: SISO Nyquist plot for Y controller with only gain

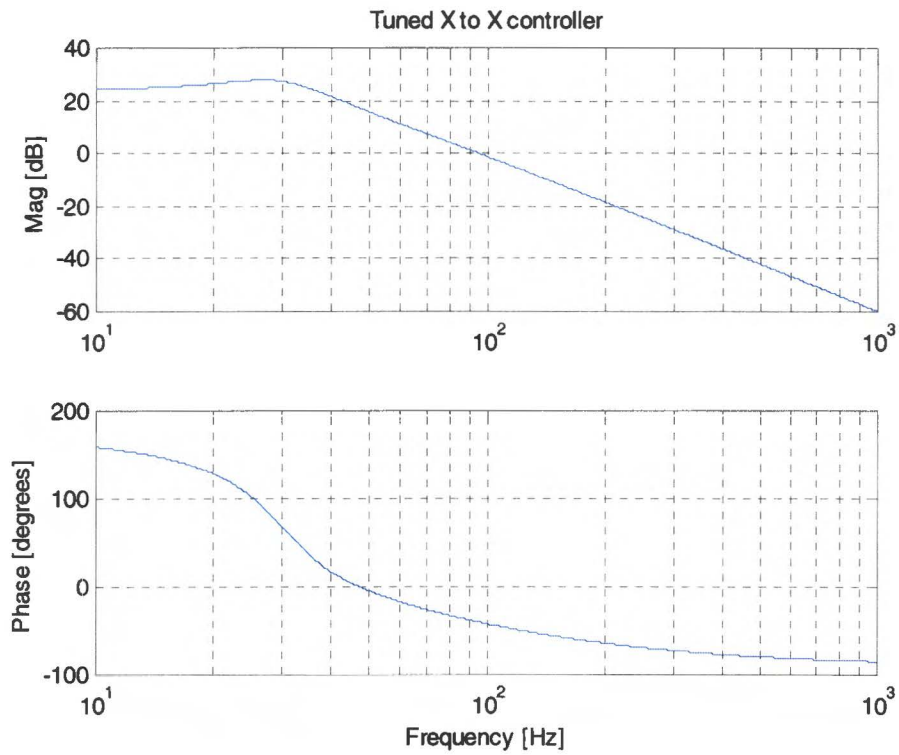


Figure D.3: Tuned X controller

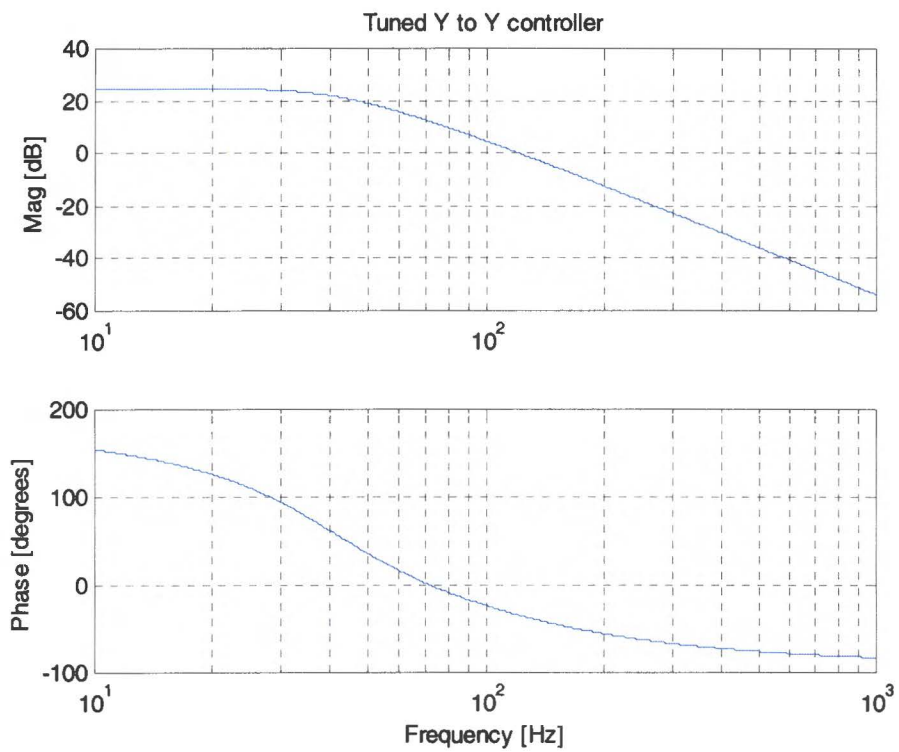


Figure D.4: Tuned Y controller

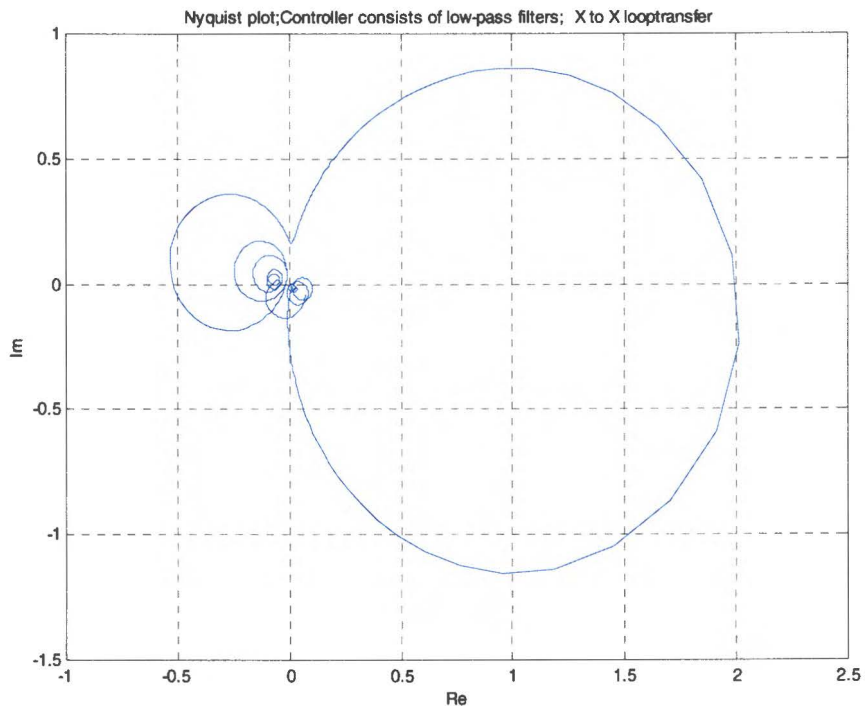


Figure D.5: SISO Nyquist plot for tuned X controller

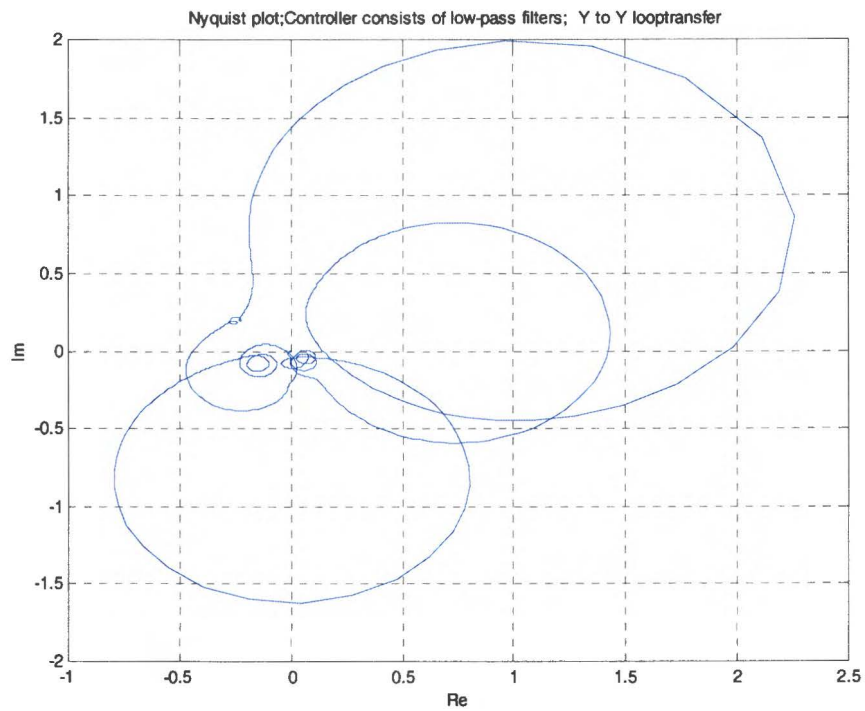


Figure D.6: SISO Nyquist plot for tuned Y controller

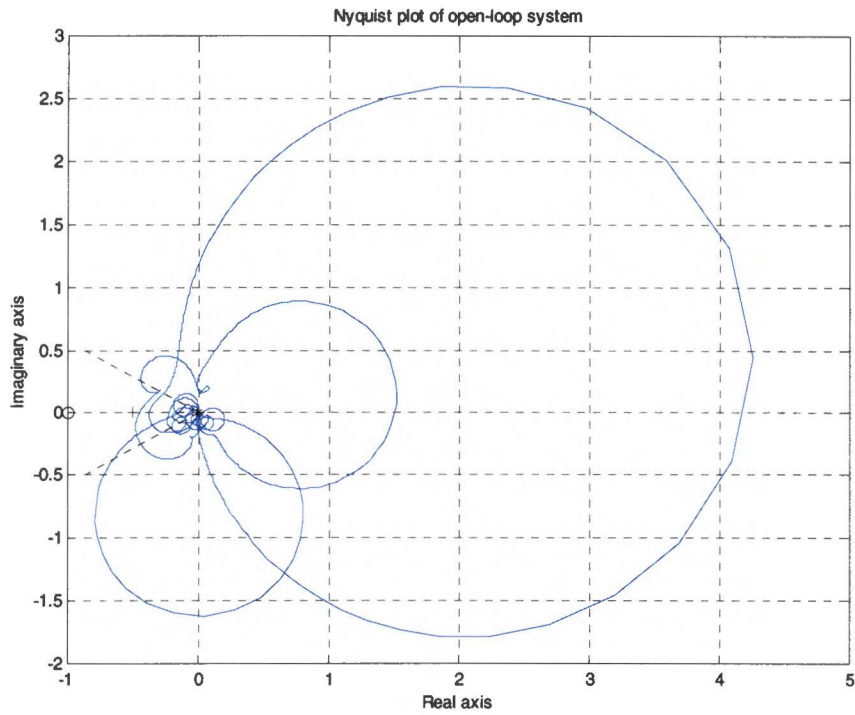


Figure D.7: MIMO Nyquist plot for tuned controllers, modeled system

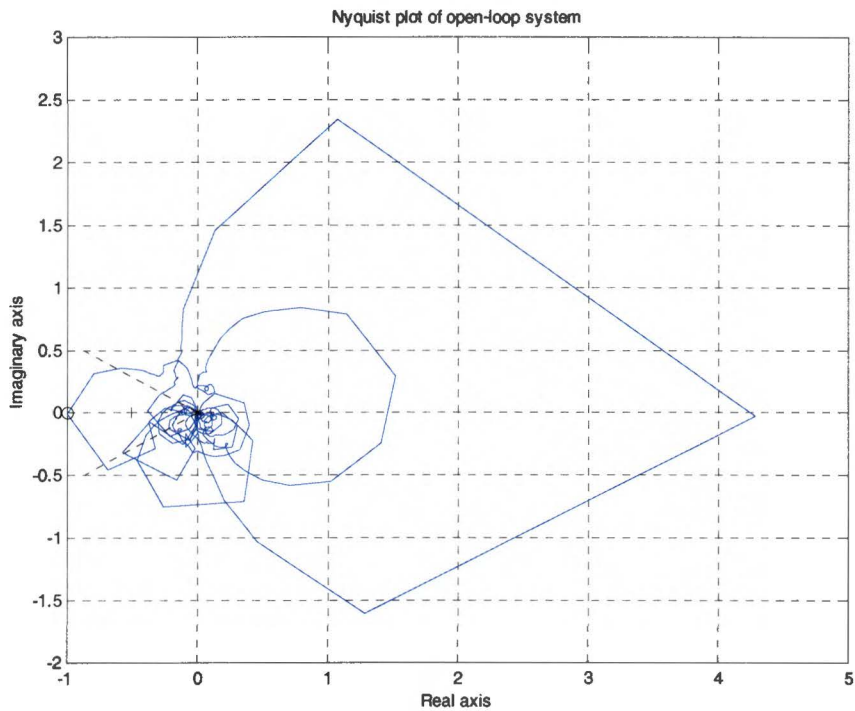


Figure D.8 :MIMO Nyquist plot for tuned controllers, measured system

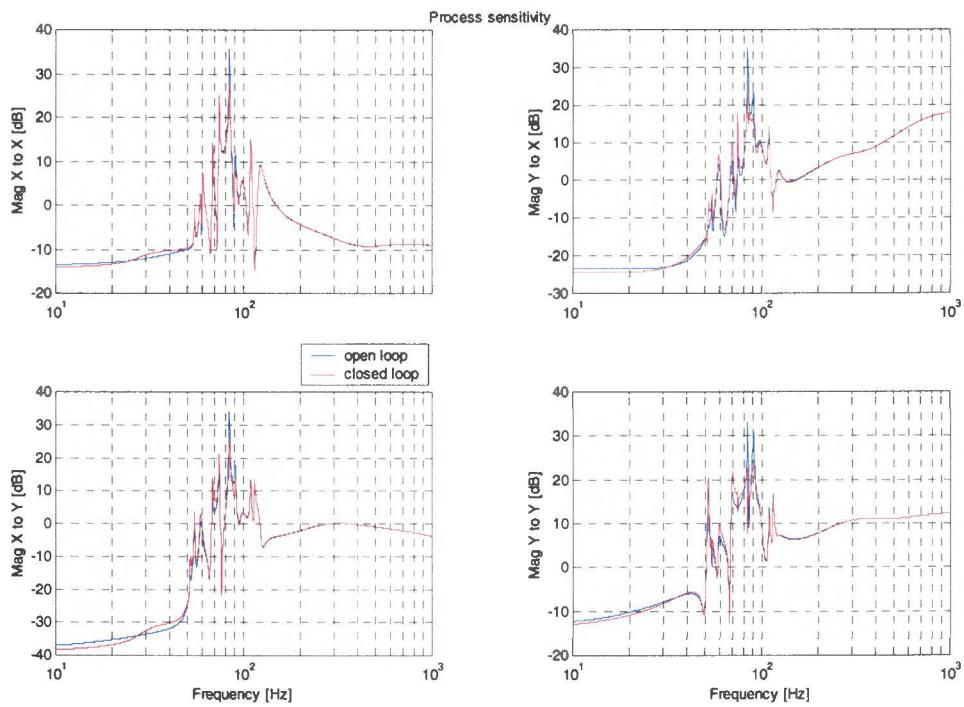


Figure D.9: Process sensitivity

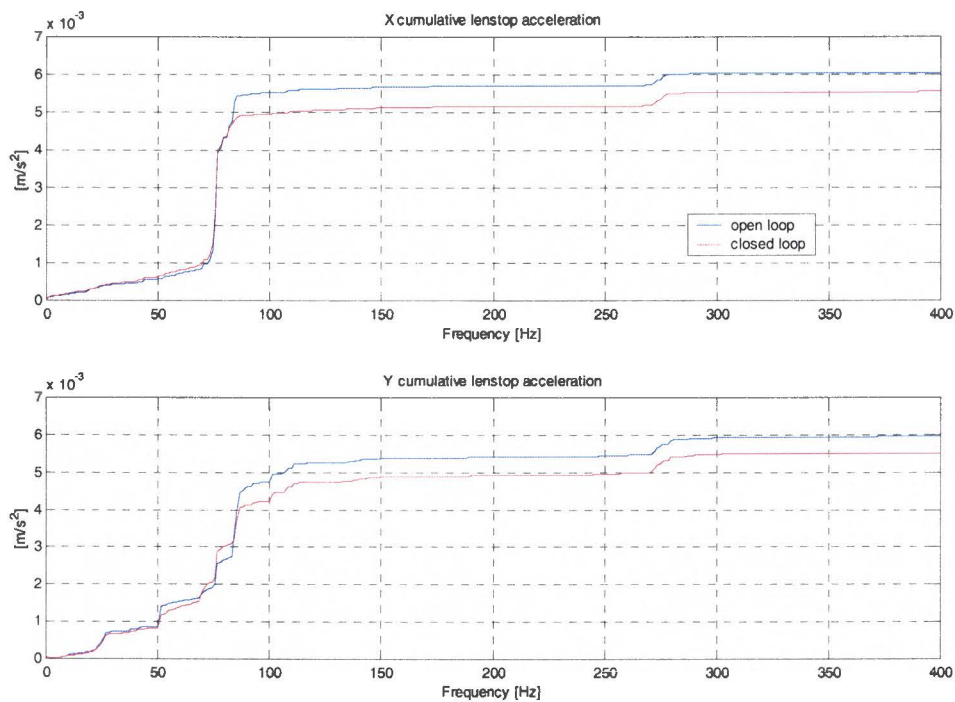


Figure D.10: Cumulative PSD resulting from simulation

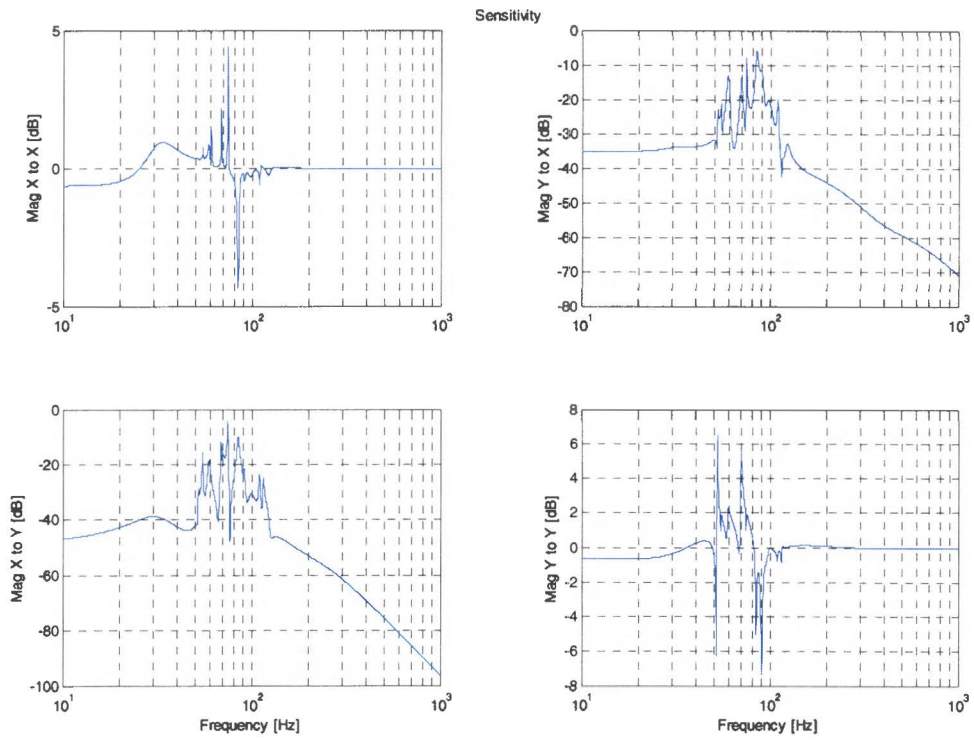


Figure D.11: Sensitivity

Appendix E: LQG Design

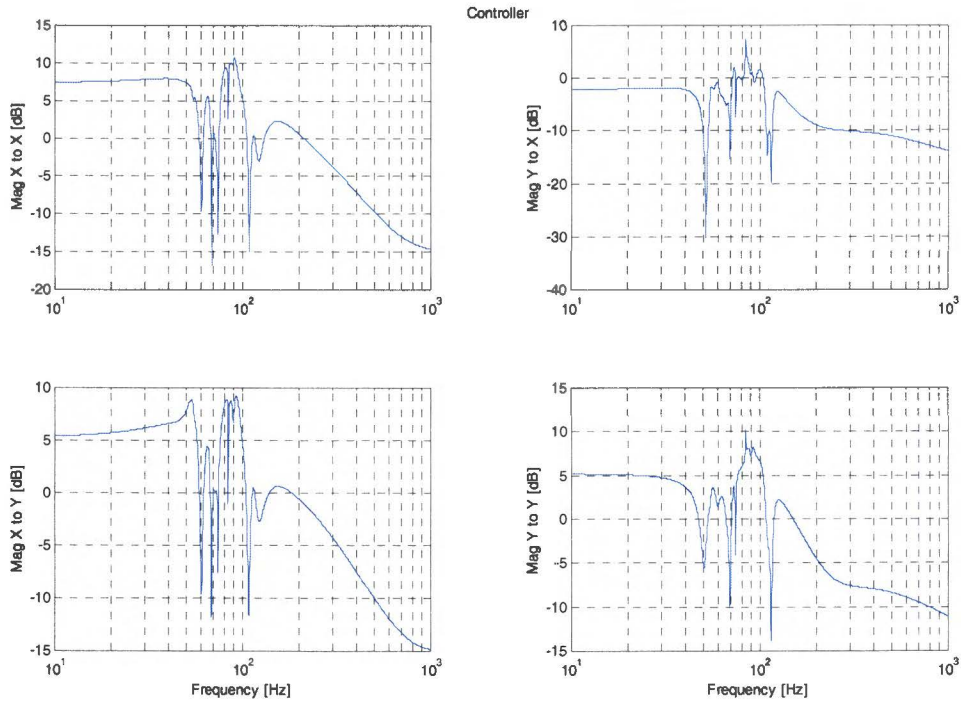


Figure E.1: LQG controller

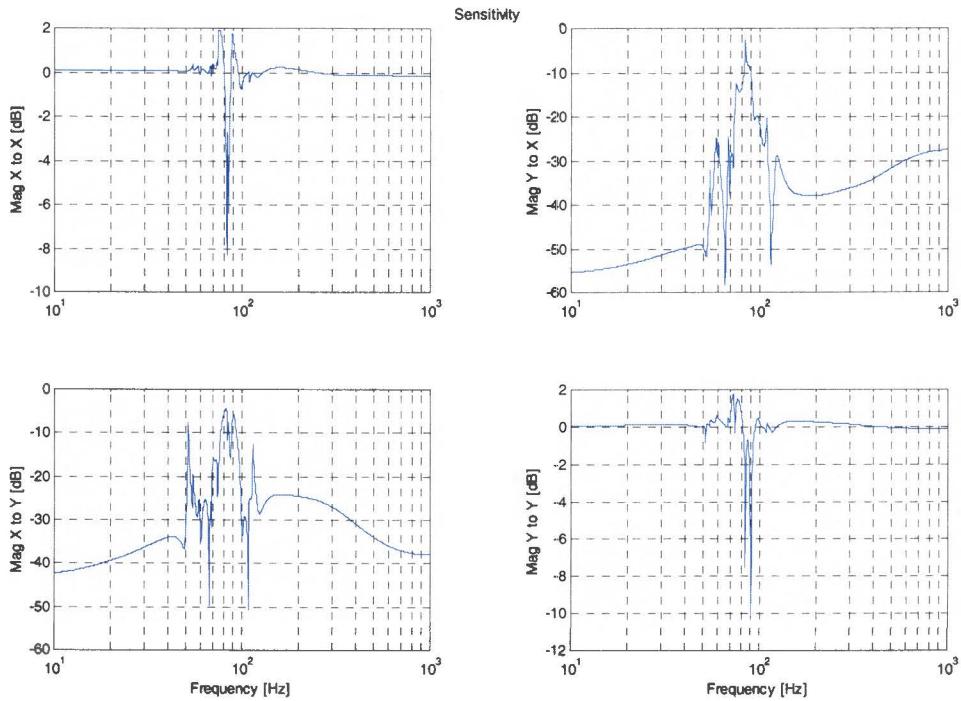


Figure E.2: Sensitivity

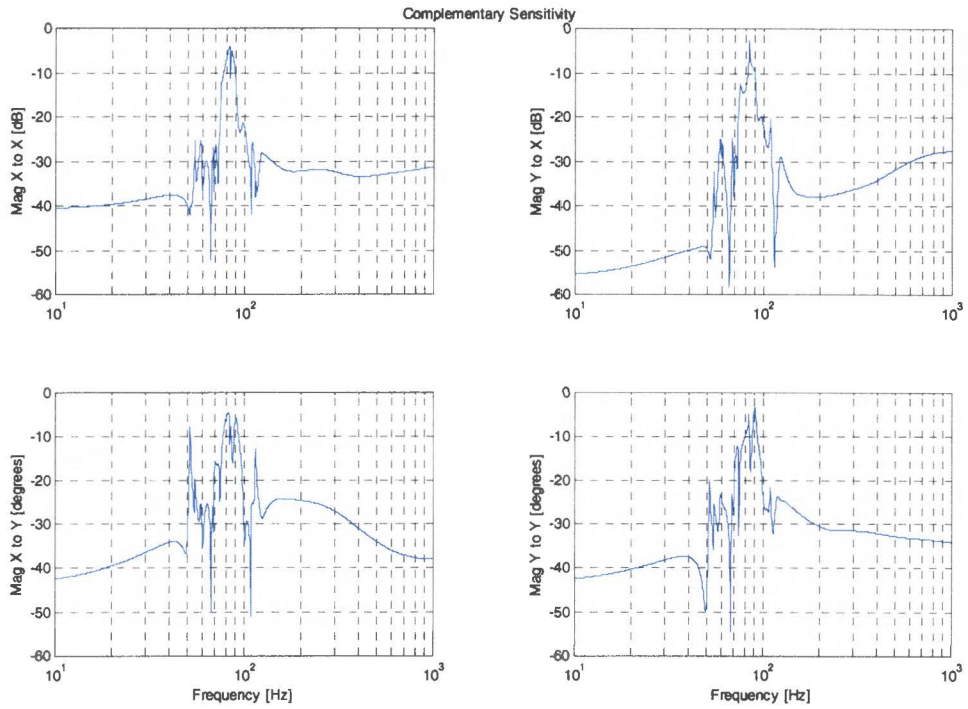


Figure E.3: Complementary sensitivity

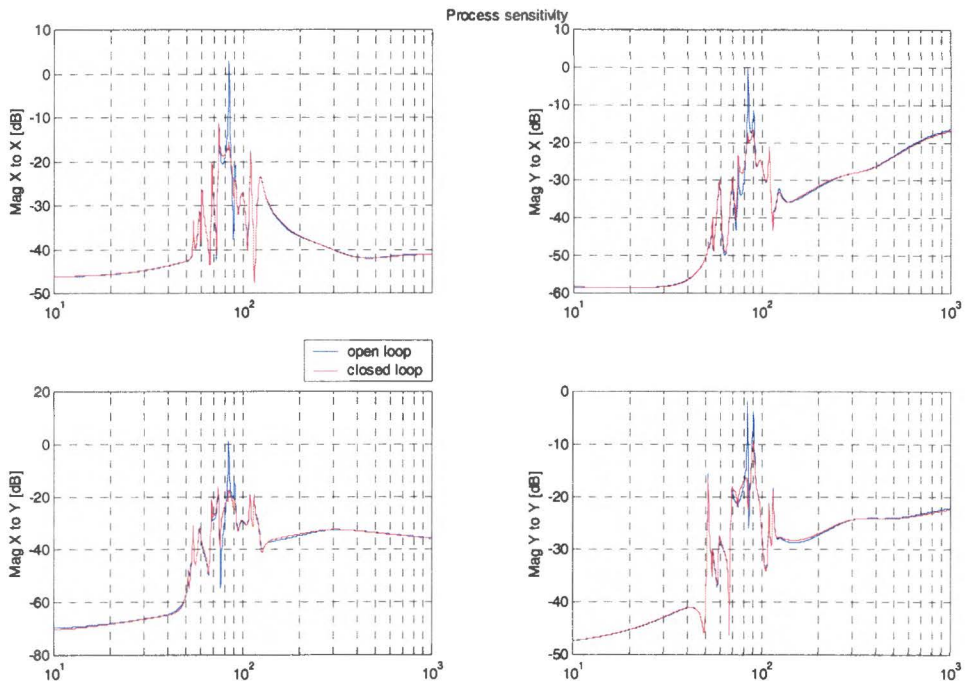


Figure E.4: Process sensitivity

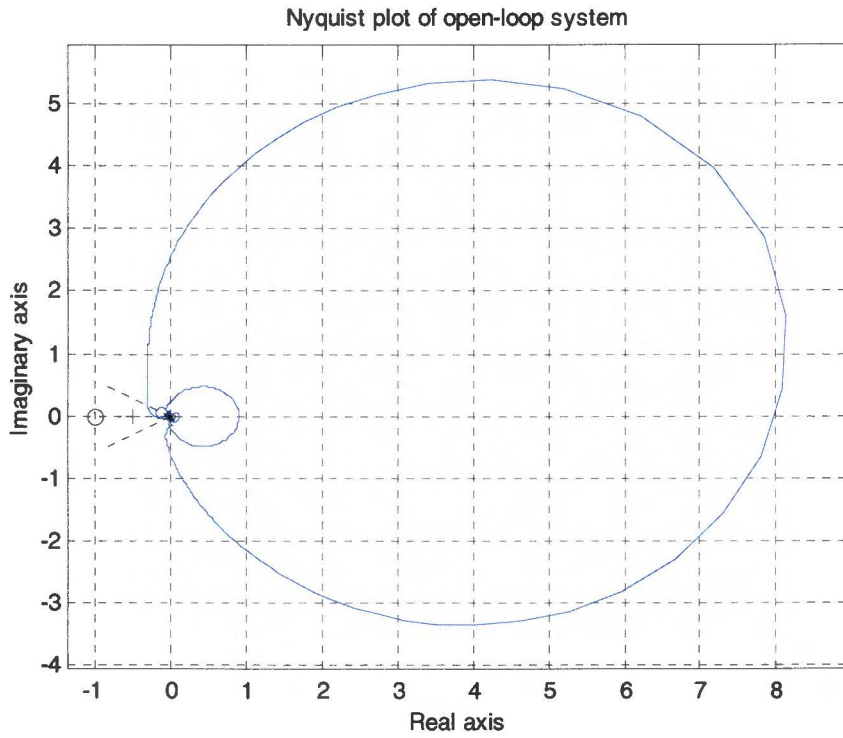


Figure E.5: MIMO Nyquist plot with modeled system

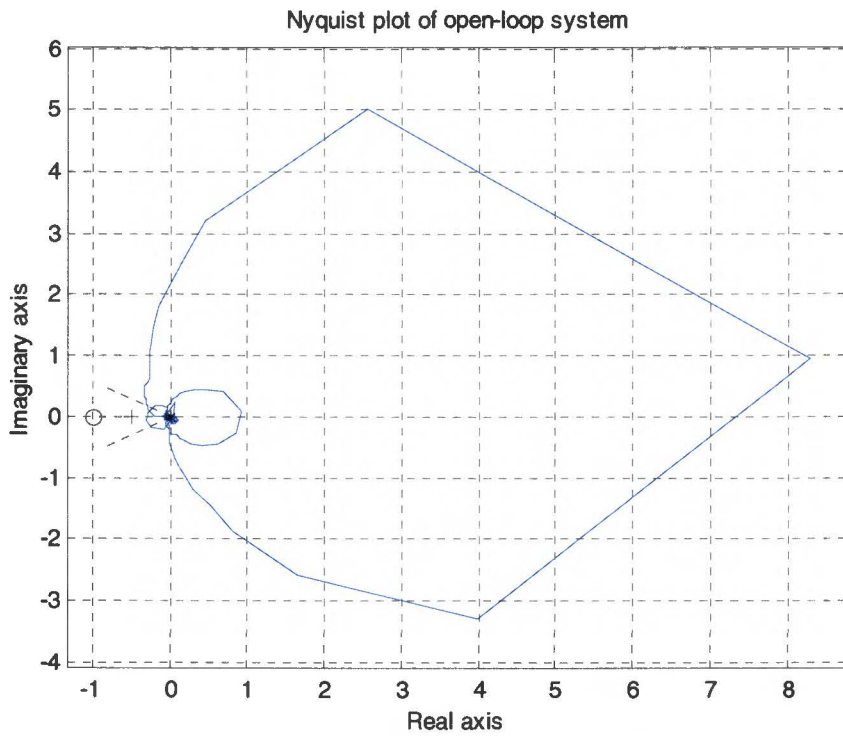


Figure E.6: MIMO Nyquist plot with measured system

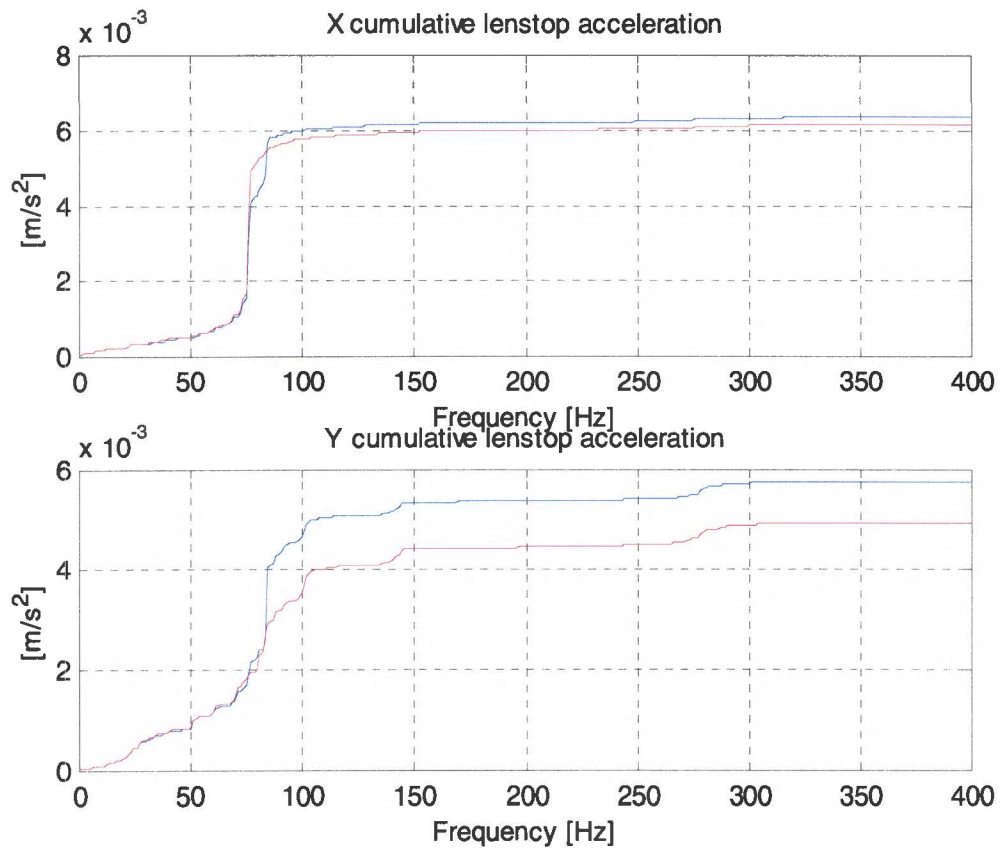


Figure E.7: Cumulative PSD resulting from simulation

Appendix F: H^∞ design, augmented plant setup 1

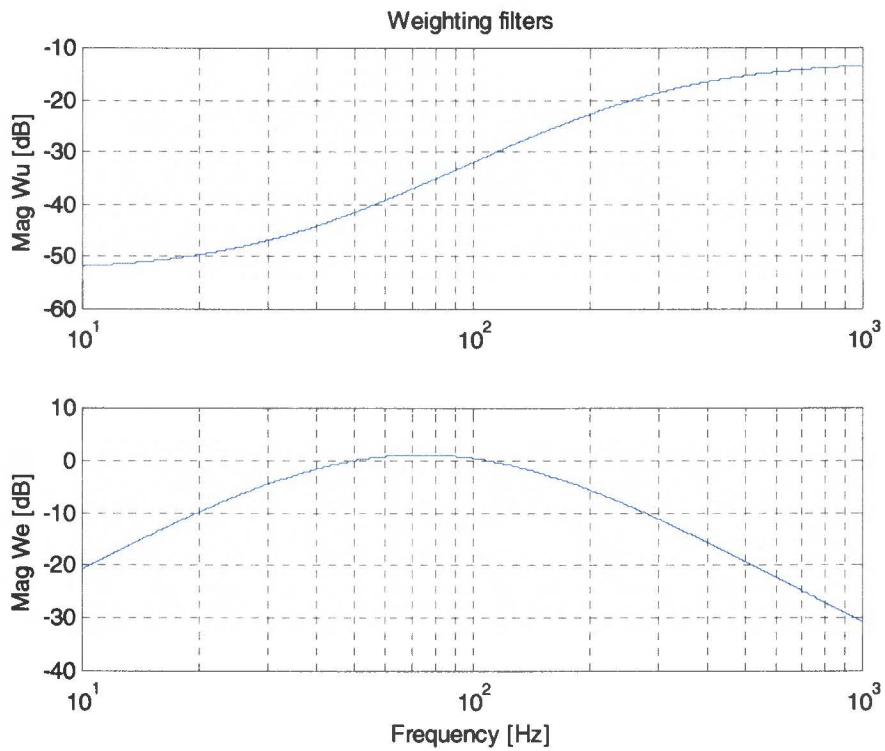


Figure F.1: Weighting filters

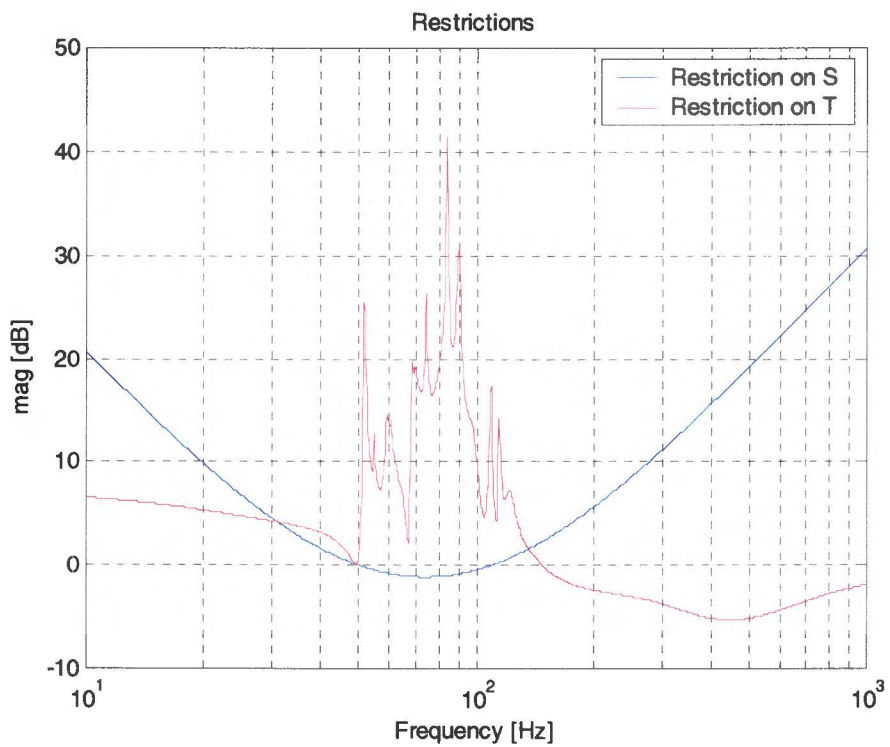


Figure F.2: (Complementary) Sensitivity borders

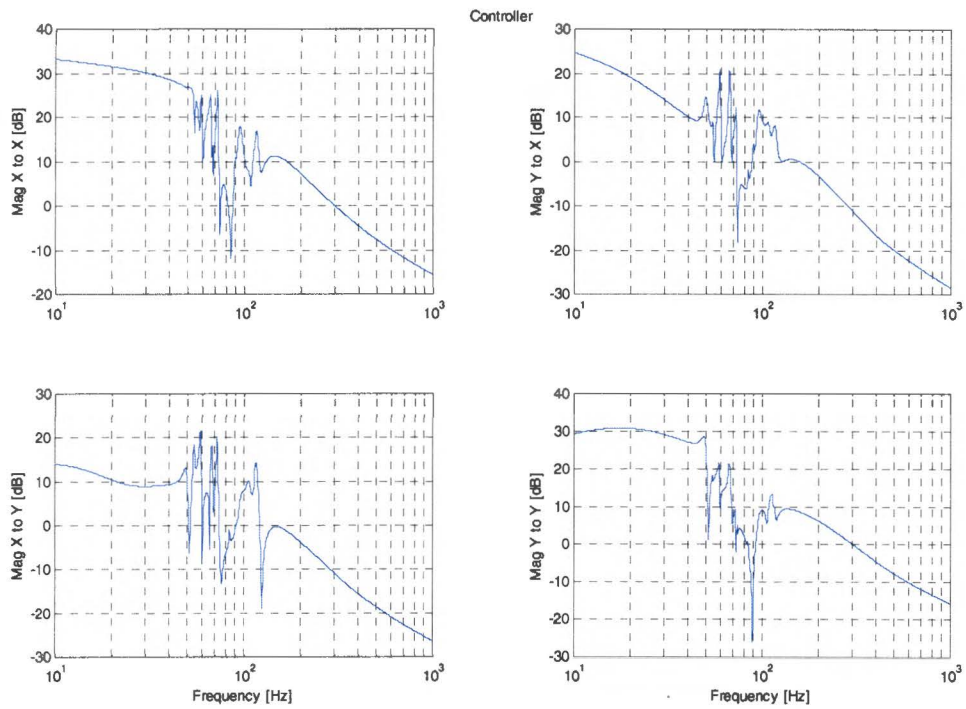


Figure F.3: Controller

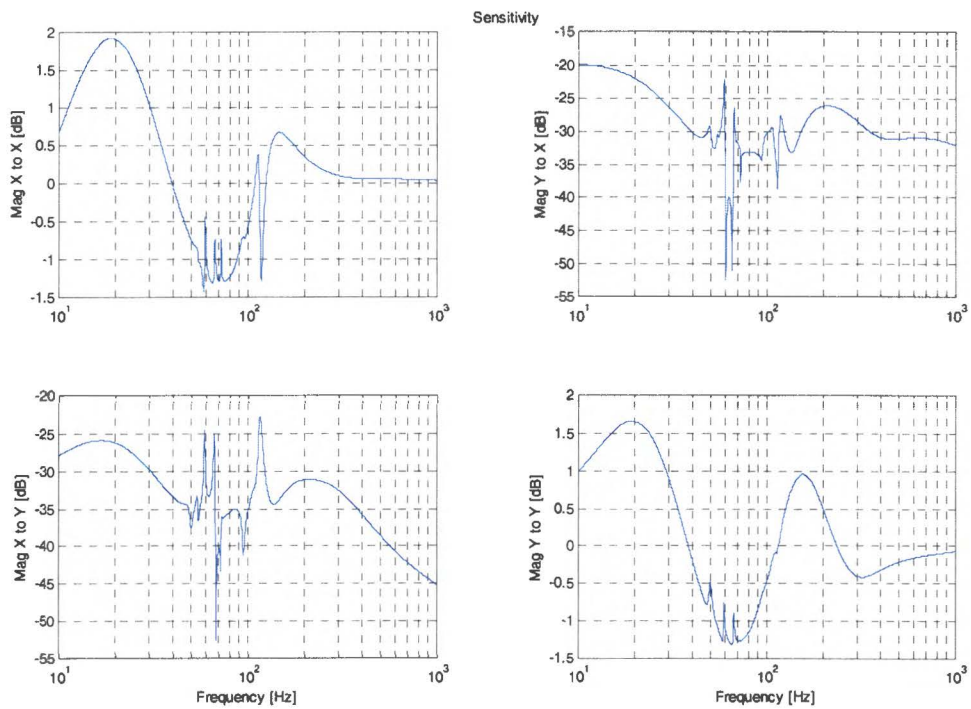


Figure F.4: Sensitivity

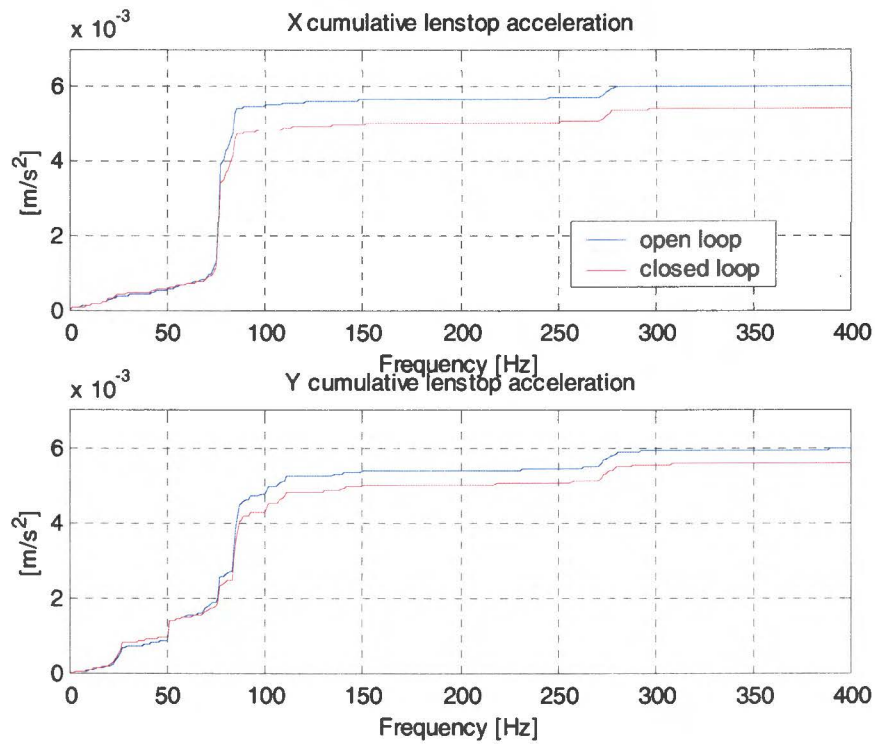


Figure F.5 Cumulative PSD resulting from simulation

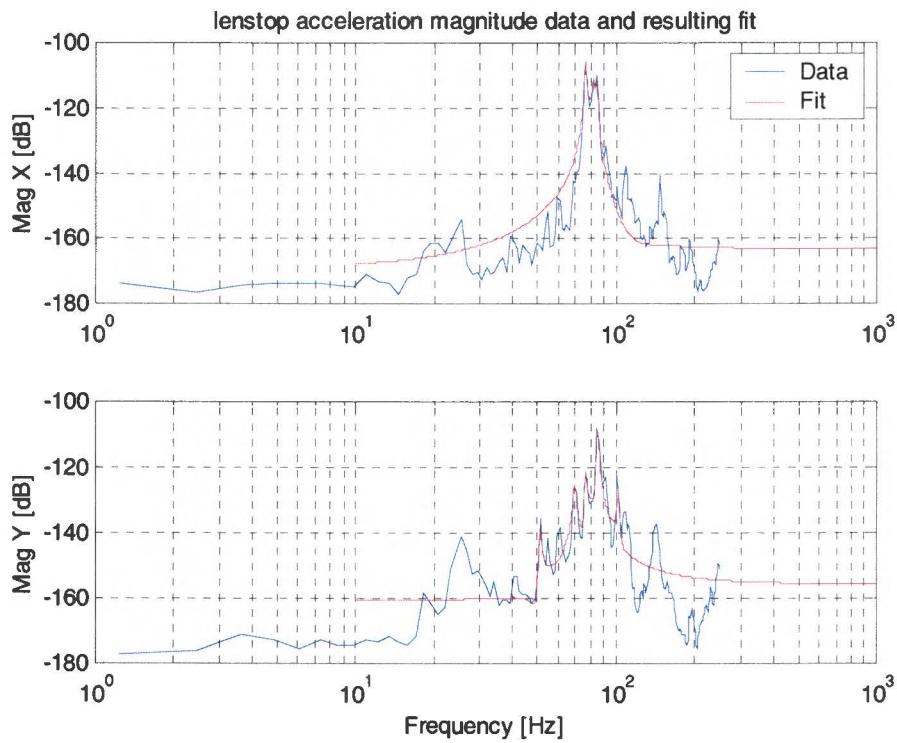


Figure F.6: V_d as lenstop disturbance fits

Appendix G: H^∞ design, augmented plant setup 2

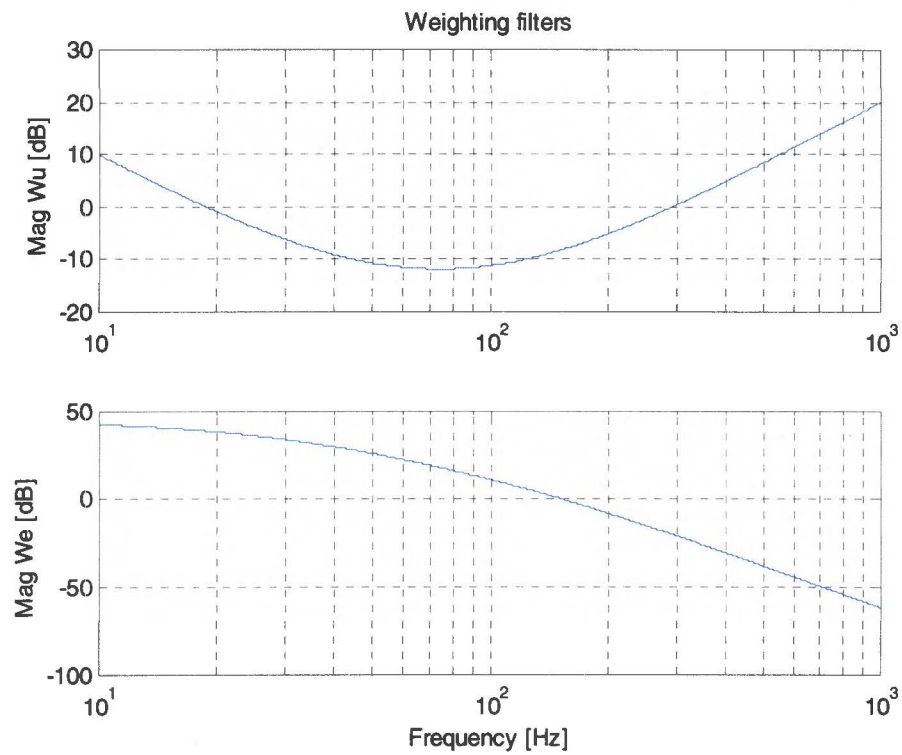


Figure G.1: Weighting filters

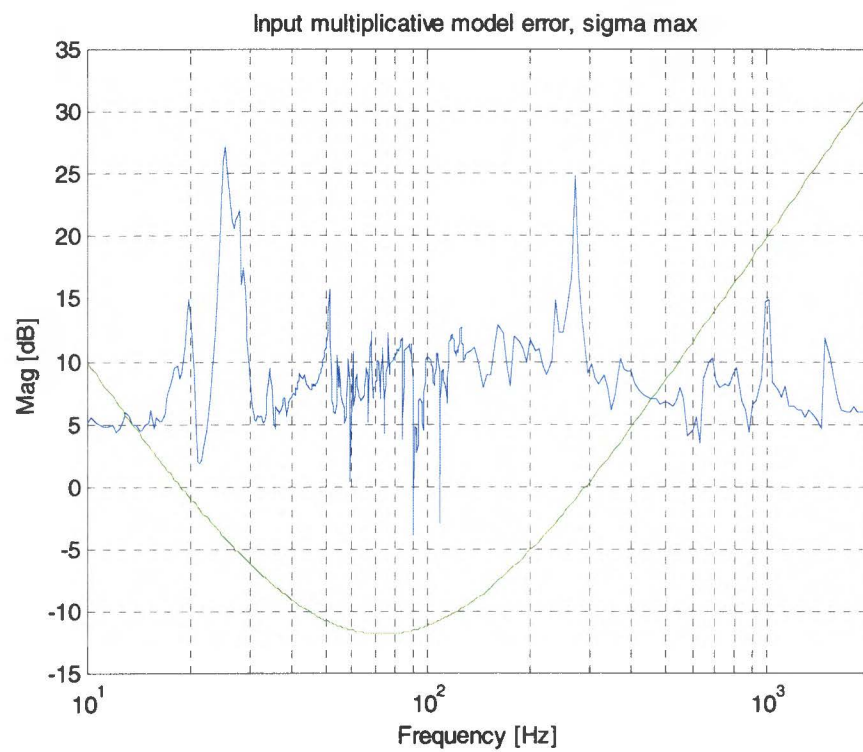


Figure G.2: Input multiplicative model error

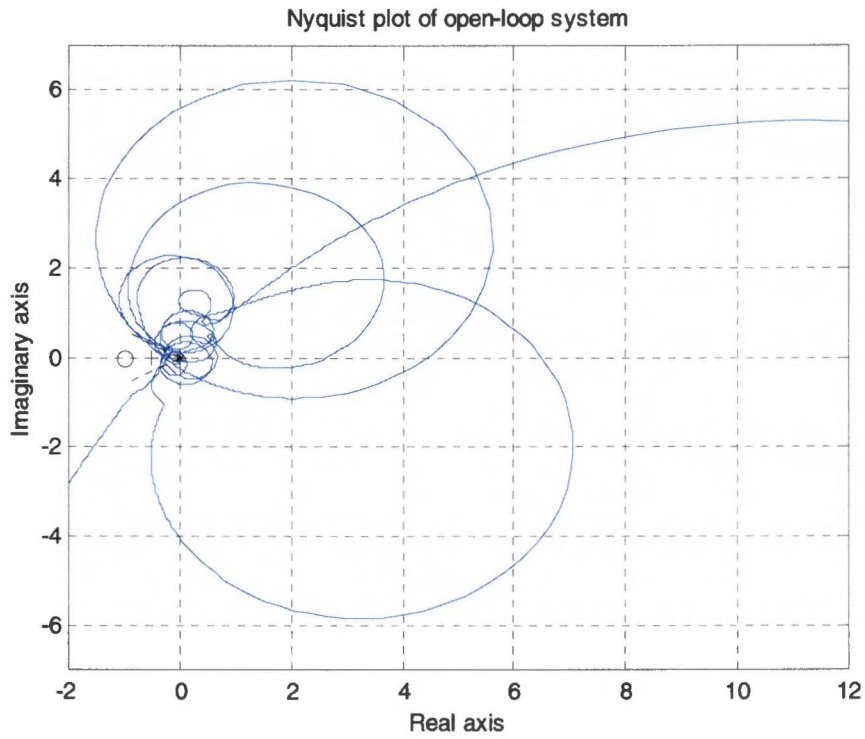


Figure G.3 MIMO Nyquist plot with modeled system

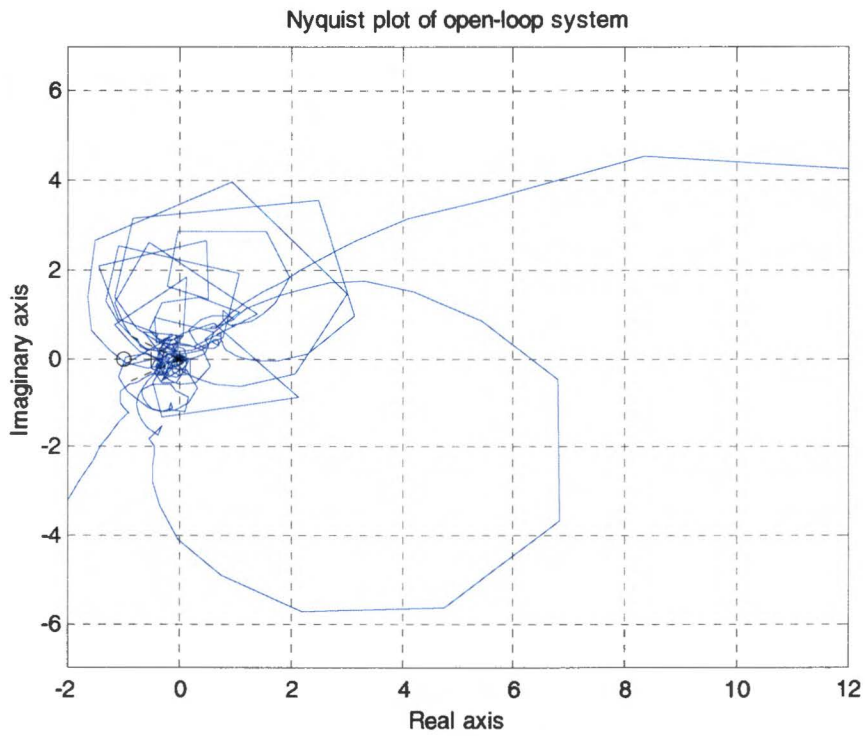


Figure G.4 MIMO Nyquist plot with measured system

Appendix H: H^∞ design, augmented plant setup 3

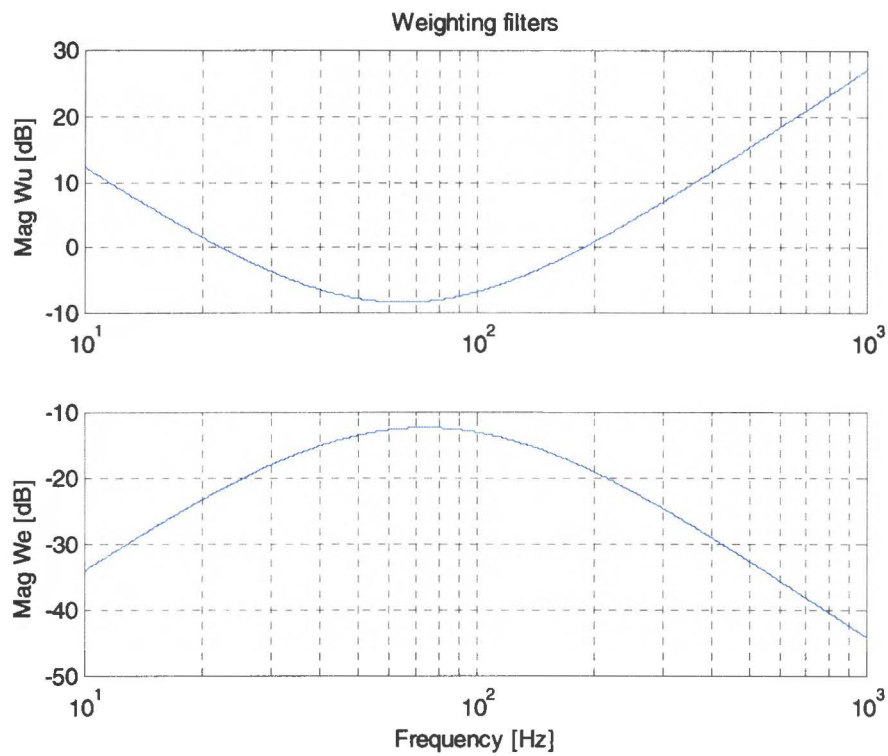


Figure H.1: Weighting filters

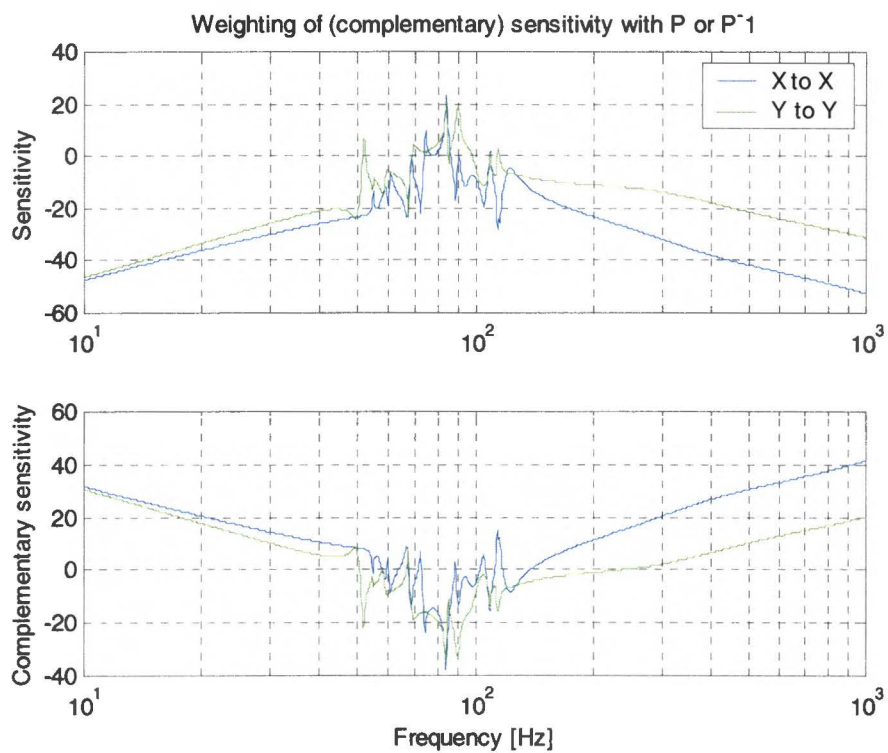


Figure H.2: $|W_e P_i V_u|$ and $|W_u P^{-1} V_d|$

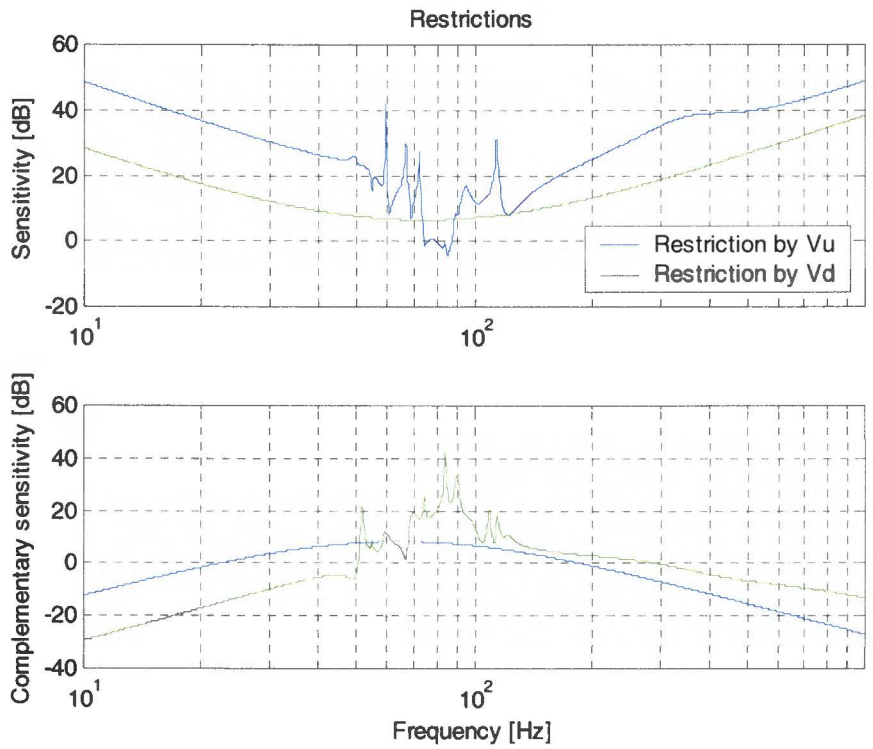


Figure H.3: Restrictions on (complementary) sensitivity

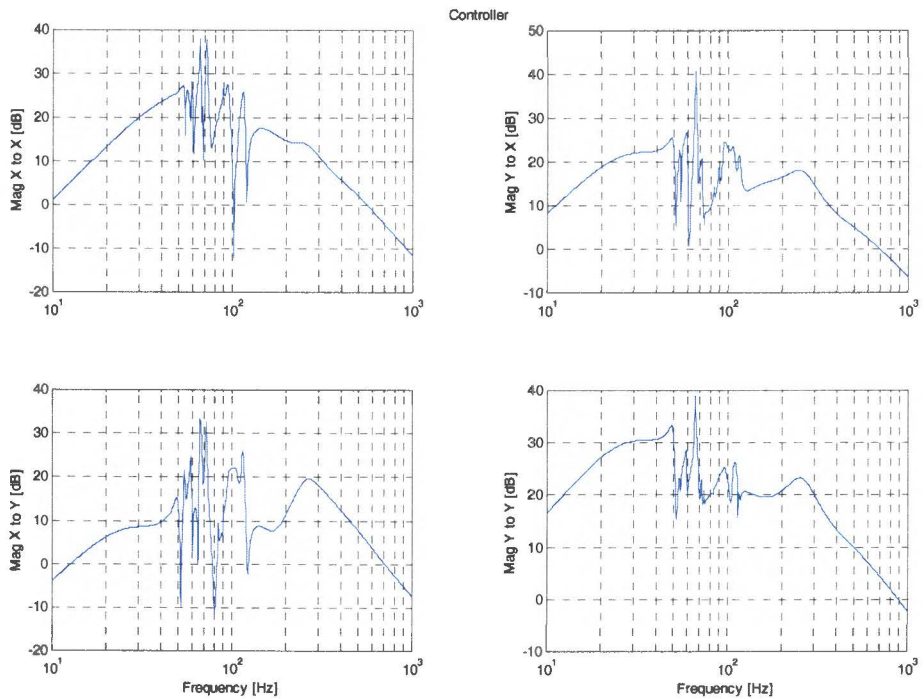


Figure H.4: Controller

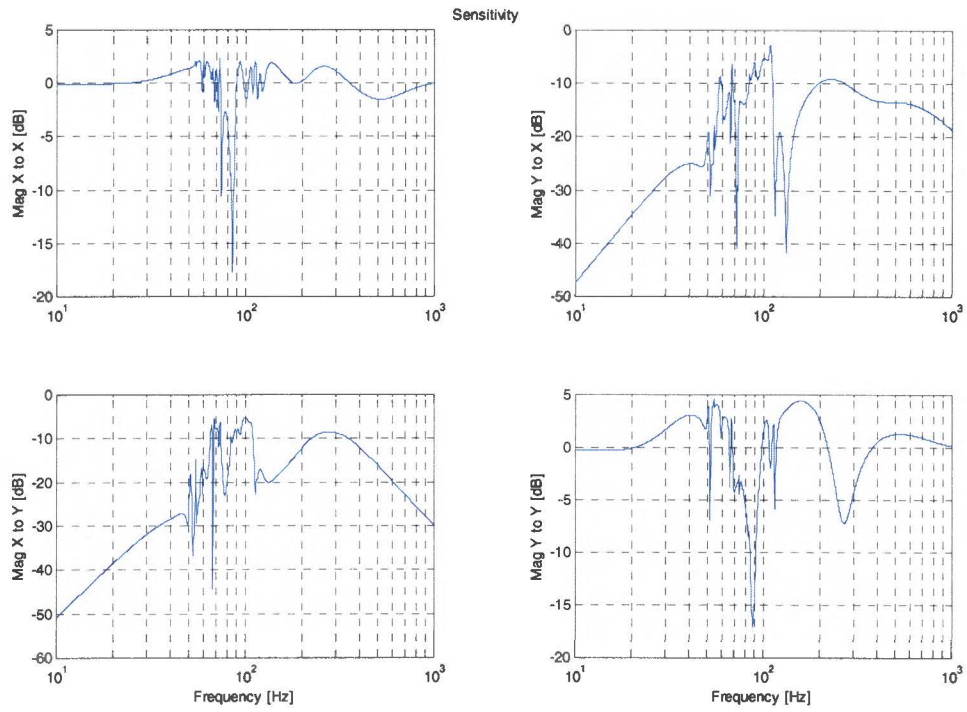


Figure H.5: Sensitivity

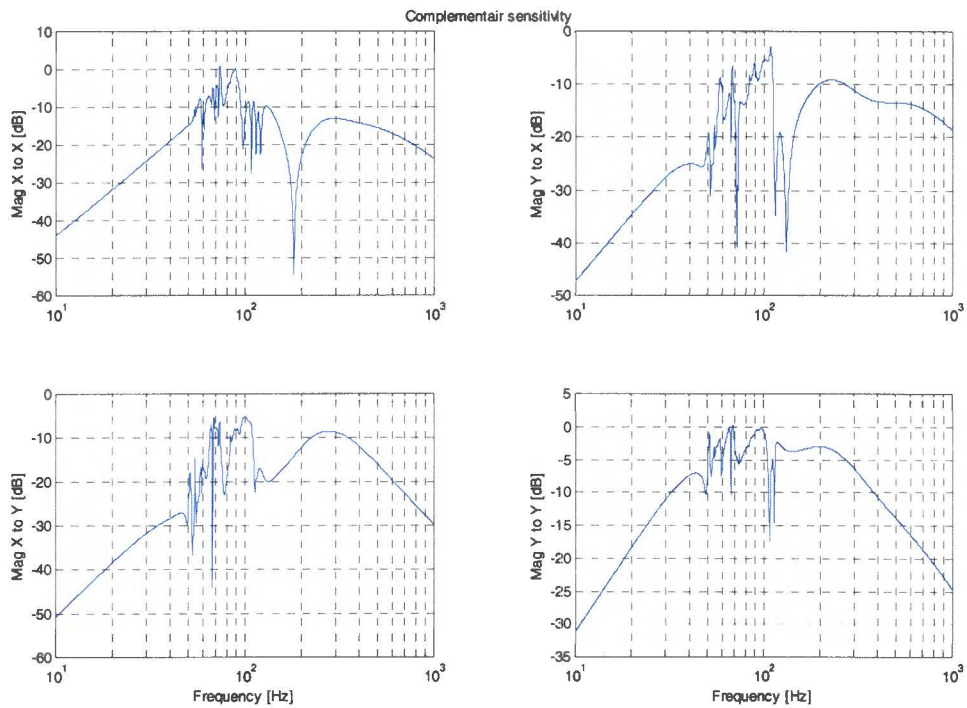


Figure H.6: Complementary sensitivity

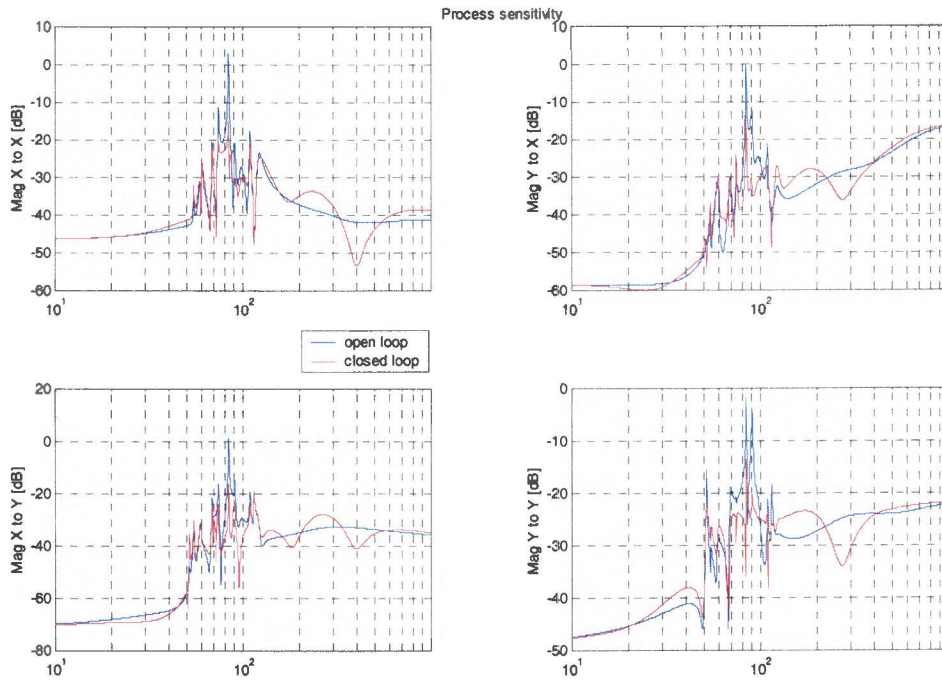


Figure H.7: Process sensitivity

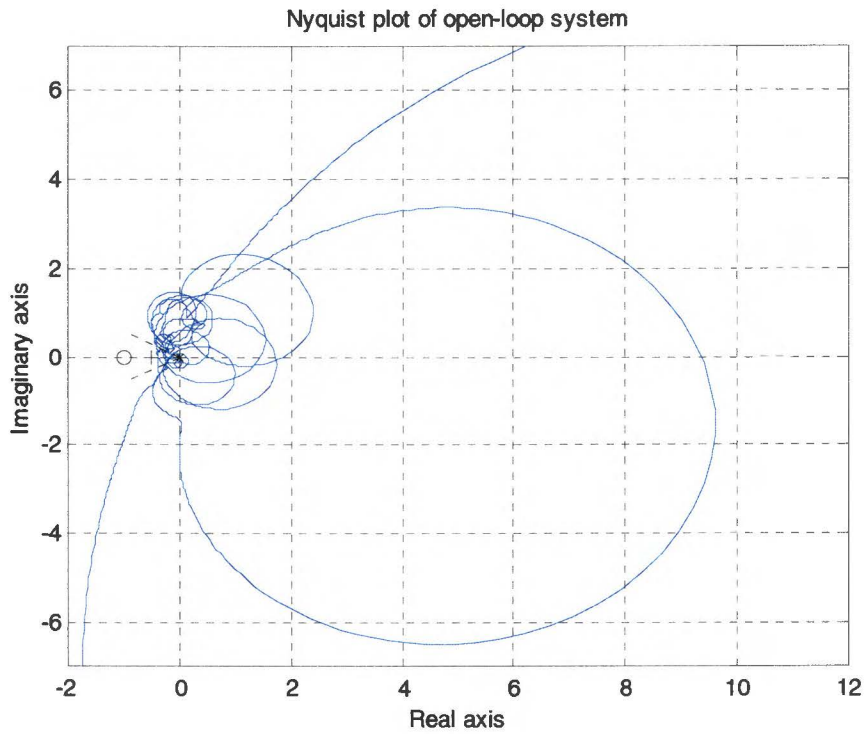


Figure H.8: MIMO Nyquist plot with modeled system

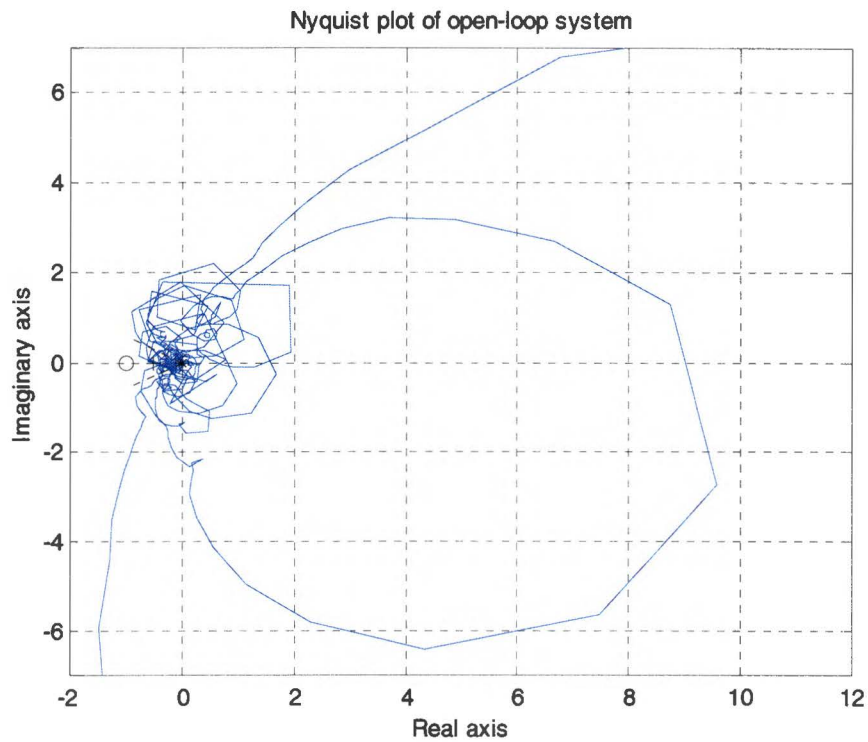


Figure H.9: MIMO Nyquist plot with measured system

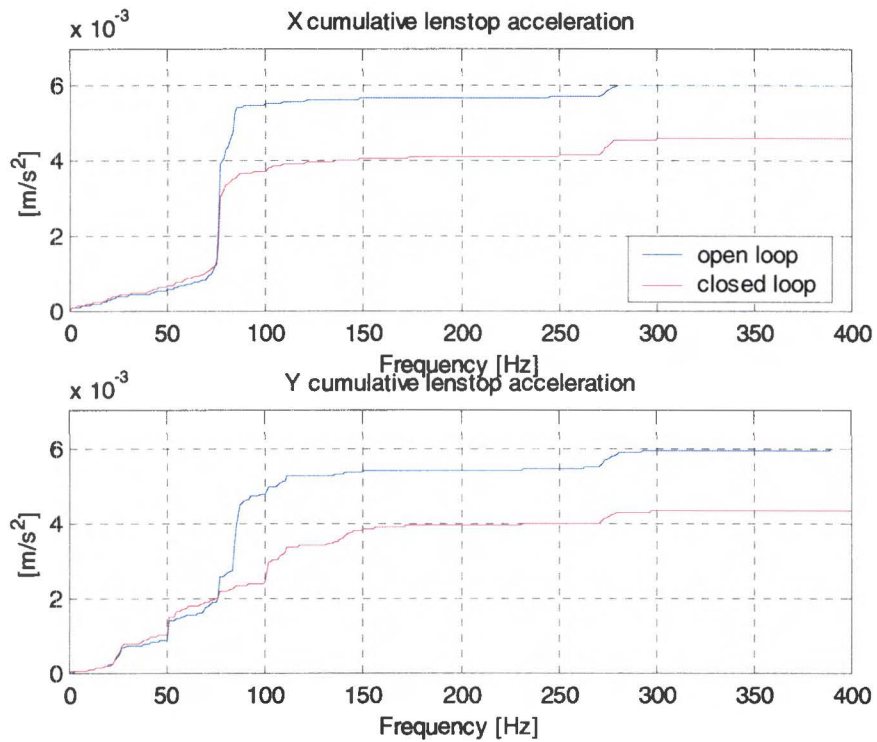


Figure H.10: Cumulative PSD resulting from simulation

Appendix I: Controller implementation results

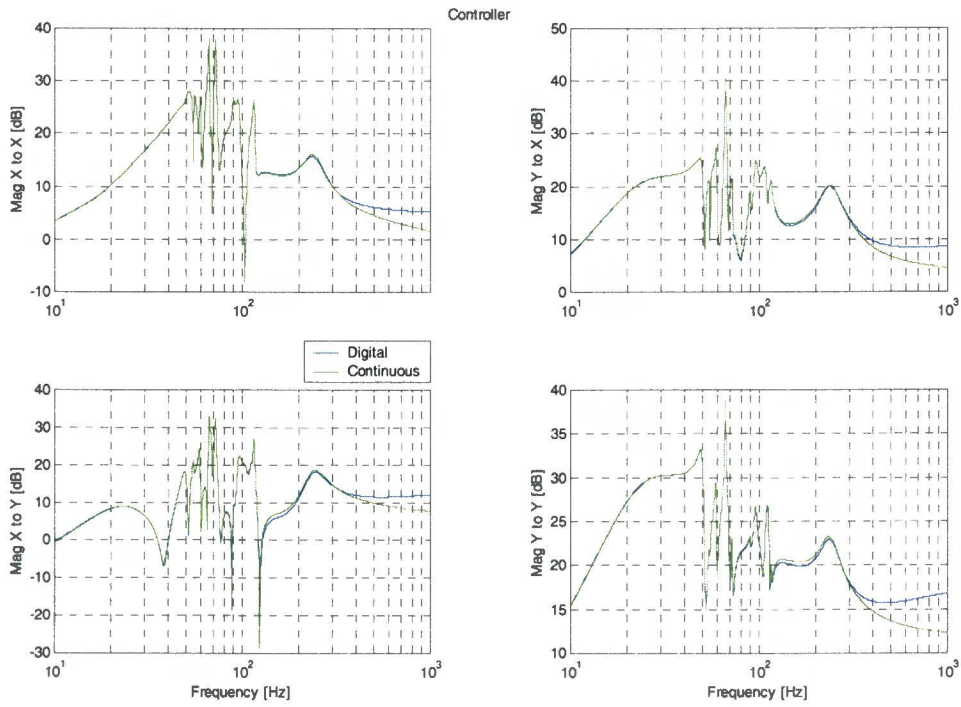


Figure 1.1: Controller digitized with ZOH

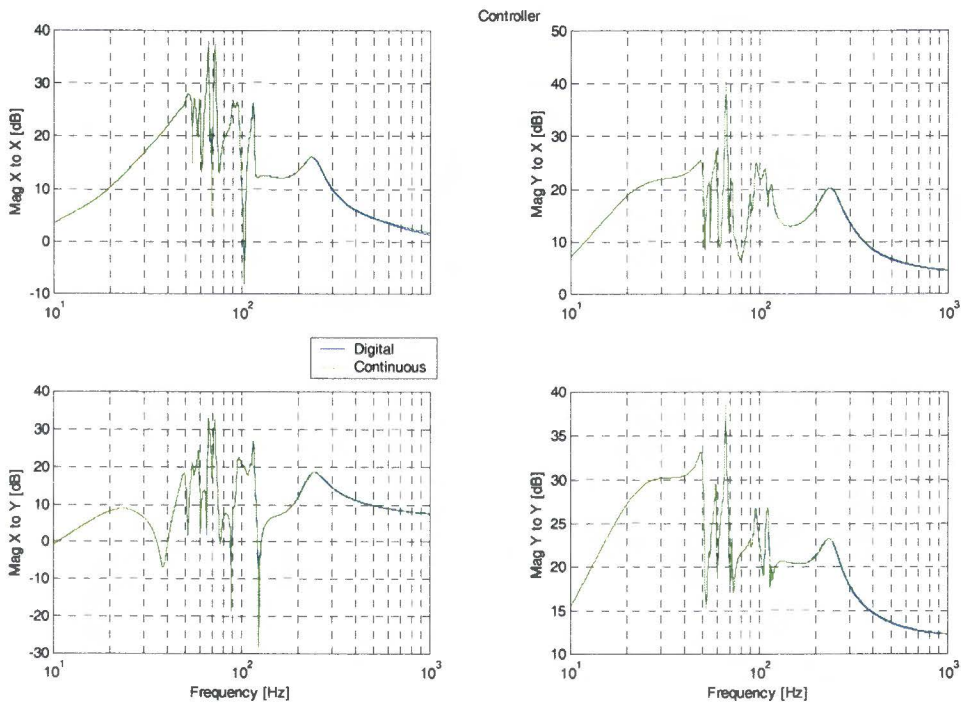


Figure 1.2: Controller digitized with Tustin's method

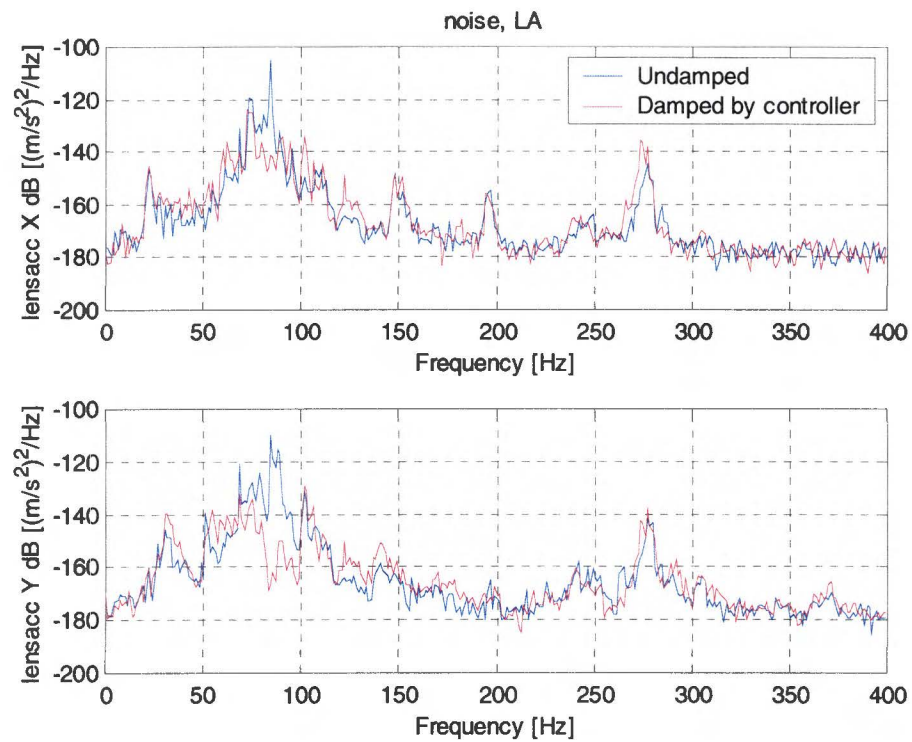


Figure I.3: Lenstop acceleration during noise

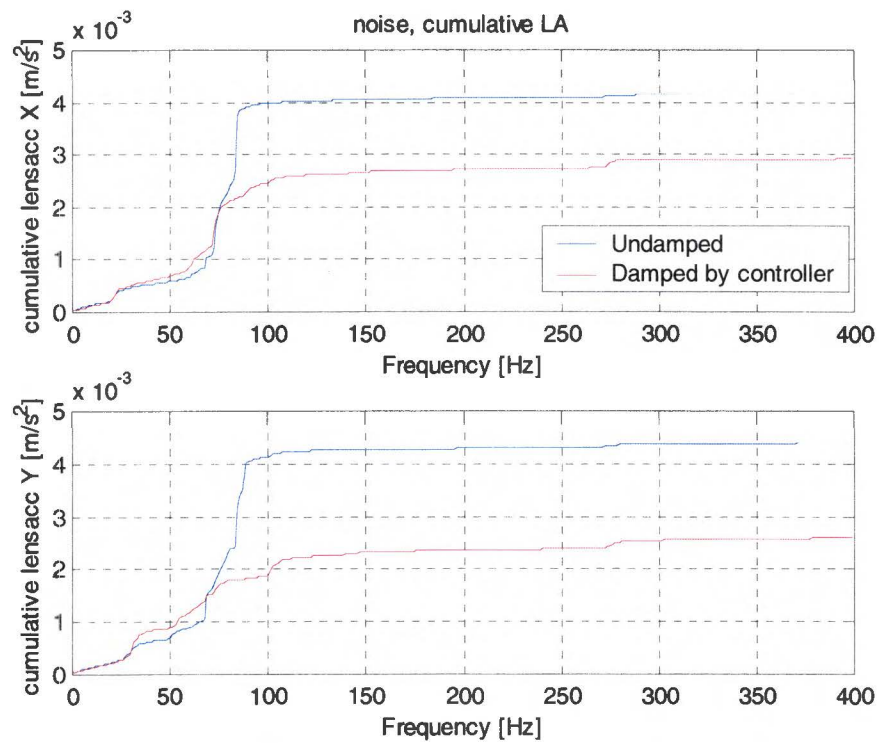


Figure I.4: Cumulative lenstop acceleration during noise

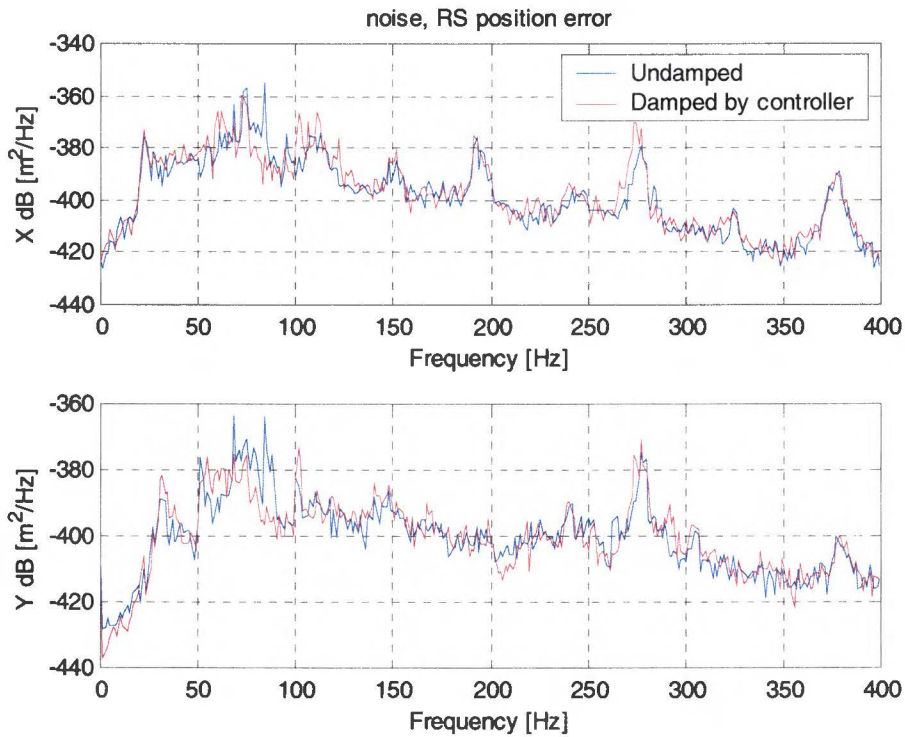


Figure 1.5: RS position error during noise

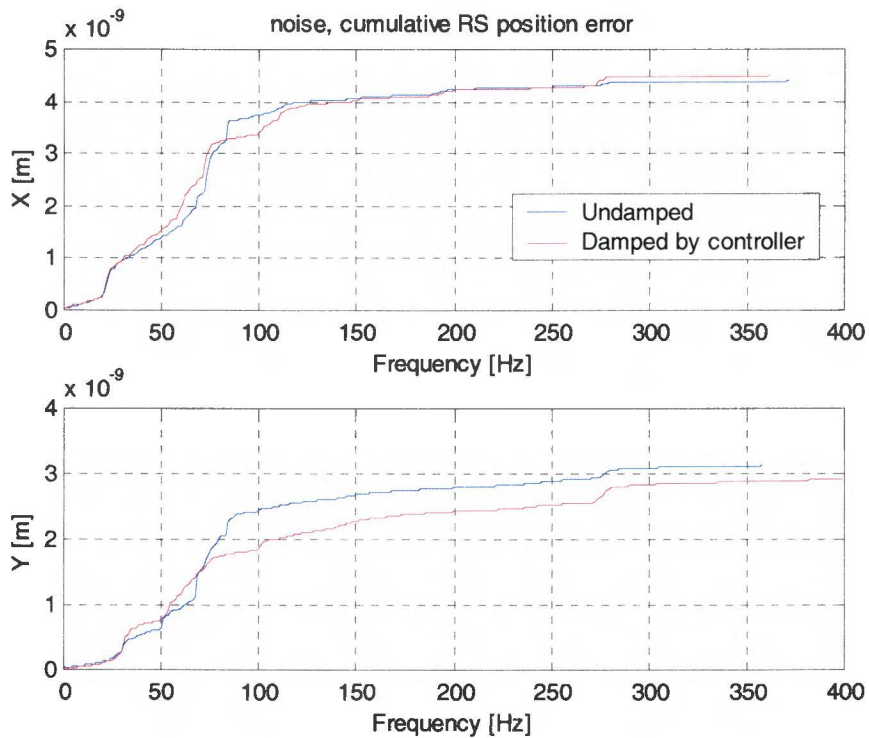


Figure 1.6: Cumulative RS position error during noise

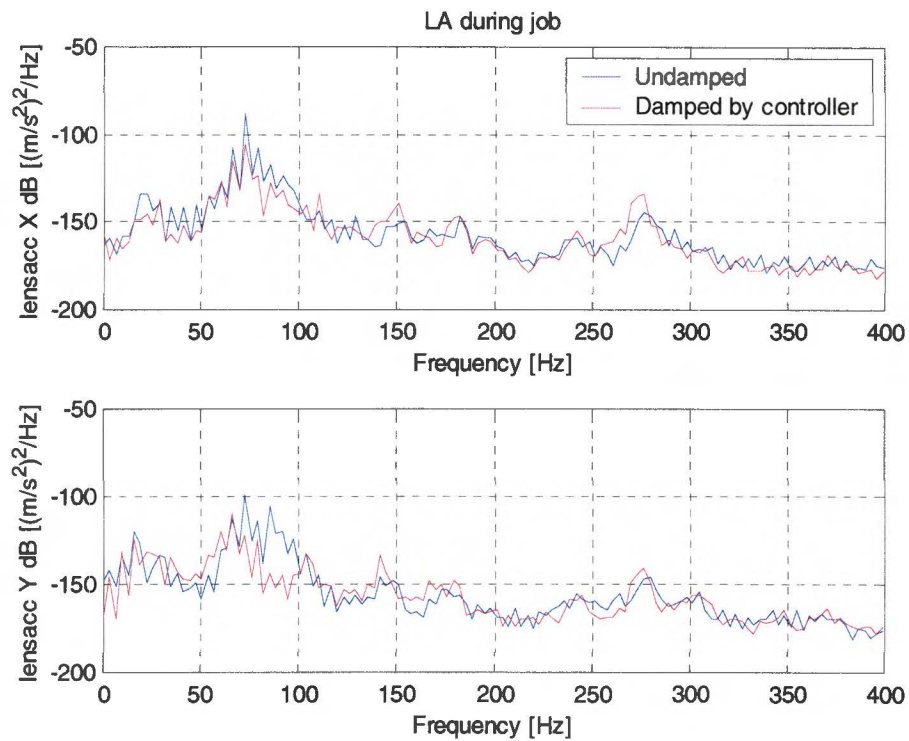


Figure 1.7: Lenstop acceleration during job

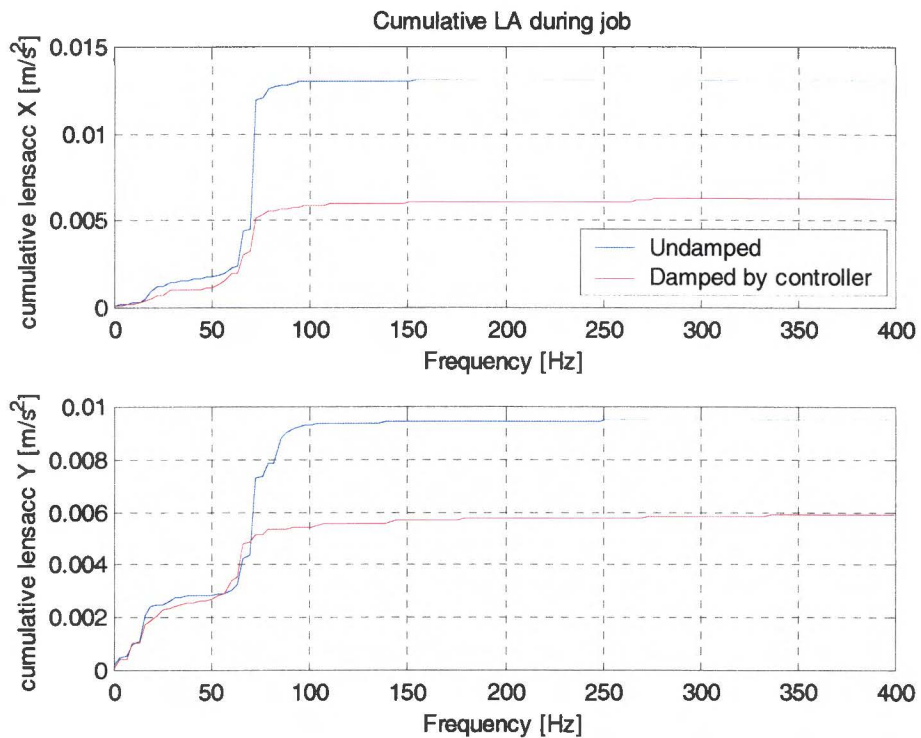


Figure 1.8: Cumulative lensstop acceleration during job

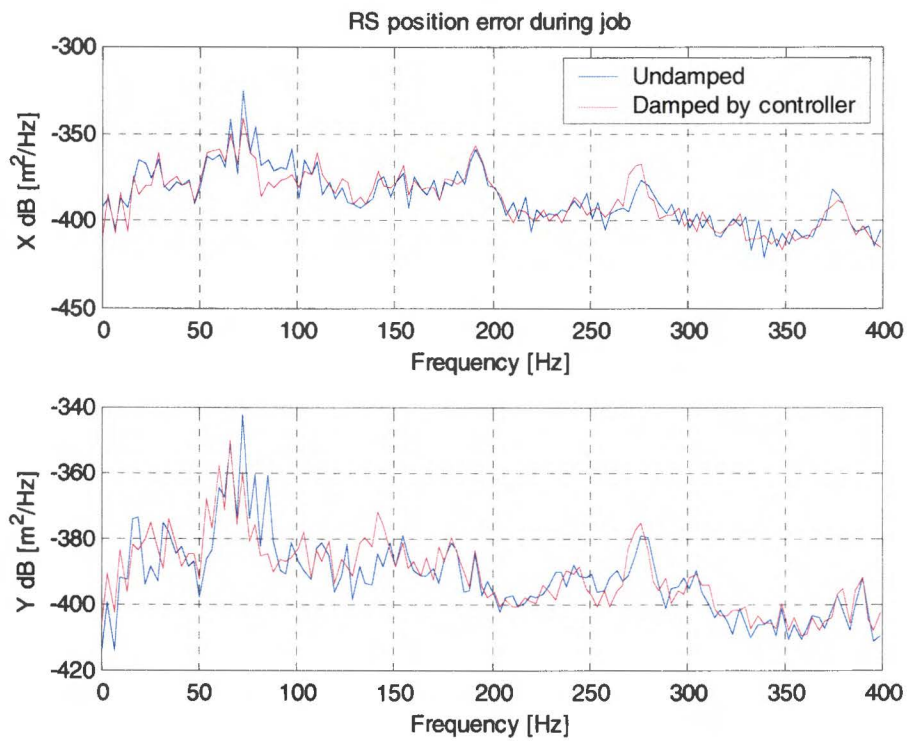


Figure 1.9: RS position error during job

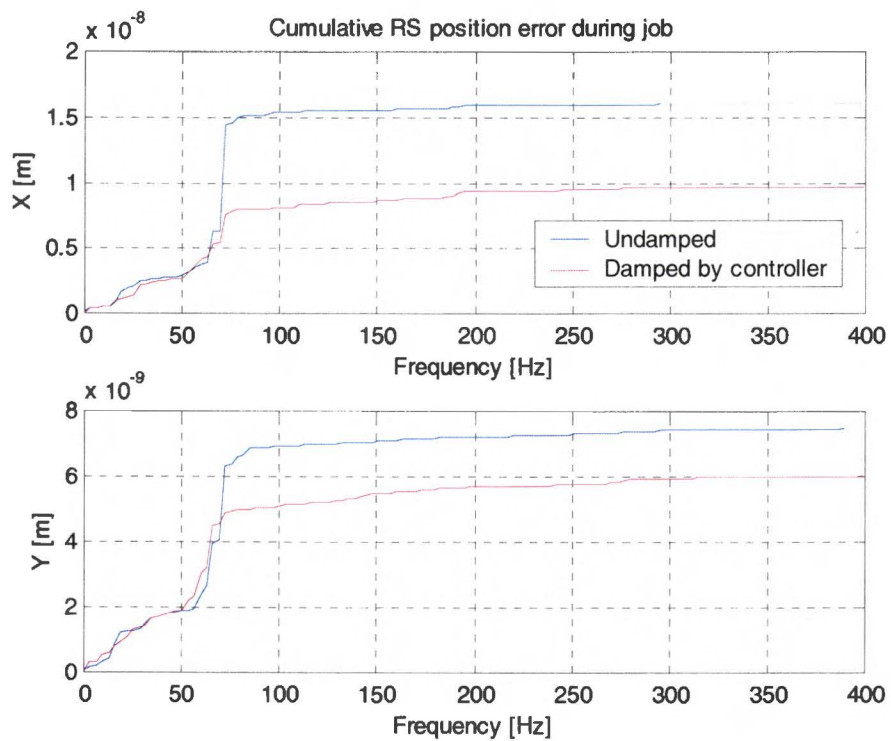


Figure 1.10: Cumulative RS position error during job